

Scalar tetraquark candidates on the lattice

Dissertation
zur Erlangung des Doktorgrades
der Naturwissenschaften

vorgelegt beim Fachbereich Physik
der Johann Wolfgang Goethe-Universität
in Frankfurt am Main

von
Joshua Berlin
aus Frankfurt am Main

Frankfurt am Main 2017
D30

vom Fachbereich Physik der
Johann Wolfgang Goethe-Universität als Dissertation angenommen.

Dekan: Prof. Dr. O. Philipsen

Gutachter: Prof. Dr. M. Wagner
Prof. Dr. C. Alexandrou

Datum der Disputation:

CONTENTS

Deutsche Zusammenfassung	vii
<hr/>	
1 Introduction	1
2 QCD on the lattice	5
2.1 The classical theory	5
2.2 Lattice gauge action	7
2.3 Wilson fermions	8
2.4 Path integrals from the lattice	12
2.4.1 Fermion contraction	12
2.4.2 Gauge field Configurations	13
2.5 Correlation functions	16
2.6 Towards the continuum	17
2.6.1 Infinite volume limit	17
2.6.2 Continuum limit	17
2.6.3 Chiral limit	18
2.7 Setting the scale	19
3 Meson spectroscopy	21
3.1 Multi-particle correlators	21
3.2 The variational method	23
3.3 Interpolating operators	26
3.3.1 Four-quark interpolators	27
3.4 Techniques for propagator computation	32
3.4.1 Point-to-all propagators	33
3.4.2 Stochastic timeslice-to-all propagators	34
3.4.3 The one-end trick	36
3.4.4 Sequential propagators	37
3.5 Smearing Techniques	39
3.5.1 Gauge link smearing	39
3.5.2 Smeared quark sources and sinks	40

4	Technical aspects	41
4.1	Simulation details	41
4.1.1	Fixing a charm quark mass	42
4.2	Computation of the correlation matrix	43
4.2.1	Two-quark – two-quark	45
4.2.2	Two-quark – four-quark	46
4.2.3	Two-quark – two-meson	47
4.2.4	Four-quark – four-quark	49
4.2.5	Four-quark – two-meson	49
4.2.6	Two-meson – two-meson	53
4.2.7	Efficiency for different flavor setups	56
4.3	Relevance of $2\times$ connected contributions	58
5	Investigation of scalar tetraquark candidates	65
5.1	The light candidate: $a_0(980)$	65
5.1.1	Omitting quark loop contributions	68
5.1.2	Including quark loop contributions	73
5.2	The heavy candidate: $D_{s0}^*(2317)$	84
5.2.1	Omitting quark loop contributions	86
5.2.2	Including quark loop contributions	89
	Conclusions & Research perspectives	97
	<hr/>	
	Appendix A Notations and conventions	101
A.1	Gamma matrices	101
A.2	Parity transformation	102
A.3	Charge conjugation	102
	Appendix B Computation of matrix elements	103
B.1	Spin diagrams	103
B.2	Application of techniques	105
B.3	Application of sequential propagation	106
B.4	Propagator content of methods	107
	<hr/>	
	Bibliography	113
	Acknowledgments	121
	Curriculum Vitae	123

To my mother

DEUTSCHE ZUSAMMENFASSUNG

Auf Längenskalen von einem Fermi ($1 \text{ fm} = 10^{-15} \text{ m}$), was ungefähr dem Radius eines Protons entspricht, ist die *starke Wechselwirkung* die vorherrschende Kraft des Universums. Gemeinsam mit der *elektromagnetischen* und *schwachen Wechselwirkung* ist sie Teil des Standardmodells der Teilchenphysik, welches unter Ausschluss der Gravitation sämtliche bekannte Teilchen und deren Interaktionen beschreibt. Der starken Wechselwirkung kommt dabei die Rolle des Zusammenschlusses fundamentaler Materie zuteil.

Die Geschichte der Theorie hinter dieser starken Kraft reicht mehr als 60 Jahre zurück. Zu einer Zeit, in der immer neue Teilchen in Experimenten entdeckt wurden, gelang es M. Gell-Mann und J. Ne'eman unabhängig voneinander diese schematisch miteinander in Verbindung zu setzen. Als Teil einer $SU(3)$ -Flavor-Symmetrie formten Baryonen so Oktetts und Dekupletts, Mesonen Oktetts und Singlets. Das Ω^- Baryon, welches von Gell-Mann vorhergesagt werden konnte um das Baryon Dekuplett zu vervollständigen, wurde 1964 am Brookhaven National Laboratory gemessen. 1969 wurde Gell-Mann dafür der Nobelpreis der Physik verliehen, *for his contributions and discoveries concerning the classification of elementary particles and their interactions*.

Die Bausteine der $SU(3)$ -Flavor-Darstellung, sogenannte Quarks, blieben jedoch in Experimenten unbeobachtet. Sie sollten in drei Generationen existieren (up, down, strange) und fraktale Ladungen ($2/3, -1/3, -1/3$) aufweisen. So würden Baryonen aus je drei Quarks und Mesonen aus einem Quark-Antiquark-Paar bestehen. Doch unter anderem bereitete das Ω^- erneut Probleme. Mit Spin $3/2$ und als gebundener Zustand von drei strange Quarks (sss) sollte dieses eine symmetrische Wellenfunktion aufweisen, was jedoch dem für Fermionen geltenden Pauli-Prinzip widersprach. Lösung bat ein zusätzlicher Freiheitsgrad für Quarks, die sogenannte Farbladung. Diese ermöglicht die Unterscheidung der Quarks in mindestens einer Quantenzahl, wodurch ihre Wellenfunktionen wieder antisymmetrisch sind. Innerhalb dieser zusätzlichen exakten $SU(3)$ -Farbsymmetrie müssen Hadronen dann als farbneutrale Zustände vorliegen. Baryonen sind so antisymmetrisch in Farbindizes ($\epsilon_{abc}q_aq_bq_c$) und Mesonen symmetrisch ($q_a\bar{q}_a$) realisiert. Dieser zusätzliche Freiheitsgrad ist namensgebend für die Theorie der starken Wechselwirkung, die sogenannte *Quantenchromodynamik* (QCD).

Bei der Formulierung der Quantenchromodynamik als nicht-abelsche Eichtheorie mit Symmetriegruppe $SU(3)_C$ erhält das Eichfeld durch die acht Generatoren der Gruppe acht 4-Vektorpotentiale, die acht Gluonenfeldern entsprechen. Die Gluonen sind die Träger der starken Kraft und erlauben es den Quarks durch Emission oder Absorption ihre Farbe zu ändern. Sie treten jedoch nicht nur in Verbindung mit den Quarks, sondern auch in antisymmetrischer Form im Feldstärketensor auf. Dadurch kommt es zu dreifach und vierfach Gluon-Gluon-Wechselwirkungen im Eichfeld-Term der La-

grangedichte. Diese Interaktionen führen zu charakteristischen Eigenschaften der QCD. Zum einen führen sie auf kleinen Abständen, bei der räumlichen Separation eines Quark-Antiquark-Paares dazu, dass sich die Gluonenfelder nicht ausbreiten, wie man es aus der Elektrodynamik erwarten würde, sondern sich gegenseitig anziehen. Das Quark-Antiquark-Paar ist also durch einen konstanten String von gluonischen Feldlinien, und dadurch mit einer konstanten Kraft, miteinander verbunden. Man sagt Quarks unterliegen dem sogenannten *Confinement* (‘‘Gefangenschaft’’). Das Trennen eines solchen Paares führt bei genügend Energiezufuhr nur zur Erzeugung eines neuen Quark-Antiquark Paares und es wird angenommen, dass, obwohl der analytische Beweis fehlt, diese Eigenschaft Grund dafür ist, warum einzelne Quarks unbeobachtet bleiben. Zum anderen führen sie zur Abnahme der Kopplungskonstante für zunehmende Energien oder kleinere Abstände. Quarks und Gluonen verhalten sich in diesen Regionen wie in einer freien Theorie. Diese Eigenschaft bezeichnet man als *asymptotische Freiheit*. Dadurch lässt sich die QCD für kleine Energien nicht als Entwicklung in ihrer Kopplung untersuchen. Vorgänge in diesen Bereichen, wie die Formation des Hadronenspektrums, bleiben für die Störungstheorie unzugänglich. Anders als für den Fall der Quantenelektrodynamik ist die QCD streng nicht-perturbativ. Für die Entdeckung des Aspekts der asymptotischen Freiheit erhielten D. Politzer, F. Wilczek und D. Gross 2004 den Nobelpreis der Physik.

Eine der wenigen Methoden, die in der Lage sind die Quantenchromodynamik auch auf solch kleinen Energieskalen ohne Annahmen zu untersuchen, sind sogenannte Gittereichtheorien. Hier wird die Theorie der QCD diskretisiert und auf ein vierdimensionales, endliches, euklidisches Raumzeit-Gitter gelegt. Wichtig ist dabei erst einmal nur, dass die Theorie im Kontinuum $a \rightarrow 0$ wiederhergestellt wird. Die exakte Form der Diskretisierung ist damit nicht eindeutig und erlaubt gewisse Freiheiten. Allen gemein sind die Vorteile der *Gitterregularisierung*: Durch den endlichen Gitterabstand a erhält die Theorie einen ultraviolettten Cutoff, wodurch keine Divergenzen auftreten. Die endliche euklidische Raumzeit ermöglicht darüber hinaus die exakte Berechnung der in der Feldtheorie auftretenden Pfadintegrale. Das Gitter erhält darüber hinaus die lokale $SU(N_c)$ -Eichinvarianz und viele der Symmetrien, die verletzt sind, werden im Kontinuum wiederhergestellt und stellen damit also kein größeres Problem dar. Dies ist nicht der Fall für die *chirale Symmetrie*. Diese wird in der wahrscheinlich prominentesten Diskretisierung der Fermionenwirkung, der sogenannten Wilson-Fermionenwirkung, explizit gebrochen und im Kontinuum nicht wiederhergestellt. Ursache dieses Symmetriebruchs auf dem Gitter ist ein zusätzlich eingeführter Term, der wiederum ein anderes Gitterartefakt kontrollieren soll. Diese beiden Umstände werden im Nielsen-Ninomiya-Theorem miteinander verknüpft. Danach stellen sie zwei von insgesamt vier Konsequenzen der Fermion-diskretisierung dar, von denen stets eine unvermeidlich ist. Heute existieren auch Diskretisierungen, die versuchen diesen Effekt zu mildern oder tatsächlich chirale Symmetrie im Kontinuum wiederherzustellen.

Die unverkennbaren Stärken der Gitter-QCD erlauben die Untersuchung einer Vielzahl interessanter Fragestellungen. So können zum Beispiel unter Abwesenheit von Fermionen, mit reiner $SU(3)$ Eichtheorie, die Wechselwirkungen zwischen Gluonen oder Quark-Antiquark-Paaren untersucht werden. Dieser Bereich ist dem Experiment unzugänglich und trägt zum Verstehen von Confinement oder der Formation von Hadronen bei. Mit Hilfe experimenteller Daten gelingt es ferner gesamte Spektren beobachteter

Hadronen auf dem Gitter zu berechnen. Das unterstützt nicht nur die Annahme der QCD als korrekte Theorie der Teilchenphysik überall dort, wo Gitter und Natur übereinstimmen, sondern mag vielleicht auch eine Physik jenseits des Standardmodells implizieren, wo dies nicht der Fall ist. Auch die QCD-Phasenstruktur lässt sich für hohe Temperaturen oder nicht verschwindende Dichten untersuchen. Das Auflösen des Columbia Plots, der chirale Phasenübergänge für verschiedene Flavor-Setups zusammenfasst, sei da nur ein Beispiel für eine moderne Problemstellung.

Neben einer explizit gebrochenen chiralen Symmetrie, die auf dem Gitter in der Regel in Kauf genommen wird, existieren noch weitere Umstände, die Gittersimulationen verkomplizieren. Im Vordergrund steht der immense Aufwand, der benötigt wird, um letztendlich Aussagen über das Kontinuum tätigen zu können. Einer der größten Vorteile des Gitters - die Möglichkeit Pfadintegrale exakt zu berechnen - verlangt nach einer euklidischen Raumzeit. Denn trotz der endlichen Ausdehnung des Hyperwürfels ist der Parameterraum der Pfadintegrale zu groß für eine praktische Simulation. Während die fermionischen Freiheitsgrade ausintegriert werden können, ist das System dennoch durch die Eichfreiheitsgrade bestimmt. Es werden sogenannte *Monte-Carlo-Methoden* eingesetzt, um den Raum der möglichen (Eich-)Feldkonfigurationen auf eine für das Pfadintegral relevante Teilmenge zu reduzieren. Das ist nur in einer euklidischen Raumzeit möglich und, zum Beispiel, im Falle eines vorhandenen chemischen Potentials selbst dann nicht. Zusätzlich wird diese Aufgabe gegebenenfalls durch Fermionendeterminanten erschwert. Diese tragen nach dem Ausintegrieren der Fermionenfriheitsgrade zum Eichintegral bei und erfordern selbst wieder großen numerischen Aufwand. Mit kleiner werdenden Quarkmassen werden die Fermionenmatrizen beinahe singulär, so dass die iterativen Prozesse zu deren Bestimmung wesentlich langsamer konvergieren und somit viel Zeit in Anspruch nehmen. Das Berechnen der Eichfelder auf diese Weise erfordert den Einsatz moderner Supercomputer.

Unter anderem aus diesen Gründen arbeiten auch heute noch Gittersimulationen mit unphysikalischen Quarkmassen. In der Hadronenspektroskopie werden typischerweise Simulationen für Pionmassen von 200 - 300 MeV angeführt, welche wesentlich günstiger sind, als am physikalischen Punkt. Der naive Kontinuumsliches $a \rightarrow 0$ wird dadurch jedoch um die Notwendigkeit eines zusätzlichen chiralen Limes erweitert. Um die Extrapolation allein von Gitterrechnungen ausgehend zu motivieren, muss der physikalische Punkt dann immer noch ansatzweise erreicht werden. Ferner muss sichergestellt werden, dass sich physikalische Begebenheit und Beobachtungen währenddessen nicht ändern.

Darüber hinaus stellte die euklidische Zeit des Gitters für Streuprozesse lange ein Problem dar. Die darin auftretenden Resonanzen sind im Gegensatz zu stabilen Zuständen (im Rahmen der starken Wechselwirkung) keine Eigenzustände des Hamiltonians und können nicht direkt mit euklidische Korrelatoren untersucht werden. Ihre Eigenschaften sind durch Streu- und Übergangsamplituden definiert, die wiederum nur in Minkowski-Zeit vorliegen. Eine analytische Fortsetzung der euklidischen Korrelationsfunktionen zum Minkowski-Raum ist für kleine Energien zwar über chirale Störungstheorie möglich, wegen der Auflösung der Korrelatoren selbst jedoch häufig nicht in vernünftigem Maße. Großes Aufsehen innerhalb der Gittergemeinschaft gewann 1991 die von M. Lüscher gefundene Methode um über Gitterrechnungen *indirekt* Streuamplituden berechnen zu können. Darin wird das diskrete Energiespektrum euklidischer Zwei-Teilchen-Zustände im endlichen Volumen mit der elastischen Streuamplitude im

unendlichen (Minkowski-)Volumen in Verbindung gebracht. Die Lüscher-Methode wurde seither um inelastische Streuungen erweitert und ihre Anwendung stellt einen modernen Zweig der Hadronenspektroskopie dar. Der Umfang dieser Methode auf Basis von Gitterrechnungen ist jedoch um ein Vielfaches aufwändiger, verglichen mit der konventionellen Spektroskopie gebundener Zustände. Es bedarf einer hervorragenden Auflösung verschiedener Zwei-Teilchen-Zustände und Simulationen auf mehreren Volumina sind essentiell. Die Zwei-Teilchen-Zustände hängen dabei, unter anderem, von der Pionmasse ab, wodurch sich Ergebnisse für leichtere Pionen eventuell komplett verändern. Die Berechnung des einfachsten Streuprozess $\pi\pi \rightarrow \rho \rightarrow \pi\pi$ liegt so erst seit ~ 2004 im Rahmen der numerischen Möglichkeiten.

An großem Interesse, sowohl theoretisch als auch experimentell, erfreut sich aktuell die Erforschung *exotischer* Hadronen. So werden jene Hadronen bezeichnet, die vom konventionellen Quarkmodell ($q\bar{q}$ bzw. qqq) abweichen oder Quantenzahlen besitzen, die nicht mit dem Quarkmodell vereinbar sind. Im Fall von Mesonen kann es sich so alternativ um einen Aufbau rein aus Gluonen (gg), einem zusätzlichen Gluon ($qg\bar{q}$) oder zwei Quark-Antiquark-Paaren halten ($qq\bar{q}\bar{q}$). Kandidaten für solch einen exotischen Aufbau sind meist Zustände nahe der jeweiligen Mehr-Teilchen-Schwellen mit den entsprechenden Zerfallskanälen oder solche, deren Beobachtungen stark der theoretischen Erwartung widersprechen. Eines der besten Beispiele ist das Tetraquark $Z_C(3900)$, welches 2013 unabhängig von BES III und dem Belle-Experiment bestätigt wurde. Dieser geladene Zustand zerfällt in ein Pion (π^\pm) und ein J/ψ -Meson, was auf ein vorhandenes charm-anticharm-Paar schließen lässt. Die Ladung des Zustands ist nur durch die zusätzliche Anwesenheit eines leichten Quarkpaares möglich, wodurch der Inhalt des $Z_C(3900)$ mindestens vier Quarks umfassen muss. Ein aktuelles Beispiel für ein exotisches Baryon sind die 2015 von der LHCb-Kollaboration am CERN identifizierten Pentaquarks $P_C^+(4380)$ und $P_C^+(4450)$, die als kurzlebige Zustände im Zerfallskanal $\Lambda_b^0 \rightarrow J/\psi K^- p$ auftreten.

Im Fokus dieser Arbeit liegen jedoch andere Tetraquark-Kandidaten. Zum einen wird das $a_0(980)$ untersucht. Es ist Teil des auf theoretischer Ebene schlecht verstandenen Nonetts leichter skalarer Mesonen mit Quantenzahlen $I(J^P) = 1(0^+)$. Diese werden im nicht-relativistischen Quarkmodell, neben 1^{+-} , 1^{++} und 2^{++} , als P -Wellen identifiziert und sollten gegenüber den pseudoskalaren Mesonen und Vektormesonen ohne Bahndrehimpuls, 0^{-+} und 1^{--} , den S -Wellen, wesentlich höhere Massen aufweisen als sie experimentell gefunden wurden. Ferner ist die Massenhierarchie der Zustände innerhalb des Nonetts invertiert zu der, die man von der konventionellem Quark-Antiquark Interpretation erwarten würde. Es liegt eine Massenentartung zwischen $f_0(980)$ und $a_0(980)$ vor, wobei im $q\bar{q}$ -Bild das isosinglet σ und das isotriplet a_0 entartet sein sollten. Die Interpretation der Mesonen dieses Nonetts als Tetraquarks löst das beobachtete Bild beinahe natürlich auf. Darin würde das σ aus einem zusätzlichen leichten Quark Paar bestehen, wohingegen das f_0 und a_0 um ein zusätzliches strange Quark Paar erweitert würden. Die Massenhierarchie wäre invertiert, wie beobachtet, und die Massenentartung zwischen f_0 und a_0 wäre durch den gemeinsamen strange-Inhalt ebenso erklärt.

Sehr verwandt zu diesem Problem verhält sich die Situation um das $D_{s0}^*(2317)$ herum. In der konventionellen Quark-Antiquark-Intepretation ist dieses Meson ein $c\bar{s}$ -Zustand, wird jedoch unterhalb der DK -Schwelle beobachtet, genauso wie sein Partner $D_{s1}(2460)$ unterhalb der D^*K -Schwelle beobachtet wird. Die Nähe der beiden Zustände zueinander, sowie ein Verhalten ähnlich des $a_0(980)$ knapp unter der $K\bar{K}$ -Schwelle, sind

mitunter Motivation für eine Tetraquark-Interpretation der beiden Zustände. Ferner werden beide D_{sJ} als leichter beobachtet als sie von Modellen oder Gitterberechnungen, die dem konventionellen Ansatz folgen, vorhergesagt werden.

Diese Dissertation ist wie folgt aufgebaut. Kapitel 1 widmet sich erneut der Motivation der vorliegenden Arbeit mit Fokus auf der Gitterdiskretisierung sowie der Untersuchung möglicher Tetraquark-Kandidaten in deren Rahmen. Im zweiten Kapitel wird ein vorangehendes Wissen der Quantenfeldtheorie angenommen, sodass wir uns umgehend mit den theoretischen Grundlagen der Gitterdiskretisierung beschäftigen können. In gewohnter Weise besprechen wir separat den gluonischen und fermionischen Anteil der QCD Wirkung. In beiden Fällen gelangen wir von einer naiven Diskretisierung zu Wilsons ursprünglicher Formulierung und besprechen anschließend Alternativen und Wirkungen mit verbessertem Kontinuumslikes. Daraufhin erläutern wir schematisch stochastische Integrationsmethoden die zur Lösung des Gitter-QCD-Pfadintegral verwendet werden, bei denen man sich effektiv auf eine relevante Teilmenge von Eichfeldkonfigurationen beschränkt. Die Grundlagen der Gitter-QCD schließen wir mit dem Kontinuumslikes ab, auch wenn dieser im Rahmen dieser Arbeit keine Anwendung findet.

In Kapitel 3 erweitern wir dann die theoretischen Grundlagen der Mesonenspektroskopie auf die Untersuchung eventueller Vier-Quark-Zustände. Dabei bedienen wir uns dem Beispiel des $a_0(980)$ und schildern zusätzliche Schwierigkeiten, die bei einer solchen Untersuchung auftreten. Anders als bei simplen Grundzuständen sind wir bei diesen Kandidaten dazu gezwungen, idealerweise das gesamte Zwei-Teilchen Spektrum der entsprechenden Quantenzahlen aufzulösen. Dazu verwenden wir eine Basis von Erzeugungsoperatoren, die sowohl die Zwei-Teilchen-Zustände auflösen soll, als auch den entsprechenden Kandidaten auf einen Zwei- oder Vier-Quark-Inhalt hin modellieren soll. Generell unterscheidet man dabei den Aufbau der Tetraquarks. Zwei eng gebundene Quark-Antiquark-Paare, bei denen die Restkräfte zu einem gebundenen Vier-Quarkzustand führen, bezeichnet man als mesonisches Molekül. Sind die beiden Quarks zu einem Diquark und die beiden Antiquarks zu einem Antidiquark zusammengebunden, so stellt der gebundene Diquark-Antidiquark-Zustand erneut ein mögliches Farbsinglett dar. Häufig wird mit der Verwendung des Begriffs ‘Tetraquark’ auf eine solche Konfiguration referiert. Wir nutzen diesen jedoch umfangreicher als generelle Bezeichnung eines Vier-Quarkzustandes. Darüber hinaus führen wir in diesem Kapitel detailliert die verwendeten Techniken zur Abschätzung von Quarkpropagatoren auf dem Gitter ein. Jede besprochene Technik ist ein relevantes Element dieser Arbeit und zur Untersuchung des Gesamtbildes nicht zu vernachlässigen.

Kapitel 4 beschäftigt sich mit technischen Aspekten dieser Arbeit. So bestimmen wir zum einen eine charm-Quarkmasse innerhalb unseres $N_f = 2 + 1$ -Ensembles, in dem wir pseudoskalare Mesonen so anpassen, dass sie mit den Energien der erwarteten open-charm-Mesonen übereinstimmen. Dies ermöglicht uns dann im späteren Verlauf die qualitative Untersuchung eines Kandidaten für das $D_{s0}^*(2317)$. Zusätzlich untersuchen wir eine Vielzahl verschiedener Möglichkeiten, um die Elemente der für uns relevanten Matrix von Korrelationsfunktionen zu berechnen. Diese Methoden entsprechen unterschiedlichen Kombinationen der in Kapitel 3 eingeführten Propagator-Techniken und bilden das Fundament jeder anschließenden Analyse. Es ist daher von besonderer Wichtigkeit die effizienteste Strategie zur Berechnung jedes einzelnen Elements zu bes-

timmen, da bereits einzelne problematische Fälle Auswirkungen auf die gesamte Matrix mit sich bringen. Die Klasse jener problematischer Kandidaten identifizieren wir im Verlauf dieser Arbeit genauer und behandeln sie in diesem Kapitel noch einmal gesondert.

Das fünfte Kapitel ist das Letzte dieser Arbeit und präsentiert die Resultate verschiedener Analysen zu den beiden untersuchten Tetraquark-Kandidaten $a_0(980)$ und $D_{s_0}^*(2317)$. Wir betrachten dabei verschiedene Unterprobleme der jeweiligen Kandidaten und legen so eine umfangreiche Analyse der berechneten Daten aus. Abschließend fassen wir Erkenntnisse und Ergebnisse dieser Arbeit zusammen und geben einen Ausblick auf zukünftige Forschungsperspektiven.

1

INTRODUCTION

Quantum Chromodynamics (QCD) is the established theory of strong interactions. It is based on quarks and gluons as fundamental constituents of hadronic matter, such as mesons and baryons. Its formulation as a non-abelian gauge theory makes the mediators of the strong force, the gluons, go through self-interactions. Through these interactions the coupling of QCD decreases for increasing energies. The feature of *asymptotic freedom* hence dominates QCD at short distances or large energies, where quarks and gluons interact only weakly. In this region a perturbative expansion in the QCD coupling becomes possible. At energies below the QCD scale $\Lambda_{\text{MS}} \approx 220$ MeV the coupling becomes too large so that perturbative studies can not be applied. To obtain insights on processes below this scale, e.g. the hadronic spectra, a non-perturbative approach has to be considered.

Lattice QCD, originally proposed by K. Wilson [1], provides an ultraviolet and infrared cutoff for the theory by defining a shortest distance a in an enclosed volume $L^3 \times T$. The ideal hierarchy of scales being

$$\Lambda_{\text{IR}} = L^{-1} \ll m_\pi, \dots, m_D, m_B \ll a^{-1} = \Lambda_{\text{UV}}. \quad (1.1)$$

The regularization is realized by defining the theory on a finite, four-dimensional Euclidean spacetime grid. On this grid the path integral formulation of quantum field theory is utilized, where path integrals become finite objects. In analogy to statistical mechanics, stochastic integration methods, such as Markov chain Monte Carlo methods, are used to compute these integrals. The inclusion of dynamical quarks is a delicate task during this process, so that even at modern times unphysically heavy light quarks are used for simulations. The continuous theory is then recovered by sending the lattice spacing $a \rightarrow 0$ while keeping the box size $L^3 \times T$ finite. As a consequence of the heavy quarks employed throughout computations, also the limit $m_q \rightarrow m_q^{\text{phys}}$ has to be studied.

Hadron spectroscopy is a modern branch of lattice QCD studies. Hadrons are bound states of QCD, composed of quarks and gluons. They are colorless objects and can be divided in two sub-categories, baryons and mesons. In the conventional quark model the former states are composed of three valence quarks or antiquarks, each with different color, while the latter are composed of a valence quark antiquark pair¹. Studying hadronic spectra from first principles by lattice QCD is a vital tool for modern physics. The computation of experimentally well established particles is an important benchmark

¹Emphasize on valence quarks is given to implicitly include gluons as well.

test to the theory of QCD. Reproducing experimentally measured spectra by lattice calculations is one of the strongest indications that QCD is the correct theory to describe nature at this scale we have. Even though pions appear as unphysically heavy particles, a lot of computational power can be invested to perform a chiral extrapolation or to provide a qualitative analysis of the respective spectra [2, 3, 4, 5, 6, 7]. In these studies lattice spectroscopy also occasionally advances to predict new states that have not been observed in experiments or finds significant deviations from those, possibly indicating physics beyond the conventional quark model.

In addition to the just mentioned hadronic content ($\epsilon_{abc}q_aq_bq_c$ and $q_a\bar{q}_a$) there are also other configurations that may apply to nature [8, 9]. For instance, there are in principle no limitations to the number of quarks inside a hadron, as long as a color neutral state is preserved. Such *exotics* experienced a lot of attention in recent years fueled by experimental evidence. A prominent example is the discovery of the $Z_c(3900)$, which was simultaneously measured by Belle and BESIII [10, 11] in $e^+e^- \rightarrow \pi^+\pi^-J/\psi$. A significant peak in the $\pi^\pm J/\psi$ mass spectrum, that couples to charmonium and has electric charge, was seen. This suggests a state containing more quarks than just a charm and anticharm, and is widely believed to be a tetraquark state. The first observation of a pentaquark was reported by the LHCb collaboration at CERN [12]. In $\Lambda_b^0 \rightarrow J/\psi K^- p$ the decay of the Λ_b^0 was measured to sometimes go through intermediate states ($P_c^+(4380)$ and $P_c^+(4450)$) instead of decaying directly into mesons and baryons.

Hadron spectroscopy in the framework of lattice QCD can provide important insights to understand such exotic structures. By defining well-suited creation operators the eigenstates of the QCD Hamiltonian can be studied by Euclidean correlation functions. They contain contributions from *all* hadronic excitations with quantum numbers of the operators involved. Extracting the leading and sub-leading exponentials does then allow to resolve the spectrum of interest. For example in the absence of quarks, in a pure $SU(3)$ gauge theory, the spectrum of glueballs below 4GeV has been extrapolated to the continuum [13]. For heavy quarks the Born-Oppenheimer approximation can be utilized to study the binding of two dynamical quarks, which suggests a $ud\bar{b}\bar{b}$ tetraquark in the scalar channel [14, 15]. However, such investigations with fully dynamical quarks unfold to be far more complicated.

While stable hadrons well below decay thresholds are in general safe to study on the lattice, excited and exotic hadrons as well as resonances pose a more sophisticated issue. It was indicated above, that signals for excited mesons are only found in sub-leading contributions to the Euclidean correlator. To obtain insights on these states one requires a large set of operators that yield high angular momenta, allow spin identification and still provide stable results. Resonances are not eigenstates of the Hamiltonian and need to be extracted indirectly. This turns out to be a tremendous task that requires large sets of operators and several lattice volumes to work as intended [16, 17]. Furthermore is this procedure highly sensible to thresholds, and analyses may change entirely with decreasing pion masses. Exotic mesons are to be found somewhere in between. Heavy tetraquark states (commonly referred to as XYZ -states) with experimental evidence, like the $Z_c(3900)$, are exciting candidates to study on the lattice. However, their masses exceed typical lattice scales and, more importantly, they lie above several two-particle thresholds. Thus, their investigation also relies on extensive operator sets, aimed to

resolve several compact two-particle states in addition to the identification of a possibly exotic state. Although experimentally confirmed, first studies on the $Z_c(3900)$ neglecting coupled-channels find no candidate [18, 19, 20], surely motivating more work into this direction.

The topic of this thesis is the investigation of scalar tetraquark candidates from lattice QCD. It is motivated by a previous study [21, 22, 23], originating in the twisted mass collaboration and continues the project [24, 25, 26, 27, 28]. The initial tetraquark candidate of choice is the $a_0(980)$, an isovector in the nonet of light scalars ($J^P = 0^+$). This channel is still poorly understood. It displays an inverted mass hierarchy to what is expected from the conventional quark model and the $a_0(980)$ and $f_0(980)$ feature a surprising mass degeneracy, cf. Figure 1.1. For this reason the $a_0(980)$ is a long assumed tetraquark candidate in the literature [29, 30, 31, 32].

We follow a methodological approach by studying the sensitivity of the scalar spectrum with fully dynamical quarks to a large basis of two-quark and four-quark creation operators. Ultimately, the candidate has to be identified in the direct vicinity of two two-particle states, which is understandably inevitable for a tetraquark candidate. To succeed in this difficult task two-meson creation operators are essential to employ in this channel. By localized four-quark operators we intend to probe the Hamiltonian on eigenstates with a closely bound four-quark structure.

The thesis is structured as follows. In Chapter 2 we introduce the basic principles of the lattice regularization of QCD. We follow a didactic approach by introducing a naïve discretization first and eventually ending up with Wilson's formulation. Improved and alternative actions are presented and the stochastic solution to path integrals is motivated. Although not performed in this work, the continuum limit is discussed at the end of this chapter. Chapter 3 focuses on the relevant theoretical aspects of this thesis. On the example of the $a_0(980)$ we elaborate the employed interpolator basis of choice and provide a detailed introduction to estimators for quark propagators. In Chapter 4 technical aspects of this study are presented. We summarize the numerical details of our lattice simulation and tune a charmed quark mass to prepare for a qualitative analysis of the $D_{s_0}^*(2317)$. Furthermore, we study various combinations of techniques to determine the most efficient strategy of computation for every element of our matrix. Chapter 5 is the last chapter of this thesis and presents the results of our studies on both tetraquark candidates by analyzing multiple sub-problems. The thesis is concluded by summarizing the obtained results and a brief outlook.

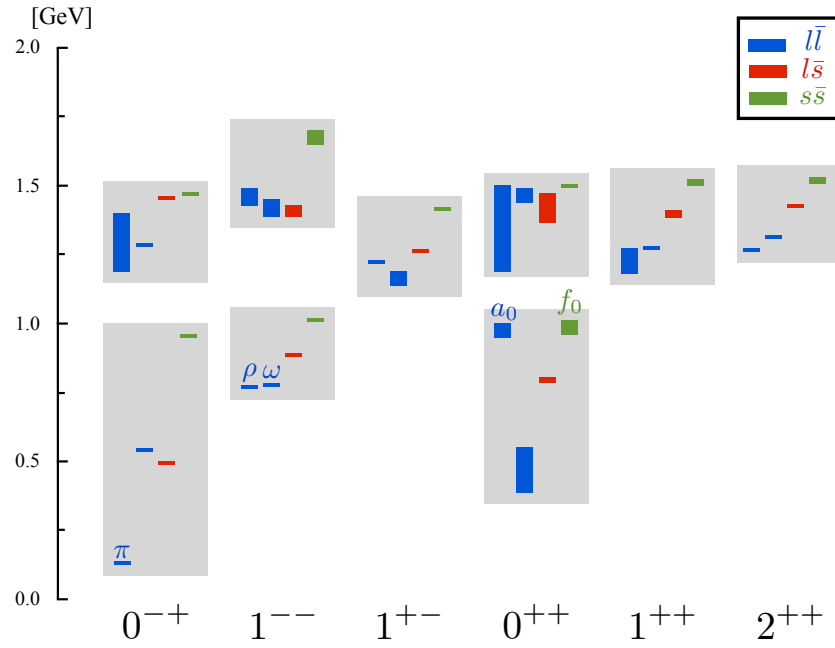


FIG. 1.1: Nonet of light mesons for several J^{PC} . Data taken from [29], extended boxes indicate uncertainties. Mass ordering of states are generally in agreement with expectations from the quark model. Obvious exceptions are the pions π as pseudo Goldstone bosons from the breakdown of the chiral-flavor symmetry, a mechanism we understand very well, and the a_0 in the 0^+ nonet.

2

QCD ON THE LATTICE

In this chapter we review the basic principles of a lattice formulation of QCD that are essential to study hadronic quantities. Section 2.1 presents the continuous version of a Euclidean quantum field theory briefly and motivates the transition to a discretized spacetime in order to regulate the theory. In Section 2.2 and 2.3 we describe the construction of a naïve lattice gauge and fermion action, respectively. Both allow for improvement in terms of discretization errors, but the latter can not be constructed to be local, doubler-free, chirally invariant and with the correct continuum limit. We proceed with the numerical computation of path integrals on the lattice in Section 2.4. After we have elaborated how we plan to compute hadronic quantities in this discrete world Section 2.6 presents the extrapolations necessary to relate the results to the physical, continuous world. In Section 2.7 we discuss how to set the scale for the *dimensionless* results of our simulations in order to relate them to any experimental result.

This introduction is based on the approach many standard text books [33, 34, 35, 36] follow and the reader is encouraged to consult those for a more detailed discussion. Alternatively, public lectures provide an excellent introduction into the topic [37, 38, 39], as well. In this section we closely follow the discussion in [35].

2.1 The classical theory

The continuous action of QCD in a 4-dimensional Euclidean space is conveniently separated into its fermionic and purely gluonic part

$$S_{\text{QCD}}[\psi, \bar{\psi}, A] = S_{\text{F}}[\psi, \bar{\psi}, A] + S_{\text{G}}[A],$$

with

$$S_{\text{F}}[\psi, \bar{\psi}, A] = \sum_{f=1}^{N_f} \int d^4x \bar{\psi}^{(f)}(x) \left(\gamma_{\mu} D_{\mu} + m^{(f)} \right) \psi^{(f)}(x), \quad (2.1)$$
$$S_{\text{G}}[A] = \frac{1}{2g^2} \int d^4x \text{tr} [F_{\mu\nu}(x) F_{\mu\nu}(x)].$$

Quark fields are described by Dirac spinors $\psi_{a,\alpha}^{(f)}(x)$ at every point x in spacetime, and indices $a = 1, 2, 3$ and $\alpha = 1, 2, 3, 4$ label color and spin, respectively. Each field $\psi^{(f)}(x)$ thus has 12 independent components. The fields ψ and $\bar{\psi}$ are related by $\bar{\psi} = \psi^{\dagger} \gamma_0$. Like the mass matrix $m^{(f)}$, quark fields come in N_f different flavors.

The covariant derivative $D_{\mu} = \partial_{\mu} + \imath A_{\mu}(x)$ and the field strength tensor

$$F_{\mu\nu}(x) = \partial_{\mu} A_{\nu}(x) - \partial_{\nu} A_{\mu}(x) + \imath [A_{\mu}(x), A_{\nu}(x)] \quad (2.2)$$

contain the gauge fields $A_\mu^{ab}(x)$, representing the gluon fields. At every point x in spacetime they carry a Lorentz index $\mu = 1, 2, 3, 4$ and color indices $a, b = 1, 2, 3$, so that for a given x and μ , the field $A_\mu(x)$ is a traceless, hermitian 3×3 matrix. They are defined such that the QCD action is invariant under local $SU(3)$ gauge transformations. The field strength is not linear in the non-abelian gauge fields A_μ , but mixes the different color components of the gluon fields. This gives rise to nonlinear self interactions of the gluons and, eventually, leading to *confinement*, making QCD highly nontrivial. g denotes the bare coupling constant, which alternatively can be placed in the covariant derivative after rescaling the gauge fields, to make the coupling between quarks and gluons more obvious.

In order to compute an observable from a quantum field theory, an ultraviolet regulator is required to make expressions finite. While regulators in continuum perturbation theory are introduced by e.g. dimensional regularization or the Pauli-Villars regularization, a different approach is chosen here.

We replace the continuous Euclidean spacetime by a finite hypercubic lattice of points x , separated by a lattice spacing a

$$(x_0, x_1, x_2, x_3) \in \mathbb{R}^4 \rightarrow (x_0, x_1, x_2, x_3) \in \{0, 1, \dots, N-1\}^4. \quad (2.3)$$

The lattice itself serves as a regulator of the theory, as the shortest distance a defines an ultraviolet momentum cutoff π/a . Furthermore, path integrals (cf. (2.28)) become mathematically well defined due to the finite number of lattice sites. Hence, lattice QCD provides a non-perturbative definition of QCD. Physical results are recovered in the continuum limit $a \rightarrow 0$, while requiring the finite volume of the lattice to remain large enough $V \rightarrow \infty$ to contain the scales we are interested in.

In a naïve discretization, however, local gauge invariance will be lost. This becomes clear after the continuum derivative in (2.1) is replaced by a non-local discrete derivative

$$\partial_\mu \psi(x) \rightarrow \frac{1}{2a} (\psi(x + \hat{\mu}) - \psi(x - \hat{\mu})), \quad (2.4)$$

where $\pm \hat{\mu}$ labels the neighboring site in μ -direction, i.e. $\hat{\mu} = a \mathbf{e}_\mu$. As a result terms of the form $\bar{\psi}(x)\psi(x + \hat{\mu})$ occur, which are not gauge invariant as the fields transform according to

$$\psi(x) \rightarrow \psi'(x) = \Omega(x)\psi(x) \quad \text{and} \quad \bar{\psi}(x) \rightarrow \bar{\psi}'(x) = \bar{\psi}(x)\Omega(x)^\dagger, \quad (2.5)$$

where $\Omega(x)$ is an $SU(3)$ matrix. To preserve local gauge invariance on the lattice new fields $U_\mu(x) \in SU(N_c)$ are required to connect adjacent lattice sites x and $x + \hat{\mu}$. These so-called *link variables* are the analogue of the continuum gauge-transporters and are related to the gauge fields to first order a by

$$U(x, x + \hat{\mu}) = U_\mu(x) = \exp(i a A_\mu(x)). \quad (2.6)$$

Under a local gauge transformation $\Omega(x)$ the link variables transform according to

$$U_\mu(x) \rightarrow U'_\mu(x) = \Omega(x) U_\mu(x) \Omega(x + \hat{\mu})^\dagger \quad (2.7)$$

such that gauge invariance is obtained for neighboring fields by, e.g. $\bar{\psi}(x) U_\mu(x) \psi(x + \hat{\mu})$. The simplest possibility to construct a gauge invariant quantity on the lattice is the trace over the *plaquette* $U_{\mu\nu}(x)$, a closed loop of four link variables

$$U_{\mu\nu}(x) = U_\mu(x) U_\nu(x + \hat{\mu}) U_{-\mu}(x + \hat{\mu} + \hat{\nu}) U_{-\nu}(x + \hat{\nu}), \quad (2.8)$$

with $U_\mu = U_{-\mu}(x + \hat{\mu})^\dagger$. From here we recognize that the quark fields $\psi, \bar{\psi}$ live on the lattice sites and link variables, corresponding to the gauge fields, live on the links between the sites. Figure 2.1 presents a simple illustration of this concept.

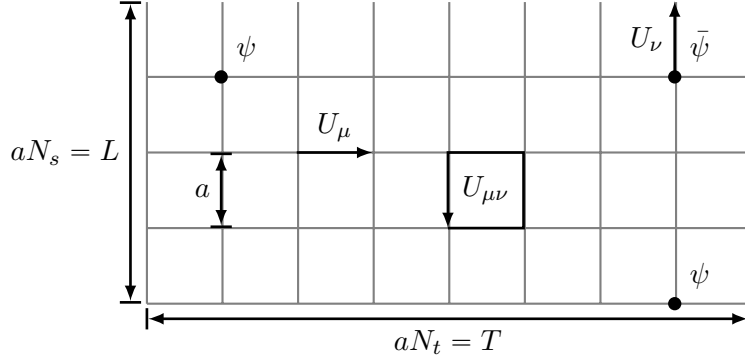


FIG. 2.1: Example of a 4×8 lattice with periodic boundary conditions. Spatial coordinates of fermion fields $\psi, \bar{\psi}$ and gauge links U are omitted. Objects like a plaquette $U_{\mu\nu}$ and a pair of fermion fields connected by a link are shown.

2.2 Lattice gauge action

After introducing the conceptual idea of lattice regularization, this section briefly addresses examples for discrete actions. These will turn into the continuum theory (2.1) for $a \rightarrow 0$, but not without certain issues. We mainly follow the pioneering work of Kenneth Wilson [1], adding further remarks when relevant for the upcoming chapters.

A simple construction of a lattice gauge action can be identified by using the plaquette,

$$S_G[U] = \frac{2}{g^2} \sum_x \sum_{\mu < \nu} \text{Re tr} [\mathbf{1} - U_{\mu\nu}(x)], \quad (2.9)$$

counting each loop on the lattice only once. The factor $2/g^2$ is included to match the continuum formulation and is often replaced by the inverse coupling

$$\beta = \frac{2N_c}{g^2}. \quad (2.10)$$

To see that the continuum theory is indeed recovered ($\lim_{a \rightarrow 0} S_G[U] = S_G[A]$) it is important to point out the relation between the link variables and the field strength tensor, i.e.

$$U_{\mu\nu}(x) = \exp(i a^2 F_{\mu\nu}(x) + \mathcal{O}(a^3)), \quad (2.11)$$

which is derived from(2.6) by applying the Baker-Campbell-Hausdorff formula. Eventually, we find

$$\begin{aligned}
S_G[U] &\simeq \frac{2}{g^2} \sum_x \sum_{\mu < \nu} \operatorname{Re} \operatorname{tr} [\mathbb{1} - \exp(i a^2 F_{\mu\nu}(x))] \\
&\simeq \frac{2}{g^2} \sum_x \sum_{\mu < \nu} \operatorname{Re} \operatorname{tr} \left[\mathbb{1} - \mathbb{1} + i a^2 F_{\mu\nu}(x) + \frac{1}{2} a^4 F_{\mu\nu}(x) F_{\mu\nu}(x) \right] \\
&= \frac{a^4}{2g^2} \sum_x \sum_{\mu, \nu} \operatorname{tr} [F_{\mu\nu}(x) F_{\mu\nu}(x)] + \mathcal{O}(a^2).
\end{aligned} \tag{2.12}$$

The continuous and discrete version of the gauge action thus agree up to $\mathcal{O}(a^2)$ discretization effects, originating from the expansion of the gauge fields in the plaquette.

Infinitely many more terms do exist but are suppressed by increasing powers of the lattice spacing. Similarly, one may add any terms that vanish in the continuum limit without changing continuum physics. As a consequence, the lattice action is not unique, only the classical limit is. This is utilized in the construction of *improved* lattice actions, which attempt to further reduce discretization effects.

One example for an improved action is the *Lüscher-Weisz* gauge action [40, 41]. In addition to the plaquette also rectangular planar loops $U_{\mu\nu}^{1 \times 2}(x)$ are included in such a way that leading order discretization errors are subtracted

$$S_G^{\text{improv.}}[U] = \frac{\beta}{3} \sum_x \left((1 - 8c_1) \sum_{\mu < \nu} \operatorname{tr} [\mathbb{1} - U_{\mu\nu}^{1 \times 1}(x)] + c_1 \sum_{\mu \neq \nu} \operatorname{tr} [\mathbb{1} - U_{\mu\nu}^{1 \times 2}(x)] \right). \tag{2.13}$$

The coefficient c_1 takes different values for various choices of the improved actions. For an approach based on the renormalization group transformations, the *Iwasaki* gauge action [42, 43] requires $c_1 = -0.331$, for a tree-level improved action, the *Symanzik* framework [40] requires $c_1 = -1/12$. Wilsons standard formulation (2.9) is restored at $c_1 = 0$. Computations throughout this thesis will employ the Iwasaki gauge action.

2.3 Wilson fermions

For the fermionic part of the action, the most prominent discretization is the Wilson fermion action. It appears in Wilson's first lattice formulation and deals with an issue that the naïve lattice formulation faces. By introducing an additional term to the action it gets rid of the so-called *fermion doubling*. This expression labels the appearance of additional $2^d - 1$ fermionic particles when fermion fields are naïvely placed on a d -dimensional lattice.

They correspond to additional poles of the inverse lattice Dirac operator in momentum space. The naïve Dirac operator on the lattice is given by

$$\left(D_{\text{naïve}}^{(f)} \right)_{a, \alpha; b, \beta}(x; y) = \frac{1}{2a} \sum_{\mu=\pm 1}^{\pm 4} (\gamma_\mu)_{\alpha\beta} U_\mu(x)_{ab} \delta(x + \hat{\mu}, y) + m^{(f)} \delta_{\alpha\beta} \delta_{ab} \delta(x, y), \tag{2.14}$$

where we define the convenient notation $\gamma_{-\mu} = -\gamma_{\mu}$. In the free theory ($U_{\mu} \equiv \mathbb{1}$) with massless fermions we can obtain analytical expressions for the Dirac operator and its inverse, the *quark propagator*. In momentum space they read

$$\tilde{D}_{\text{naïve}}(p)\Big|_{m=0} = \frac{\imath}{a} \sum_{\mu=1}^4 \gamma_{\mu} \sin(p_{\mu}a), \quad (2.15)$$

$$\tilde{D}_{\text{naïve}}^{-1}(p)\Big|_{m=0} = \frac{-\imath a^{-1} \sum_{\mu} \gamma_{\mu} \sin(p_{\mu}a)}{a^{-2} \sum_{\mu} \sin(p_{\mu}a)^2} \xrightarrow{a \rightarrow 0} \frac{-\imath \sum_{\mu} \gamma_{\mu} p_{\mu}}{p^2}. \quad (2.16)$$

Although the momentum space propagator has just a single pole in the continuum, the situation is different on the lattice. Whenever all components of p_{μ} are either 0 or π/a , a pole is met, cf. Figure 2.2. These additional fermions cannot be ignored and will eventually contribute with incalculable effects to our finite volume measurements.

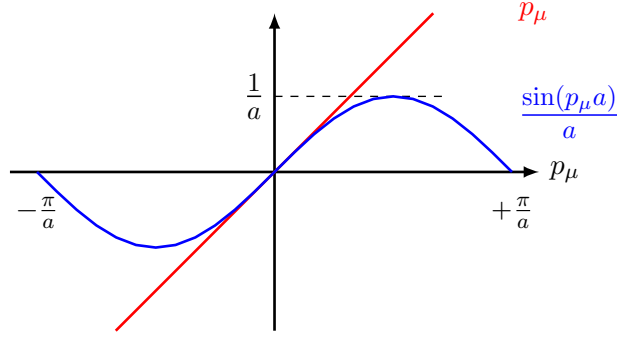


FIG. 2.2: Plot of p_{μ} (red) and $\sin(p_{\mu}a)/a$ (blue) as functions of $p_{\mu} \in (-\pi/a, \pi/a]$ in the Brillouin zone. Zeroes of the sine function at the corners of the Brillouin zone give rise to lattice artifacts.

Introducing the so-called *Wilson term* to the naïve momentum space Dirac operator resolves the issue smoothly

$$\tilde{D}(p) = \frac{\imath}{a} \sum_{\mu=1}^4 \gamma_{\mu} \sin(p_{\mu}a) + \mathbb{1} \frac{1}{a} \sum_{\mu=1}^4 (1 - \cos(p_{\mu}a)) + m\mathbb{1}. \quad (2.17)$$

It simply vanishes for the physical pole at $p = (0, 0, 0, 0)$ and every unphysical pole obtains an additional mass term $\sim 1/a$ so that they decouple from the theory if we send $a \rightarrow 0$. Finally we arrive at the Wilson fermion action

$$S_F^{\text{Wilson}}[\psi, \bar{\psi}, U] = \sum_{f=1}^{N_f} a^4 \sum_{x,y} \bar{\psi}^{(f)}(x) D^{(f)}(x; y) \psi^{(f)}(y), \quad (2.18)$$

with a Wilson Dirac operator of the form

$$D_{a,\alpha;b,\beta}^{(f)}(x; y) = -\frac{1}{2a} \sum_{\mu=\pm 1}^{\pm 4} (\mathbb{1} - \gamma_{\mu})_{\alpha\beta} U_{\mu}(x)_{ab} \delta(x + \hat{\mu}, y) + \left(m^{(f)} + \frac{4}{a} \right) \delta_{\alpha\beta} \delta_{ab} \delta(x, y). \quad (2.19)$$

An important symmetry of this Dirac operator later on is the γ_5 -hermiticity

$$D^\dagger = \gamma_5 D \gamma_5. \quad (2.20)$$

This symmetry is passed on to its inverse, the quark propagator, which allows us to drastically simplify the calculations of correlation functions later on. Furthermore, the eigenvalues of the Dirac operator are, as a consequence, either real, or come in complex conjugate pairs. This implies a real fermion determinant, a feature crucial for Monte Carlo simulations of lattice QCD.

A major disadvantage of the Wilson action is that it breaks chiral symmetry explicitly, even for massless quarks. This is caused by the additional mass term introduced to remove the doublers, cf. (2.19). The loss of chiral symmetry and the requirement to remove doublers are two circumstances that are closely connected to each other. As it is stated in the *Nielsen-Ninomiya theorem* [44, 45] any discrete Dirac operator cannot have the following properties simultaneously:

1. Locality:
 $D(x; y)$ is *local*, i.e. bound by $e^{-\gamma|x-y|}$ with $\gamma \in \mathbb{R}^+$
2. Correct low momentum limit:
 For $p \ll \pi/a$: $\tilde{D}(p) = v\gamma_\mu p_\mu + \mathcal{O}(a^2 p^2)$
3. No doublers:
 $\tilde{D}(p)$ invertible for $p \neq 0$
4. Chiral:
 $\{D, \gamma_5\} = 0$

While the Wilson action knowingly sacrifices chiral symmetry, other discretizations like *staggered fermions* [46, 47] choose to hold on to it. By distributing the four components of the Dirac spinor to different lattice sites and distinguishing between “tastes” the doublers are controlled. Very subtle effects, like the spontaneous breaking of chiral symmetry, can then be investigated on the lattice.

A possible solution to recover the chiral limit without doublers is proposed by the *Ginsparg-Wilson equation* [48]. It replaces the continuum relation by the weaker condition

$$\{D, \gamma_5\} = aD\gamma_5D, \quad (2.21)$$

such that chiral symmetry is restored in the continuum. Approaches like *overlap* [49, 50] and *domain wall fermions* [51, 52] solve this condition precisely, but are extremely demanding in the required computational power. Approximate solutions for (2.21) are achieved by e.g. *chirally improved fermions* [53, 54].

We stick to the Wilson fermion action, but, similar to the gauge action, want to improve it by an additional term. Following the Symanzik improvement scheme [55], this is achieved by adding the clover term to the Wilson fermion action

$$S_F^{\text{SW}} = S_F^{\text{Wilson}} + c_{\text{SW}} a^5 \sum_{x, \mu < \nu} \bar{\psi}(x) \frac{1}{2} \sigma_{\mu\nu} F_{\mu\nu}^{\text{SW}}(x) \psi(x). \quad (2.22)$$

The coefficient c_{SW} has to be tuned in such a way that $\mathcal{O}(a)$ effects vanish for on-shell quantities. To achieve this non-perturbatively, suitable improvement conditions [56, 57, 58] need to be imposed. Note that the coefficient also affects the renormalization of the bare quark mass and bare coupling. The realization of the lattice field strength tensor by four plaquettes sharing the same lattice site takes the shape of a clover leaf, and gives this term its name:

$$\begin{aligned} F_{\mu\nu}^{\text{SW}}(x) &= \frac{-i}{8a^2} (Q_{\mu\nu}(x) - Q_{\nu\mu}(x)), \\ Q_{\mu\nu}(x) &\equiv U_{\mu,\nu} + U_{\nu,-\mu} + U_{-\mu,-\nu} + U_{-\nu,\mu}. \end{aligned} \quad (2.23)$$

For small couplings the coefficient can also be computed perturbatively [59].

Another realization of an improved Wilson fermion action is the *Wilson twisted mass* [60, 61, 62] formulation. The additional term to the actions corresponds there to a chiral rotation in flavour space under the requirement of pairs of degenerate flavors. It can be shown that this action provides an automatic $\mathcal{O}(a)$ improvement if the chiral rotation is at maximal twist.

Finally, we want to expand the Dirac operator in its inverse quark mass. This procedure is the so-called *hopping-parameter* expansion and is considerably convenient for numerical simulations. After defining the hopping parameter κ and rescaling the fermion fields

$$\kappa = \frac{1}{2(am + 4)}, \quad \psi \rightarrow \sqrt{m + \frac{4}{a}} \psi, \quad \bar{\psi} \rightarrow \sqrt{m + \frac{4}{a}} \bar{\psi}, \quad (2.24)$$

one can rewrite the single flavor Dirac operator in its matrix representation by

$$D(x; y) = \mathbf{1} - \kappa H(x; y). \quad (2.25)$$

The hopping matrix $H(x; y)$ connects the nearest neighboring sites, cf. (2.19)

$$H(x; y)_{a,\alpha;b,\beta} = \sum_{\mu=\pm 1}^{\pm 4} (\mathbf{1} - \gamma_{\mu})_{\alpha\beta} U_{\mu}(x)_{ab} \delta(x + \hat{\mu}, y), \quad (2.26)$$

and the quark propagator can be expanded in powers of κ

$$D^{-1} = (\mathbf{1} - \kappa H)^{-1} = \sum_{n=0}^{\infty} \kappa^n H^n. \quad (2.27)$$

Each power of H hence adds another layer of separations between two points through various series of link variables. They correspond to the shortest paths between the points and due to the earlier defined notation of $\gamma_{-\mu} = -\gamma_{\mu}$ and $(\mathbf{1} - \gamma_{\mu})(\mathbf{1} - \gamma_{-\mu}) = 0$ back-tracking paths are excluded. Thus, the full quark propagator at $(x; y)$ is the sum of all fermion lines connecting x and y . The fermion determinant can be rewritten in a similar manner.

2.4 Path integrals from the lattice

Expectation values of observables are determined by the path integral over all possible field configurations $\int \mathcal{D}[\psi, \bar{\psi}, U]$, weighted by a Boltzmann factor containing the action. For two field operators O_i at times t and 0 the vacuum expectation value is defined as

$$\begin{aligned} \langle 0|O_1(t)O_2(0)|0\rangle &= \langle O_1(t)O_2(0)\rangle = \frac{1}{Z} \int \mathcal{D}[\psi, \bar{\psi}, U] O_1[\psi, \bar{\psi}, U] O_2[\psi, \bar{\psi}, U] e^{-S_{\text{QCD}}}, \\ \text{with } Z &= \int \mathcal{D}[\psi, \bar{\psi}, U] e^{-S_{\text{QCD}}}, \end{aligned} \quad (2.28)$$

and will later be used to compute the mass of meson groundstates. The partition function Z denotes the chosen normalization. The path integral quantization translates the field operators $O_i(t)$, acting in Hilbert space, into functionals of field variables $O_i[\psi, \bar{\psi}, U]$. They depend on the fields with the corresponding time argument.

Separating the QCD action into its fermionic and gluonic part we write the path integrals conveniently in angled brackets with a suited index

$$\langle O_1 O_2 \rangle = \frac{1}{Z} \int \mathcal{D}U e^{-S_G[U]} \left(\int \mathcal{D}[\psi, \bar{\psi}] e^{-S_F[\psi, \bar{\psi}, U]} O_1 O_2 \right) \equiv \langle\langle O_1 O_2 \rangle\rangle_F \rangle_U, \quad (2.29)$$

and consider in a first step the integration over the fermion fields. This integration is often referred to as *fermion contraction*.

2.4.1 Fermion contraction

The quark fields $\psi^{(f)}$, $\bar{\psi}^{(f)}$ are represented by anti-commuting Grassmann variables to respect Fermi statistics. They are treated as independent fields when integrating and the definition of the integration of Grassmann valued fields can be found in e.g. [35]. The integration in (2.29) can be performed analytically and one obtains for the Gaussian integral with Grassmann valued fields

$$\langle O_1 O_2 \rangle_F = \prod_f \det D^{(f)}[U] O_{12}[(D^{(f)})^{-1}, U]. \quad (2.30)$$

O_{12} is a functional of quark propagators and link variables. Its spin, color and spacetime structure is given by the operators on the left hand side. Quark propagators appear as a result of contracting every occurring expectation value of a fermion and anti-fermion field, for all flavors and all possible permutations of expectation values. A product of *fermion determinants* $\det(D^{(f)})$ with the respective quark flavors is a consequence of the transformation properties of the measure in the Grassmann integration. Each determinant can be interpreted as the collective creation and annihilation of quark pairs from the vacuum. They are eventually included as a distribution weight in the partition function

$$Z = \int \mathcal{D}[U] e^{-S_G[U]} \prod_f \det D^{(f)}[U] = \int \mathcal{D}[U] e^{-(S_G[U] - \sum_f \ln(\det(D^{(f)}))}, \quad (2.31)$$

which will become more relevant later on when the path integral is described by stochastic methods, and a probability distribution of the gauge fields needs to be determined. In the second step of (2.31) we defined an *effective action* S_{eff} as distribution weight. To indicate a performed integration over fermionic fields we write

$$\langle\langle O_1 O_2 \rangle\rangle_F \rangle_U \xrightarrow{D[\psi, \bar{\psi}]} \langle O_{12}[(D^{(f)})^{-1}, U] \rangle_U = \frac{1}{Z} \int \mathcal{D}U e^{-S_{\text{eff}}[U]} O_{12}[(D^{(f)})^{-1}, U], \quad (2.32)$$

and imply the presence of fermionic contributions to the gauge integration. The fermionic expectation value of a fermion and anti-fermion field, i.e. a two-point function of fermions, is written in the employed short hand notation as

$$\langle \psi_{a,\alpha}^{(f)}(x) \bar{\psi}_{b,\beta}^{(f)}(y) \rangle_F = a^{-4} (D^{(f)})_{a,\alpha;b,\beta}^{-1}(x; y). \quad (2.33)$$

Quark propagators $(D^{(f)})^{-1}$ are the major components of the functionals on the right hand side of (2.30) and thus are essential for the computation of hadronic observables. The full quark propagator, which connects all sites of the lattice with each other, is however a huge quantity and it is not feasible to compute it explicitly. Storing such a matrix on a typical lattice with a size of $32^3 \times 64$ sites, turns out to be equally undesirable:

$$(3 \times 4 \times (32^3 \times 64))^2 \times 2 \times 8 \text{ bytes} \approx 10 \text{ petabytes}. \quad (2.34)$$

Moreover, such propagators are required for multiple realizations of the gauge field, every quark mass and ultimately, is one quark propagator per gauge field per mass not sufficient to study modern problems.

Instead we are going to compute estimations of the full quark propagator by the use of quark sources. In the simplest realization one could think of computing only a single spatial column of the full propagator. This column will then describe the propagation from one fixed lattice site to all lattice sites and hence reduces the numerical effort drastically. Due to spatial translational invariance of QCD this might be sufficient for the problem at hand. To obtain such a column ϕ a linear system of the form

$$D^{(f)} \phi^{(f)} = \xi, \quad (2.35)$$

has to be solved, involving the Dirac matrix D and a suited source term ξ . The systematic construction of quark propagators will play a major role in the later parts of this work. How this linear system is solved and which other strategies are utilized at this point are discussed in Chapter 3.

What remains is the integration over all gauge field configurations in (2.32). Even though the degrees of freedom are finite on the lattice, their total number remains too large to be solved explicitly. Monte Carlo techniques to solve such high dimensional integrals are discussed in the following section.

2.4.2 Gauge field Configurations

To solve integrals of the form (2.32) it is not required to know the whole space of all possible gauge field configurations. If $S_{\text{eff}}[U]$ is positive definite, each gauge field is

weighted by a factor $\exp(-S_{\text{eff}}[U])$ so that only a small subset of configurations, those which are close to minimizing the action, will have a crucial impact to the integral. Contributions from the vast majority of configuration space are suppressed exponentially.

From a numerical point of view we are only interested in sampling this small subset of vital contributions. To obtain them from the large configuration space an importance sampling is employed. Configurations are subsequently sampled according to a path which follows a probability distribution only dependent on the current state $P(U_i) \propto \exp(-S_{\text{eff}}[U_i])$, the so-called *Markov chain*. Within a Markov chain conditions to the transition probabilities $P_{i \rightarrow j}$, from one to another state, are set so that every state within the configuration space can be reached within a finite number of steps, i.e.

$$\sum_j P_{i \rightarrow j} = 1, \quad (2.36)$$

where $P_{i \rightarrow j} \in [0, 1]$ labels the transition probability to go from $U_i \rightarrow U_j$. The equilibrium distribution of states within the Markov chain is then equivalent to the desired distribution $\exp(-S_{\text{eff}}[U_i])$. The number of steps taken until an equilibrium is reached is called thermalization. Only within the region of thermalized configurations can we expect to measure physical observables. By construction this region will be reached eventually so that also *detailed balance*

$$P(U_i)P_{i \rightarrow j} = P(U_j)P_{j \rightarrow i}, \quad (2.37)$$

is employed as a additional condition to the transition probabilities in order to guarantee the reversibility of the equilibrated system.

Probably the most well-known algorithm to generate gauge field configurations along the Markov chain is the *Metropolis algorithm*. Here one differentiates between a Metropolis step, which is the update of a single link variable, and a Metropolis sweep, which is the update of all link variables on the lattice. An update of the link variable $U_\mu(x)$ is of the form

$$U'_\mu(x) = X U_\mu(x), \quad (2.38)$$

where the random $X \in SU(N_c)$ are chosen carefully to provide an appropriate change within the configuration space. Both X too close and too far away from unity will slow down the convergence of the Markov chain drastically.

The Metropolis algorithm starts from an arbitrary configuration. Every step that results in an effective action which is smaller compared to the current situation is accepted and replaces the current action. A larger action is only accepted with a probability taking into account the anticipated loss in the action, if a step is rejected the current state will be kept

$$P_{i \rightarrow j}^{\text{accept}} = \min(1, \exp(-(S_{\text{eff}}[U_j] - S_{\text{eff}}[U_i]))). \quad (2.39)$$

This selection process fulfills the detailed balance condition (2.37) and as stated above allows for multiple states along the equilibrium distribution of the Markov chain.

Eventually one ends up with a set of N_{conf} configurations distributed to minimize

the present effective action, so that the integral (2.32) can be computed as

$$\begin{aligned} \langle O_{12}[(D^{(f)})^{-1}, U] \rangle_U &= \lim_{N \rightarrow \infty} \frac{1}{N} \sum_{i=1}^N e^{-S_{\text{eff}}[U_i]} O_{12}[(D^{(f)})^{-1}, U_i] \\ &\approx \frac{1}{N_{\text{conf}}} \sum_{\substack{U_n \text{ with} \\ \text{probability} \\ \propto e^{-S_{\text{eff}}[U_n]}}}^{N_{\text{conf}}} O_{12}[(D^{(f)})^{-1}, U_n]. \end{aligned} \quad (2.40)$$

A set of N_{conf} gauge field configurations with little to no correlation, generated from the same configuration space, is referred to as gauge field ensemble.

An order of thousands of Metropolis sweeps might be necessary to reach the thermalized region. On top of that several sweeps between thermalized configurations are discarded as well, as they are not statistically independent. Hence it becomes evident that the numerical effort to generate a gauge field ensemble of reasonable extent is a tremendous computational task.

Important to mention is the crucial role of the fermion determinants throughout this process. In (2.31) we constructed an effective action with a product over all fermion determinants as a probability weight for the gauge field integration. If we want to interpret it as such this product has to be real and nonnegative. There are indeed scenarios, e.g. when introducing a chemical potential, where the fermion determinants are complex and standard Monte Carlo methods are not anymore applicable (the so called sign problem, see e.g. [63] and references therein).

A pair of mass degenerate quark flavors with a γ_5 -hermitian Dirac operator (2.20) meet the conditions

$$\det[D] \det[D] = \det[D] \det[D^\dagger] = \det[DD^\dagger] \geq 0. \quad (2.41)$$

Even after fulfilling the conditions to serve as a probability weight, the inclusion of fermion determinants to the gauge field integration poses a considerable numerical effort. Not only is their computation highly non-trivial, c.f. (2.25), they are also connecting all link variables on the lattice with each other, making them highly non-local objects. A change in a single link variable during a Monte Carlo step will hence affect the whole determinant and require a new computation for every small change. This effort increases for larger lattices or smaller quark masses.

Local gauge link updates (2.38) are obviously not efficient enough to handle such non-local quantities. Instead different methods are used in modern simulations where global updates of the gauge field allow simulations with dynamical fermions. The Hybrid Monte Carlo algorithm [64], for example, applies a molecular dynamics evolution by introducing conjugate momenta to the gauge links. The evolution of the system along directions determined by the action is then combined with a Metropolis accept/reject step to yield the desired probability distribution.

An alternative, numerically less demanding approach is realized with the so-called *quenched approximation*. Fermion determinants are set to a constant such that the integration in (2.31) is only governed by the gauge action. Updates of link variables do

then become local operations and the computation of the difference in the respective actions reduces to the six plaquettes directly affected by the update. In terms of the earlier given interpretation, such an approximation neglects the creation and annihilation of quarks from the vacuum.

2.5 Correlation functions

To compute observables from the lattice the *correlation function* plays a central role. First encountered in (2.28) it is shown within this chapter that the computation of such a two-point function is well within the range of our numerical capabilities. Eventually a correlation function can be computed on the lattice applying (2.40), i.e. as a mean of quark propagators and gauge links over a given set of gauge field configurations.

Defined as the functional average of two interpolating field operators, a correlation function can be interpreted as the amplitude of a propagating particle. Complementary to its formulation as a path integral it is equally important to consider the two operators $O_1(t)$ and $O_2(0)$ in Hilbert space. Exploiting the periodicity on the torus these are conveniently placed at times t and 0 , respectively. They create and annihilate states of certain quantum numbers. The temporal evolution is then conveniently extracted through the Hamiltonian H of the system and the correlation function becomes

$$\langle O_1(t)O_2(0)^\dagger \rangle_T = \frac{1}{Z_T} \text{tr} \left[e^{-(T-t)H} O_1 e^{-tH} O_2^\dagger \right]. \quad (2.42)$$

$Z_T = \text{tr} [e^{-TH}]$ is the partition function, which turns into a sum over the exponentials of all energy eigenvalues, eventually. Index T indicates the finite temporal lattice extent. Rewriting the trace by eigenstates of the Hamiltonian and inserting a complete orthonormal basis, i.e.

$$H|n\rangle = E_n|n\rangle, \quad \text{tr}[O] = \sum_n \langle n|O|n\rangle, \quad \mathbb{1} = \sum_n |n\rangle\langle n|, \quad (2.43)$$

we find

$$\langle O_1(t)O_2(0)^\dagger \rangle_T = \frac{1}{Z_T} \sum_{m,n} \langle m|e^{-(T-t)H} O_1 |n\rangle \langle n|e^{-tH} O_2^\dagger |m\rangle. \quad (2.44)$$

For the limit $T \rightarrow \infty$, where we are far away from any boundary, only the vacuum energy $E_m = E_0$, or vacuum contributions $|m\rangle = |0\rangle$ remain. By pulling out a factor of $e^{-E_0 T}$ both in the numerator and denominator we obtain energy differences relative to the energy of the vacuum $\Delta E_n = E_n - E_0$. Finally, one ends up with one of the most prominent identities of lattice hadron spectroscopy

$$\lim_{T \rightarrow \infty} \langle O_1(t)O_2(0)^\dagger \rangle_T = \sum_n \langle 0|O_1|n\rangle \langle n|O_2^\dagger|0\rangle e^{-\Delta E_n t}. \quad (2.45)$$

For practical reasons energy differences to the vacuum are simply denoted by E_n hereafter. This effectively normalizes the energy of the vacuum to zero, with E_0 being the lowest possible excitation, i.e. the groundstate.

We find that the correlation function is a sum of products of amplitudes and exponential functions governed by the respective energy levels. The quantum numbers of the $O_i^\dagger|0\rangle$ determine the spectrum of states. While the sum in (2.45) runs over all possible states $|n\rangle$ only those that have a nonvanishing overlap with the trial states $O_i^\dagger|0\rangle$ will contribute. Simply put, energy spectra of particles are then analyzed by computing the path integral (2.40) of $\langle O_1(t) O_2(0) \rangle$ and comparing it to the right hand side of (2.45).

2.6 Towards the continuum

Although the continuum limit of presented results will not be studied, a brief outline of the procedure is given in this section. With every lattice simulation performed at certain *dimensionless* values for the lattice extent, spacing and bare quark masses it is necessary to *set the scale* in order to provide a physical interpretation of these values (see Section 2.7: “Setting the scale”). Once observables can be associated with physical values one wants to leave the discrete world behind and send $a \rightarrow 0$. Doing so, the physical volume of the box $\propto a^4$ must not shrink to zero. Additionally, bare quark masses commonly do not relate to physical quark masses as well, leaving us effectively with three distinct limits to study.

2.6.1 Infinite volume limit

With the goal to send $a \rightarrow 0$ one would also have to send the number of lattice sites to infinity in order to preserve the physical volume, also known as the *thermodynamic limit*. As this is not feasible from a numerical point of view, the discussion quickly revolves around whether lattices are *large enough*. More precisely, this criterion concerns whether computations are affected by finite size effects. Indeed exponential corrections to hadron masses occur due to interactions around the spatial torus [16]. These are governed in leading order by the mass of the lightest hadron, i.e. the pion $\propto \exp(-m_\pi L)$. It is usually assumed that such corrections are small for $m_\pi L > 4$. The spatial lattice extent gains additional relevance in modern studies of multi-particle systems. Similar to the just mentioned corrections do two particles interact with each other in both directions around the torus. Not only does this affect possible multi-particle states, but also a correspondence between the scattering phase shift and the spatial volume as been found by M. Lüscher [17]. Commonly known as Lüscher’s method it has gained increased attention in the study of resonances within recent years.

2.6.2 Continuum limit

Observables computed on the lattice contain undesired contributions due to the finite resolution of spacetime. The mass of a particle measured on the lattice then differs from its continuous version by

$$m(a) = m_{\text{phys}} (1 + \mathcal{O}(a^\alpha)). \quad (2.46)$$

The factor α strongly depends on the choice of the (fermion) action, as well as on the particle under investigation. To reach the continuous version of the obtained result usually three to four values in a are considered, where $a \rightarrow 0$. In the context of gauge

field configurations this is equivalent to increasing $\beta \rightarrow \infty$. As it has been pointed out above, $a = 0$ does not depict a valid option so an extrapolation remains mandatory. These extrapolations are made on lines of constant physics, i.e. ideally under a preserved physical volume, quark masses, etc. As this is not always realized in practice it is then to ensure that finite size effects on observables are under control.

2.6.3 Chiral limit

Up to this point towards the continuum, the observables of interest suffer only from negligible finite size effects and are studied for several $a \rightarrow 0$. What still remains are the unphysically heavy quark masses of the simulation. Although they can not be measured directly they are tuned by the bare quark mass parameter of the simulation. Eventually one would like to reach the point where the light quark masses generate a *physical pion* of roughly 140MeV. The physical pion is hence used as a synonym for physical (light) quark masses. However, we have seen throughout this chapter that the pion mass is substantial for a multitude of processes and effects. Lattice computations aimed at physical values become tremendously expensive as the number of lattice sites has to increase drastically to control finite size effects. Furthermore, eigenvalues of the Dirac operator are smaller for lighter quark masses which increases the numerical effort as well. In hadron spectroscopy, physical pions will progressively decrease energy thresholds, possibly altering the picture entirely.

As a consequence, modern lattice QCD calculations still bear pion masses higher than observed in nature, often also with a degeneracy of the u and d quark. Similar to the continuum limit, an extrapolation to physical values remains necessary. Typically *chiral perturbation theory* is utilized for such extrapolations in the quark mass. The low energy effective theory provides expansion series of hadronic quantities in low energy quantities, like the quark mass. These have to be fixed by either experiment or lattice data and hence allow the exploration of physical values. However, with an increasing progress in the development of more powerful hardware, computations very near to the physical values are well within reach, e.g. [65]. Simple extrapolations from lattice data are then in principle enough to obtain the quantities of interest at the physical point.

For an example, the authors of [7] essentially compute their observables of interest on three lattice spacings, with three different pion masses ranging between 230 - 470 MeV on two discretizations. They employ the Wilson twisted mass fermion action and thus expect improved discretization errors $\propto a^2$ for their results. Finite volume effects are studied for two spatial extents and found to be negligible, further the typical linear behavior of masses in m_π^2 is assumed (usually the leading order in chiral perturbation theory). Their most general fitting function for the combined chiral and continuum limit is then

$$m(a, m_\pi) = m + c a^2 + \alpha (m_\pi^2 - m_{\pi \text{exp}}^2), \quad (2.47)$$

where m is shared between the discretizations, c.f. (2.46). Eventually, a total of 18 lattice QCD masses $m^\pm(a, m_\pi)$ is identified by five fitting parameters m, c^\pm, α^\pm (\pm indicating the two discretizations). Overall very solid results are obtained, especially for the heavier charmonium states. Plots depicting the combined chiral and continuum extrapolation of

states in m_π^2 demonstrate nicely the lines of constant physics, which have been mentioned above.

2.7 Setting the scale

It is important to note that the lattice spacing a is not a parameter of any lattice QCD simulation. The lattice action does not explicitly depend on a . It occurs in the action solely to provide the correct dimensionality and can be absorbed in the fields. Instead it emerges from the inverse coupling β (2.10), i.e. $a \sim \beta^{-1}$ and appears together with the quark masses to form dimensionless quantities am_q .

In order to relate the results of a lattice calculation to physical units it is therefore necessary to determine the physical length of the lattice spacing a . This is done by computing an observable to high precision with lattice methods, which is also well measured by experimental results. While there are many possible choices for said observable we focus on a prominent one, which was also used to set the scale for the gauge field configurations used in this work. Other possibilities are mentioned to give a broader view.

To determine the lattice scale for “ $N_f = 2 + 1$ Lattice QCD simulations toward the physical point” [65] the *Sommer parameter* r_0 [66] is used. This approach is linked to phenomenology where sufficiently heavy quark-antiquark bound states are described by an effective nonrelativistic Schrödinger equation. Given the static quark-antiquark potential

$$V(r) = V_0 + \frac{\alpha}{r} + \sigma r, \quad (2.48)$$

the force between two static quarks $F(r)$ can be calculated on the lattice and then compared to experimental results. For the heavy spectra this gives rise to a value of

$$F(r_0) r_0^2 = \left. \frac{dV(r)}{dr} \right|_{r=r_0} r_0^2 = 1.65 \quad \text{with} \quad r_0 \simeq 0.5 \text{ fm}. \quad (2.49)$$

The Sommer parameter r_0 can then be calculated from the numerical data of $V(r)$

$$r_{0, \text{lat.}} = \sqrt{\frac{1.65 + \alpha}{\sigma a^2}} = \frac{r_0}{a}, \quad (2.50)$$

which can be extracted by linear fits to the logarithm of *Wilson loops*¹ $W(r, t) = C(r) \exp(-V(r)t)$, i.e. the effective potential $V_{\text{eff}}(r, t) = \ln[W(r, t)/W(r, t+a)]$. Note that $r_{0, \text{lat.}}$ does not depend on a as $aV(r)$ is calculated on the lattice, leaving σa^2 as a fitting parameter.

In [65] also hadronic observables are taken into account, providing an extrapolated result for the Sommer parameter at the physical point of $r_{0, \text{lat.}} = 5.427(51)(+81)(-2)$, which is $r_0 = 0.4921(64)(+74)(-2)$ fm in physical units with the use of

$$a = 0.0907(13) \text{ fm} \Leftrightarrow a^{-1} = 2.176(31) \text{ GeV}. \quad (2.51)$$

¹ $C(r)$ denotes the ground state overlap

The first error in the Sommer parameter is statistical and the latter two are systematic uncertainties, originating from different choices of t_{\min} and r_{\min} in the respective fitting procedures. Since the exact value of r_0 is not determined precisely by experiment it varies throughout different groups in the lattice community. Choices usually vary from 0.48, 0.49 to 0.50 fm [67, 68] when fixing the scale directly from the quark-antiquark potential, chiral and/or continuum extrapolations vary the parameter slightly.

Similarly, alternative approaches which do not utilize the quark-antiquark potential often obtain an extrapolated Sommer parameter. The relevant condition is still that the observable of choice allows precise computation on the lattice and measurement in experiment. Fulfilling the criteria of a low quark mass dependence the Ω baryon is a prominent choice for a hadronic observable [69, 70] with a good signal to noise ratio for a non pseudoscalar observable and no need for a renormalization constant for m_Ω . In [69] $r_0 m_\Omega$ is extrapolated to the physical point and a value for the Sommer parameter of $r_0 = 0.471(14)(10)$ fm is found. The nucleon is used in [71, 72] and $r_0 = 0.465(6)(15)$ fm and $r_0 = 0.501(10)(11)$ fm are found as the corresponding extrapolations at the physical point, respectively. Pseudoscalar observables like decay constants f_π, f_K [73, 74, 75] provide an excellent signal to noise ratio. Applying chiral perturbation theory formulae to their fitting methodology of observables with physical m_π and f_π as input, e.g. [73] obtains $r_0 = 0.454(7)$ fm.

3

MESON SPECTROSCOPY

In this chapter we discuss how to obtain the mass spectrum of mesonic states from the lattice approach. In particular, the motivation to investigate possible tetraquark candidates will be of central relevance. Given the requirement that a well-suited gauge field ensemble is at hand, the measurement of ground state energies is in general a straightforward task. In Section 3.1 we illustrate on the example of the $a_0(980)$ that the situation becomes much more delicate for exotic mesons. These are to be found in the vicinity of two-particle states and thus require the resolution of the full two-particle spectrum. To extract a whole spectrum of states we use the variational approach, introduced in Section 3.2. In Section 3.3 we motivate the interpolator set that is employed to model the expected particles in the spectrum. Among these also trial states are designed to investigate a possibly existing four-quark structure of bound states, i.e. mesonic molecules or of diquark-antidiquark type. The various resulting correlation functions have a non-trivial spacetime structure and are no longer straightforward to compute. We proceed in Section 3.4 with the technical aspects to estimate quark propagators on the lattice and describe in great detail how to employ several standard and advanced techniques. Throughout this study we work with spatially extended quark operators. These improve the overlap to the expected physical states. Section 3.5 closes this chapter and presents the employed smearing techniques.

3.1 Multi-particle correlators

Although we briefly introduced correlation functions and pointed out their role in computing hadronic quantities in Section 2.5, we continue the discussion here. More precisely, we want to expand on issues that arise while investigating possible tetraquark candidates. We know from equation (2.45)

$$C(t) = \sum_n |\langle 0|O|n\rangle|^2 e^{-E_n t},$$

that the correlation function at separation t is a sum over all states $|n\rangle$ with quantum numbers that have nonvanishing overlap with $O^\dagger|0\rangle$. If excitations or multiparticle states are well separated from the groundstate they are suppressed exponentially. A simple exponential fit at large separations is then often sufficient to extract the energy of the groundstate from the correlator. To reveal for which separations in t only a single

exponential contributes so-called *effective masses* are utilized. Defined as

$$a m_{\text{eff}}(t) = \ln \left(\frac{C(t)}{C(t+a)} \right), \quad (3.1)$$

the values of the effective mass are typically below the ultraviolet cutoff of the lattice and convenient to study, i.e. $am_{\text{eff}}(t) \in [0, 1]$. At temporal separations, where the correlator is governed by a single exponential, this value approaches a plateau in t . Stable plateau values with little statistical fluctuations between t_{min}/a and t_{max}/a are then well suited to locate a suitable fitting range for the respective energy.

The situation becomes increasingly difficult for studies of tetraquark candidates. As these states are presumably made of four quarks $|\bar{\psi}^{(f_1)}\psi^{(f_2)}\bar{\psi}^{(f_3)}\psi^{(f_4)}\rangle$ their energies are expected to lie around the two two-particle levels $|\bar{\psi}^{(f_1)}\psi^{(f_2)}\rangle + |\bar{\psi}^{(f_3)}\psi^{(f_4)}\rangle$ and $|\bar{\psi}^{(f_1)}\psi^{(f_4)}\rangle + |\bar{\psi}^{(f_3)}\psi^{(f_2)}\rangle$. Heavier tetraquarks are even more difficult to investigate. For some tetraquark candidates several lighter two-particle states might fit below the energy thresholds. All of those need to be resolved in addition to the actual tetraquark candidate, including systems with non-zero relative momentum.

Moving to a practical example, consider one of the tetraquark candidates under investigation in this thesis, the scalar $a_0(980)$. It has quantum numbers $I^G(J^{PC}) = 1^-(0^{++})$ and is described in the conventional quark antiquark interpretation by two light quarks. On the lattice however, the trial state $|\bar{d}u\rangle$ does not simply correspond to an a_0 meson, but rather excites all states of the Hamiltonian with the same quantum numbers as the a_0 . These states consist of single mesons or meson pairs, involving u , d and s quarks

$$|\bar{d}u\rangle \simeq A|a_0(980)\rangle + B|a_0(1450)\rangle + C_i|\pi\eta\rangle + D_i|\pi\eta'\rangle + E_i|K\bar{K}\rangle + \dots, \quad (3.2)$$

where we assume the $a_0(980)$ as bound state. Eventually a single correlator receives contributions from numerous states

$$\begin{aligned} C(t) &= \sum_n |\langle \bar{d}u|n\rangle|^2 e^{-E_n t} \\ &\simeq |\langle \bar{d}u|a_0(980)\rangle|^2 e^{-m_{a_0(980)} t} + \sum_{\mathbf{k}} |\langle \bar{d}u|\pi\eta\rangle_{\mathbf{k}}|^2 e^{-E(\pi(\mathbf{k}),\eta(-\mathbf{k})) t} + \dots, \end{aligned} \quad (3.3)$$

which also appear in various lattice momenta $\mathbf{k} = 2\pi \mathbf{j}/L$, e.g.

$$E(\pi(\mathbf{k}),\eta(-\mathbf{k})) = \sqrt{m_\pi^2 + \left(\frac{2\pi \mathbf{j}}{L}\right)^2} + \sqrt{m_\eta^2 + \left(\frac{2\pi \mathbf{j}}{L}\right)^2} \quad (3.4)$$

for integer \mathbf{j} .

The impact of the particular contributions is a priori not obvious, but any assignment of the observed signal from such a single correlator to a physical particle will be meaningless. The physical rest masses [29] of the relevant particles above are

$$\begin{aligned} m_{a_0(980)} &\approx 980 \text{ MeV}, \\ m_{a_0(1450)} &\approx 1474 \text{ MeV}, \\ m_\pi + m_\eta &\approx 140 \text{ MeV} + 547 \text{ MeV} = 687 \text{ MeV}, \\ m_\pi + m_{\eta'} &\approx 140 \text{ MeV} + 957 \text{ MeV} = 1097 \text{ MeV}, \\ m_K + m_{\bar{K}} &\approx 2 \times 494 \text{ MeV} = 988 \text{ MeV}. \end{aligned} \quad (3.5)$$

A method to overcome this situation and to disentangle the states that contribute to the spectrum is presented in the following section.

Additionally we want to take into account effects caused by the finiteness of our periodic lattice. These were ignored earlier by assuming to be far away from any boundary, i.e. $T \rightarrow \infty$. Given a finite lattice, two-particle states are not only described by the two particles moving together around the torus, but also by the two particles moving in opposite directions.

Not assuming an infinite lattice as in (2.44), but instead emphasizing its periodicity we include backwards propagating contributions $\{t \leftrightarrow T - t\}$ to the correlator and write

$$C(t) = \sum_{m,n} \langle m|O|n\rangle \langle n|O|m\rangle \left(e^{-E_m(T-t)} e^{-E_n t} + e^{-E_m t} e^{-E_n(T-t)} \right). \quad (3.6)$$

Again, at large temporal separations $t \gg 0$, we ideally find a correlator dominated by only one single groundstate E . Since this groundstate is now composed of two independent particles, we find for the correlator

$$C(t) \simeq |\langle 0|O|p_1 p_2\rangle|^2 \left(e^{-E t} + e^{-E(T-t)} \right) + |\langle p_1|O|p_2\rangle|^2 \left(e^{-m_1 t} e^{-m_2(T-t)} + e^{-m_1(T-t)} e^{-m_2 t} \right), \quad (3.7)$$

where $|p_1\rangle$ and $|p_2\rangle$ denote the single particle states, with $E \simeq m_1 + m_2$ at zero relative momentum. The first term describes the joint propagation of the two particles forward and backward around the torus and the second term corresponds to one particle traveling forward in time, while the other particle travels backwards in time, and vice versa.

Two particles traveling in opposite directions around the lattice either contribute by a constant or a t -dependent value to the correlation function, depending on whether they are of equal mass or not. This finite size effect is suppressed by the temporal extent of the lattice by a factor of $\approx e^{\min(m_1, m_2)T}$. For the situation of the $a_0(980)$ the potential candidates for such two particles are of considerably low masses. We hence expect contaminating contributions from such finite size effects at large temporal separations through an artificially light signal, i.e. $\approx e^{-|m_1 - m_2|t}$.

3.2 The variational method

To extract energies from our spectrum of interest we use the *variational method*. Proposed by M. Lüscher and U. Wolff [76, 77, 78] it is probably the most prominent approach to calculate hadron masses from an operator set and is applied in various projects [79, 19, 80, 7, 81]. The strategy is to use an operator set of different mesonic interpolators O_i , $i = 0, \dots, N - 1$, with the quantum numbers of the states of interest, and to compute the correlation matrix $C(t)$

$$\begin{aligned} C_{ij}(t) &= \langle O_i(t_2) O_j^\dagger(t_1) \rangle, \\ &= \sum_n \langle \Omega | O_i | n \rangle \langle n | O_j^\dagger | \Omega \rangle e^{-E_n t}. \end{aligned} \quad (3.8)$$

The set of N operators is a projection of the infinite dimensional Hilbert space to a small subspace. As such the choice of interpolators is essential for the success of the variational method and is further discussed in Section 3.3. Eigenvalues $\lambda^{(k)}$ of the generalized eigenvalue problem (GEP)

$$C(t) \mathbf{u}^{(k)}(t, t_r) = \lambda^{(k)}(t, t_r) C(t_r) \mathbf{u}^{(k)}(t, t_r), \quad (3.9)$$

do then behave as

$$\lambda^{(k)}(t, t_r) \propto e^{-E_k(t-t_r)} \left(1 + \mathcal{O}(e^{-\Delta E_k(t-t_r)}) \right), \quad (3.10)$$

where E_k is the energy of the k -th state and ΔE_k is the difference to the lowest state which is not captured by the set. Normalizing the problem at an early reference time t_r suppresses contributions from higher states and so improves the signals for small temporal separations. Zero temporal separation is not a valid option for the reference time, as the correlator is practically investigated right at the boundary, where no clear conclusions about contributing states can be made. The usual expansion is not possible at this point, which thus will be omitted from all analyses. Often this point is referred to as *contact term*. We set $t_r = a$ for all calculations.

After diagonalizing the matrix at each time t the eigenvalues must be ordered correctly. For states well separated in their energies one usually chooses an ordering by their magnitude. The situation might become more difficult for states close to one another. If statistical fluctuations do not allow for a clear separation of eigenvalues we take the eigenvector components into account as well. These are ideally time independent and an ordering according to the smallest possible change between two timeslices is performed.

Up to N states can be extracted from the exponential decays of the eigenvalues. Similar to the previous situation of only single-operator correlation functions (3.1) we utilize effective masses obtained directly from the eigenvalues, i.e.

$$a m_{\text{eff}}^{(k)}(t) = \ln \left(\frac{\lambda^{(k)}(t, t_r)}{\lambda^{(k)}(t+a, t_r)} \right), \quad (3.11)$$

to determine plateau like regions in t , which correspond to suitable fitting ranges for single exponentials. Alternatively a more precise result is obtained by solving the equation

$$\frac{\lambda^{(k)}(t, t_r)}{\lambda^{(k)}(t+a, t_r)} = \frac{\cosh \left(a m_{\text{eff}}^{(k)}(t) (t - T/2) \right)}{\cosh \left(a m_{\text{eff}}^{(k)}(t) (t + a - T/2) \right)}, \quad (3.12)$$

for $a m_{\text{eff}}^{(k)}(t)$. Here the symmetry of the correlator is taken into account as well, cf. (3.7), which leads to an improved behavior towards the center of the lattice, cf. Figure 3.1.

The eigenvector components $u_l^{(k)}$ can then be associated with the overlap of the k -th state to the l -th operator of the correlation matrix. This allows for a physical interpretation of the observed states. Rewriting the generalized eigenvalue problem as a regular eigenvalue problem

$$C(t_r)^{-\frac{1}{2}} C(t) C(t_r)^{-\frac{1}{2}} \mathbf{v}^{(k)}(t, t_r) = \lambda^{(k)}(t, t_r) \mathbf{v}^{(k)}(t, t_r), \quad (3.13)$$

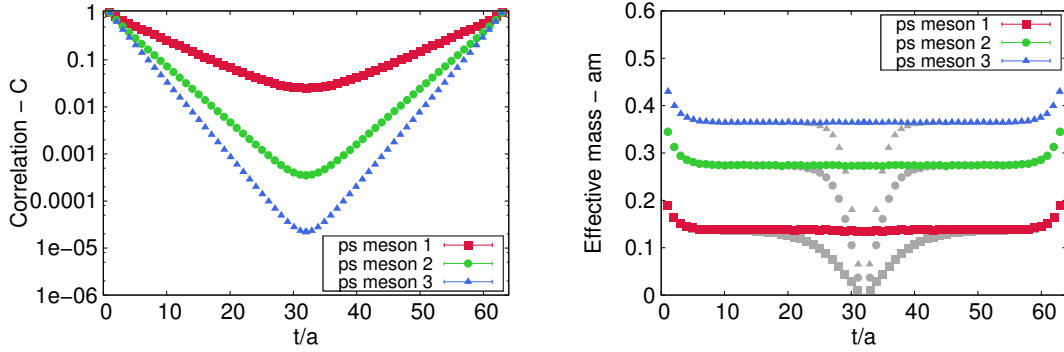


FIG. 3.1: Correlation function (left) and its associated effective mass (right) for three pseudoscalar mesons. In the right plot the gray points indicate an effective mass obtained via (3.11), while the colored points are obtained by its symmetrized alternative (3.12).

yields the same eigenvalues $\lambda^{(k)}$ but is expected to provide a smoother diagonalization process. Furthermore, from the corresponding eigenvectors $\mathbf{v}^{(k)} = C(t_r)^{\frac{1}{2}} \mathbf{u}^{(k)}$ of the symmetrical problem an orthogonal basis similar to the physical states, while $\mathbf{u}^{(k)}$ are orthogonal only in $C(t_r)$. Plotted eigenvectors in this thesis are thus always to be associated with $\mathbf{v}^{(k)}$.

This method allows for any number of interpolators as long as every element of the matrix (3.8) is calculable. While one might think that a larger operator set will always improve the analysis, realistic calculations show that this is not the case. The method is governed by its worst element and eventually a certain interpolator combination will contribute more in noise than in signal. Instead it is much better to choose an operator set that has reasonable overlap with the physical states of interest.

An alternative to solving the GEP is the Athens Model Independent Analysis Scheme (AMIAS) [82, 83, 84, 28]. This method is similar to a multi-exponential fitting tool with the major difference that the parameter space of amplitudes $A_i^{(n)} \equiv \langle \Omega | O_i | n \rangle$ and energies E_n is explored following a probability distribution function

$$P(E_n, A_i^{(n)}) = \frac{1}{Z} e^{-\chi^2/2}, \quad (3.14)$$

with appropriate normalization Z and the well-known χ^2 minimizing fits. The probability for a parameter \mathcal{A}_i to be inside $[a, b]$ is

$$\Pi(\mathcal{A}_i \in [a, b]) = \frac{\int_a^b d\mathcal{A}_i \int_{-\infty}^{+\infty} \prod_{j \neq i} d\mathcal{A}_j e^{-\chi^2/2}}{\int_{-\infty}^{+\infty} \prod_j d\mathcal{A}_j e^{-\chi^2/2}}, \quad (3.15)$$

regardless if it is an amplitude or an energy level, This multi-dimensional integral can be computed with standard Monte Carlo methods. The main advantage over the standard GEP analysis is that AMIAS does not necessarily require all elements of the correlation matrix to find the energy levels of the set, i.e. in particular problematic elements can be omitted.

3.3 Interpolating operators

To compute a certain mesonic state on the lattice we need a well-suited interpolator set for our variational approach (3.8). The interpolators are bilinear in the quark fields $\psi^{(f)}$ and excite quantum numbers determined by monomials of Dirac matrices Γ . To create states of definite spatial momenta \mathbf{p} a Fourier transformation is applied on all spatial components \mathbf{x} of the quark fields. The conventional mesonic quark-antiquark interpolator can then be written as

$$O^M = \frac{1}{\sqrt{V_s}} \sum_{\mathbf{x}} e^{-i a \mathbf{p} \mathbf{x}} \bar{\psi}_{a,\alpha}^{(f_1)}(x) \Gamma_{\alpha\beta} \psi_{a,\beta}^{(f_2)}(x). \quad (3.16)$$

Note that we do only consider a projection to zero momentum for all interpolators throughout this work and hence will often simply refer to a summation over all spatial indices for this operation. Indices f_1, f_2 denote the flavors of the quark fields (u, d, s, \dots), lower case roman letters and lower case greek letters label color and spin, respectively. For every spatial summation we do consider a normalization with the spatial volume V_s .

State	J^{PC}	Γ	Particles
scalar	0^{++}	$\mathbb{1}, \gamma_0$	f_0, a_0, \dots
pseudoscalar	0^{-+}	$\gamma_5, \gamma_0 \gamma_5$	$\pi^\pm, \pi^0, \eta, K^\pm, K^0, \dots$
vector	1^{--}	$\gamma_i, \gamma_0 \gamma_i$	$\rho^\pm, \rho^0, \omega, \dots$
axial vector	1^{+-}	$\gamma_i \gamma_5, \gamma_0 \gamma_i \gamma_5$	a_1, f_1, \dots

TAB. 3.1: Quantum numbers of the most commonly used quark-antiquark meson interpolators (3.16) and prominent particle examples. In the vector cases the sum over all polarizations $i = 1, 2, 3$ is taken.

Contracting the fermion fields of two such interpolators gives rise to quark propagators, which we are able to estimate on the lattice. These are then used to calculate the correlation functions. The possibilities for contractions of the quark fields differ noticeable according to the flavor of the fields. Of course, only creating and annihilating Grassmann variables with equal flavor can be contracted with each other

$$\langle O^M O^{M\dagger} \rangle = \frac{1}{V_s} \sum_{\mathbf{x}, \mathbf{y}} \left\langle \left(\underbrace{\bar{\psi}_{a,A}^{(f_1)}(x) \Gamma_{AB} \psi_{a,B}^{(f_2)}(x)}_{\text{solid lines}} \right) \left(\underbrace{\bar{\psi}_{a',A'}^{(f_2)}(x') (\Gamma^\dagger)_{A'B'} \psi_{a',B'}^{(f_1)}(x')}_{\text{dashed lines}} \right) \right\rangle_{F,U}. \quad (3.17)$$

For non-degenerate flavors ($f_1 \neq f_2$), e.g. an operator of the form $O^{\pi^+} = \bar{d} \gamma_5 u$, this leads to one possible combination, i.e. the solid lines in (3.17). Degenerate flavors ($f = f_1 = f_2$) within the interpolators lead to an additional possible permutation of the quark fields, which is absent in the non-degenerate case, indicated by the dashed lines. Consequently, the propagator structure of the correlator is different after contracting

the quark fields

$$\begin{aligned}
\langle O^M O^{M\dagger} \rangle &= \frac{1}{V_s} \sum_{\mathbf{x}, \mathbf{x}'} \left\langle -\Gamma_{AB} (\Gamma^\dagger)_{A'B'} \langle \psi_{a',B'}^{(f_1)}(x') \bar{\psi}_{a,A}^{(f_1)}(x) \rangle_F \langle \psi_{a,B}^{(f_2)}(x) \bar{\psi}_{a',A'}^{(f_2)}(x') \rangle_F \right. \\
&\quad \left. + \Gamma_{AB} (\Gamma^\dagger)_{A'B'} \langle \psi_{a,B}^{(f)}(x) \bar{\psi}_{a,A}^{(f)}(x) \rangle_F \langle \psi_{a',B'}^{(f)}(x') \bar{\psi}_{a',A'}^{(f)}(x') \rangle_F \right\rangle_U \\
&= \frac{1}{V_s} \sum_{\mathbf{x}, \mathbf{x}'} \left\langle -\text{tr} \left[\Gamma^\dagger \gamma_5 \left((D^{(f_1)})^{-1}(x; x') \right)^\dagger \gamma_5 \Gamma (D^{(f_2)})^{-1}(x; x') \right] \right. \\
&\quad \left. + \text{tr} \left[\Gamma (D^{(f)})^{-1}(x; x) \right] \text{tr} \left[\Gamma^\dagger (D^{(f)})^{-1}(x'; x') \right] \right\rangle_U,
\end{aligned} \tag{3.18}$$

where we made use of the γ_5 -hermiticity of the propagator $(D^{(f_{1,2})})^{-1}$ in the last line. This is a common practice to get rid of the backwards propagation and thus makes it sufficient to calculate only one set of propagators. Again with the note of caution that the latter terms on both right hand sides in (3.18) only occur for the flavor degenerate scenario.

Such correlators can be translated into diagrams where propagators are resembled by arrows pointing in the direction of propagation, cf. Figure 3.2. Here it becomes evident why these distinct contributions to a conventional quark-antiquark correlator are commonly referred to as *connected* and *disconnected* contributions.

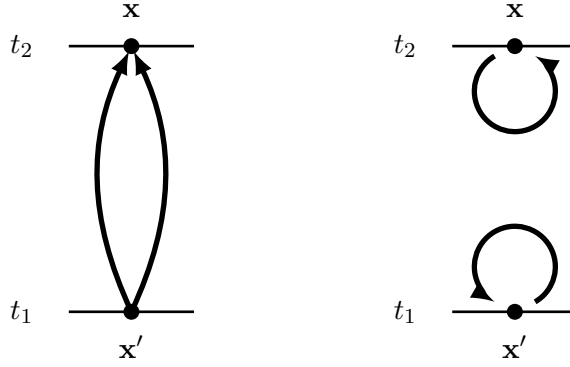


FIG. 3.2: Connected (left) and disconnected (right) contributions to a conventional quark-antiquark meson correlator. Quark propagators are represented by arrows without reference to the present color or spin structure of the diagrams, cf. (3.18).

The propagation with a starting and endpoint on a single timeslice requires an exceptional numerical effort to compute and higher statistics than their connected counterparts. For this reason such contributions were frequently neglected by many studies [85, 86, 21, 87] in the past. We will learn that the propagation within a single timeslice must not be omitted in the study of multi-particle states and in particular in the study of tetraquark candidates.

3.3.1 Four-quark interpolators

To study the $a_0(980)$ as possible tetraquark candidate, we have seen in (3.2) that a single interpolator O^{du} of the form (3.16) will ultimately not be enough to resolve the

particle spectrum of interest. Instead, we rely on an interpolator set $O_i, i = 1, \dots, N-1$, with quantum numbers $I(J^P) = 1(0^+)$. Each interpolator has to provide a good overlap with the eigenstates of the Hamiltonian that we expect in the energy regime of interest. From the resulting correlation matrix (3.8) we are able to extract the particles of interest utilizing the variational method introduced in Section 3.2.

With a proposed quark flavor content of $\{\bar{d}, u, \bar{s}, s\}$ for a tetraquark $a_0(980)$ we find a variety of possible candidates for the interpolator set. This is due to the fact that several Dirac structures of four-quark operators lead to the same set of relevant quantum numbers, e.g. $(\bar{d}\Gamma u)(\bar{s}\Gamma s)$, with $\Gamma = \gamma_5, \gamma_\mu, \gamma_\mu\gamma_5, \mathbf{1}, \dots$. However, in the following we focus on a pseudoscalar structure of quark fields within four-quark operators, i.e. a spin structure of $\Gamma = \gamma_5$. Such interpolators create the lightest mesons in a given flavor sector and are well-established from previous studies [21, 88], where also additional Dirac structures were considered.

For our studies of scalar tetraquark candidates with flavor content $\{\bar{d}, u, \bar{s}, s\}$ we consider the following operators which create states with quantum numbers $I(J^P) = 1(0^+)$, when applied to the vacuum:

$$\begin{aligned}
O^1 &= O^{q\bar{q}} &= \frac{1}{\sqrt{V_s}} \sum_{\mathbf{x}} \left(\bar{d}(\mathbf{x})u(\mathbf{x}) \right) \\
O^2 &= O^{K\bar{K}, \text{ point}} &= \frac{1}{\sqrt{V_s}} \sum_{\mathbf{x}} \left(\bar{s}(\mathbf{x})\gamma_5 u(\mathbf{x}) \right) \left(\bar{d}(\mathbf{x})\gamma_5 s(\mathbf{x}) \right) \\
O^3 &= O^{\eta_s\pi, \text{ point}} &= \frac{1}{\sqrt{V_s}} \sum_{\mathbf{x}} \left(\bar{s}(\mathbf{x})\gamma_5 s(\mathbf{x}) \right) \left(\bar{d}(\mathbf{x})\gamma_5 u(\mathbf{x}) \right) \\
O^4 &= O^{Q\bar{Q}} &= \frac{1}{\sqrt{V_s}} \sum_{\mathbf{x}} \epsilon_{abc} \left(\bar{s}_b(\mathbf{x})(C\gamma_5)\bar{d}_c^T(\mathbf{x}) \right) \epsilon_{ade} \left(u_d^T(\mathbf{x})(C\gamma_5)s_e(\mathbf{x}) \right) \\
O^5 &= O^{K\bar{K}, 2\text{part}} &= \frac{1}{V_s} \sum_{\mathbf{x}, \mathbf{y}} \left(\bar{s}(\mathbf{x})\gamma_5 u(\mathbf{x}) \right) \left(\bar{d}(\mathbf{y})\gamma_5 s(\mathbf{y}) \right) \\
O^6 &= O^{\eta_s\pi, 2\text{part}} &= \frac{1}{V_s} \sum_{\mathbf{x}, \mathbf{y}} \left(\bar{s}(\mathbf{x})\gamma_5 s(\mathbf{x}) \right) \left(\bar{d}(\mathbf{y})\gamma_5 u(\mathbf{y}) \right)
\end{aligned} \tag{3.19}$$

The different structures of the interpolators provide a reasonable overlap with the expected physical content of the spectrum. $O^{q\bar{q}}$ generates a quark-antiquark pair, the light two-quark configuration that is expected from the $a_0(980)$ as a conventional meson. All other operators in (3.19) generate two quarks and two antiquarks. $O^{K\bar{K}, \text{ point}}$ and $O^{\eta_s\pi, \text{ point}}$ are of mesonic molecule type, i.e. resemble a $K\bar{K}$ pair and a $\eta_s\pi$ pair located around the same spatial point \mathbf{x} . The η_s excites a meson-like structure composed of a pseudoscalar $s\bar{s}$ -pair, which is expected to have significant overlap to the two physical states, η and η' . $O^{Q\bar{Q}}$ combines two quarks and two antiquarks to a diquark-antidiquark pair. Due to the antisymmetric flavor combination such operators are considered to be *good diquarks*, which are lighter than their *bad* counterparts [9]. Together with a Dirac structure of $C\gamma_5$ the parity positive scalar diquark is the lightest in the spectrum [9, 89]. We also consider a diquark type operator with γ_5 replaced by $\mathbf{1}$. These four-quark operators are candidates to model the structure of a possibly existing bound four-quark state, i.e. of a tetraquark.

The remaining two operators $O^{K\bar{K}, 2\text{part}}$ and $O^{\eta_s\pi, 2\text{part}}$ are nevertheless equally essential for the study. Similar to the previous two operators they generate meson pairs ($K\bar{K}$ and $\eta_s\pi$), but this time at independent spatial points \mathbf{x} and \mathbf{y} . They are expected to have a large overlap with the low-lying two-particle states within the $I(J^P) = 1(0^+)$ sector. Only by resolving the two two-particle states we will be able to reliably identify a third low-lying state, i.e. the possible tetraquark candidate.

We emphasize the presentation of correlation matrix elements in the form of diagrams. In their spatial representation quark propagators are represented as arrows connecting lattice sites. Diagrams without a connection of the two timeslices of the interpolators do not emerge, due to the constant presence of two mass degenerate $m_u = m_d$ light quark flavors. Nevertheless, we obtain diagrams with propagators with a starting and endpoint on a single timeslice. The computation of these propagators remains numerically challenging and we thus want to distinguish between the two possible contributions to the correlator as $4\times\text{connected}$ and $2\times\text{connected}$. Note that certain elements of the correlation matrix share their spatial diagrammatic representation. Their structures in color and spin space differ from each other, but these diagrams are determined by how the interpolators distribute quarks throughout space. The correlation matrix from (3.19) represented by a spatial distribution of quark propagators is shown in Figure 3.3.

Complementary to the spatial representation of matrix elements, Figure 3.4 shows their representation in spin space. The continuous structure of the traces in spin space is illustrated by continuous dashed lines connecting the different quark spinors. Each construct of dashed lines corresponds to a single spin trace within the diagram. The specific internal spin structure in terms of Dirac matrices Γ of the operators is not illustrated, but is certainly relevant and to be inserted between the respective spinors. Together with the spatial diagrams a large amount of correlators can now be derived by “reading off” the structure from the two representations. Only the diquark-antidiquark structure remains somewhat more abstract through non-diagonal color indices. More details regarding the derivation of the matrix in spin space as well as the construction of correlators by diagrams are given in Appendix B.1.

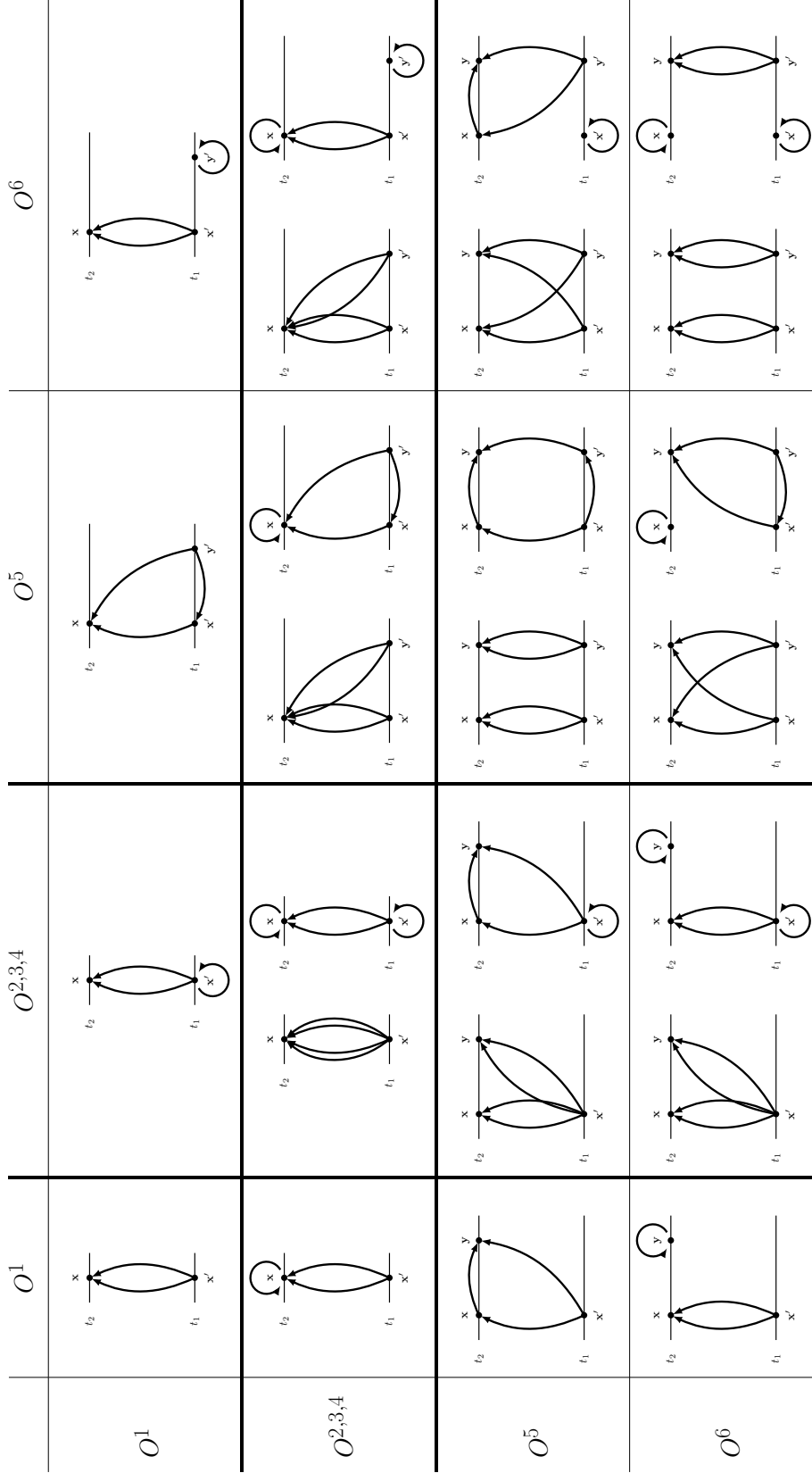


FIG. 3.3: Diagrammatic representation of the 6×6 correlation matrix from the set of interpolators (3.19) with spatial coordinates. Thick lines indicate a threefold repetition of the respective diagrams, i.e. thick lines to the left and right of an element corresponds to 1×3 submatrix and thick lines at the top and bottom of an element correspond to a 3×1 submatrix. The 3×3 submatrix is framed by thick lines.

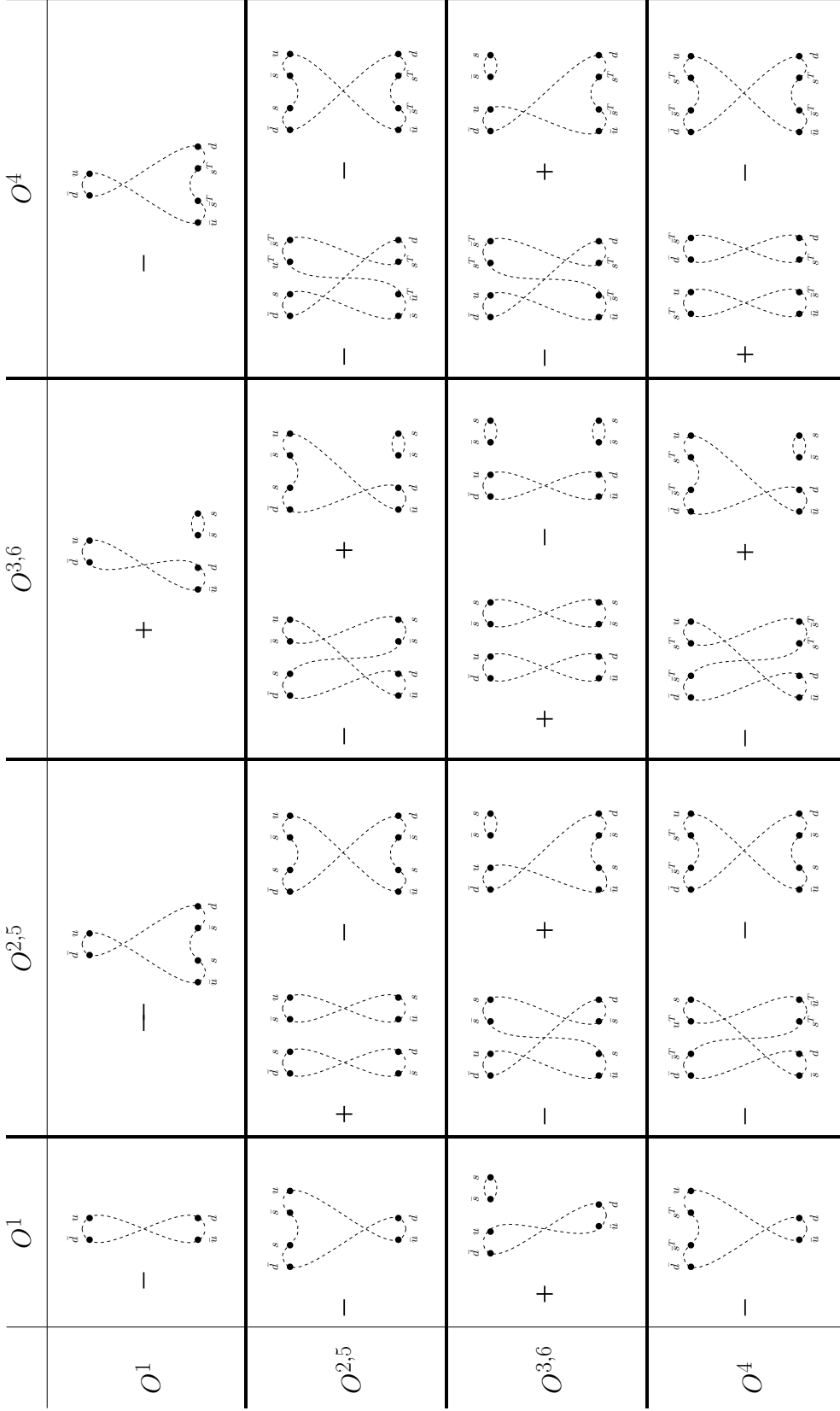


FIG. 3.4: Diagrammatic representation of the 6×6 correlation matrix from the set of interpolators (3.19) in spin space. Thick lines indicate a twofold repetition of the respective diagrams, i.e. thick lines to the left and right of an element corresponds to 1×2 submatrix and thick lines at the top and bottom of an element correspond to a 2×1 submatrix. 2×2 submatrices are framed by thick lines.

3.4 Techniques for propagator computation

To compute a correlation function (3.8) from lattice QCD we have to determine quark propagators $(D^{(f)})^{-1} = G^{(f)}$. In equation (3.18) the general structure of the correlation of two quark-antiquark interpolators is derived, which directly translates into

$$\langle O^1 O^{1\dagger} \rangle = \frac{1}{V_s} \sum_{\mathbf{x}, \mathbf{x}'} \left\langle -\text{tr} \left[\gamma_5 \left(G^d(x; x') \right)^\dagger \gamma_5 G^u(x; x') \right] \right\rangle_U, \quad (3.20)$$

for interpolator O^1 from the operator set (3.19). The Dirac structure simplifies to $\Gamma = \mathbf{1}$ and disconnected contributions do not occur. The trace is taken over color and spin indices and the γ_5 -hermiticity of the quark propagator $G^{(f)}(x; y) = \gamma_5 G^{(f)}(y; x)^\dagger \gamma_5$ is utilized to get rid of the backwards running propagation. This computational trick enables us to explicitly sum over all sites at only one of the two timeslices. This timeslice will be referred to as the *sink* (timeslice) of the correlator, in contrast to its other end, the *source* (timeslice). Technically it becomes obsolete to distinguish between the starting and end points of propagators, as these are interchangeable. Nevertheless, we denote x as the end point and y as the starting point of a propagator $G^{(f)}(x; y)$ to ease the discussion and keep in mind that we can flip the direction if needed.

In this section we discuss strategies to estimate the quark propagator, i.e. the inverse of the lattice Dirac operator (2.19). We rely on estimates as a complete inversion amounts to solving $12 \times L^3 \times T$ equations of the form

$$D_{a,A;b,B}^{(f)}(y; x) G_{b,B;c,C}^{(f)}(x; z) = \delta_{a,c} \delta_{A,C} \delta(y, z), \quad (3.21)$$

to obtain the true all-to-all propagator for a particular flavor f . Here lower case roman letters label color indices $a, b, c = 1, 2, 3$ and uppercase roman letters label spin indices $A, B, C = 1, 2, 3, 4$. Such a computation of $G^{(f)}(x; y)$ is numerically not practical at all, as its entries are expected to be highly correlated on a particular gauge field configuration and the required computer memory would be unreasonable, as shown in Section 2.4.1. Instead, it is much more practical to compute estimates of the full quark propagator, as mentioned above. These may project a certain column out of the full propagator (cf. point-to-all propagators) or attempt to estimate the full propagator under the drawback of additional stochastic noise (cf. stochastic techniques). All these estimations share the requirement to find solutions ϕ to systems of linear equations of the form

$$D_{a,A;b,B}^{(f)}(y; x) \phi_{b,B}^{(f)}(x) = \xi_{a,A}(y). \quad (3.22)$$

This numerical procedure is often referred to as an “inversion”¹. Once the source term ξ is constructed solutions are determined by iterative methods. These methods are typically so-called Krylov subspace methods. Its archetype is the conjugate gradient (CG) method [90], which solves (3.22) for matrices that are Hermitian positive definite. For our studies we initially employed the biconjugate gradient stabilized (BiCGSTAB)

¹Although a solution for ϕ is determined with certain numerical precision, D^{-1} is not known explicitly.

method [91]. However, the speed of convergence for such iterative methods can be estimated by the condition number

$$\kappa(D^{(f)}) = \left| \frac{\lambda_{\max}}{\lambda_{\min}} \right|, \quad (3.23)$$

where $\lambda_{\max/\min}$ denotes the largest and smallest eigenvalue of the matrix $D^{(f)}$, respectively. As the quark mass approaches zero the Dirac operator becomes singular, i.e. $\text{Re}(\lambda_{\min} \rightarrow 0)$, causing Krylov subspace solvers to slow down drastically. For this reason, among other issues, simulations at physical pion masses have only become feasible recently [65]. We then pursued to utilize an adaptive multigrid (MG) solver [92, 93] to solve (3.22), which further improved the computation time of our calculations by a factor of ≈ 4 . Problematic eigenmodes of the matrix are here projected onto coarser grids, which preserves the near null space of the matrix and eventually nearly removes the critical slowing down as the quark mass is taken to zero.

In the following subsections several standard techniques for propagator computation from the literature are discussed: point-to-all propagators, stochastic propagators and the one-end trick. Sequential propagators are introduced as an important procedure for the spectroscopy of multi-particle systems. To illustrate the application of these techniques correlation function (3.20) will serve as an example.

3.4.1 Point-to-all propagators

Due to spatial translational invariance of QCD it is often sufficient to compute quark propagators from a fixed spacetime point to any other point. Considering also the degrees of freedom for color and spin it requires 12 solutions of the linear system

$$D_{a,A;b,B}^{(f)}(y;x) \phi_{b,B}^{(f)}(x)[c,C,z] = \xi_{a,A}(y)[c,C,z] \quad , \quad \xi_{a,A}(y)[c,C,z] = \delta_{a,c} \delta_{A,C} \delta(y,z), \quad (3.24)$$

to obtain a column in position space of the full propagator. Each of the 12 *point sources* $\xi_{a,A}(y)[c,C,z]$ projects out a different color-spin index, labeled in cornered brackets $[c,C,z]$. Here with color index c , spin index C and z for the fixed spacetime point. These projections are then stored in the 12 solutions $\phi_{b,B}^{(f)}(x)[c,C,z]$, whereas the brackets refer to the used point source. A point-to-all propagator is then

$$\phi_{b,B}^{(f)}(x)[a,A,y] = G_{b,B;a,A}^{(f)}(x;y). \quad (3.25)$$

The example correlation function (3.20) expressed by point-to-all propagators becomes

$$C(t) = - \sum_{\mathbf{x}} \left\langle \text{tr} \left((\gamma_5)_{A,B} \left(\phi^d(\mathbf{x}, t_2)[a, B, \mathbf{x}', t_1]^\dagger \gamma_5 \phi^u(\mathbf{x}, t_2)[a, A, \mathbf{x}', t_1] \right) \right) \right\rangle_U. \quad (3.26)$$

Exploiting translational invariance allows for each correlation function to replace a single spatial sum $\sum_{\mathbf{y}}$ by a factor of V_s and fixing \mathbf{y} to an arbitrary point. Thus, correlation functions where all propagators start at the same spacetime point can be expressed exclusively in terms of point-to-all propagators. For multi-particle systems this is, however, not the case for a majority of the relevant correlation functions so that additional methods are required, cf. Figure 3.3.

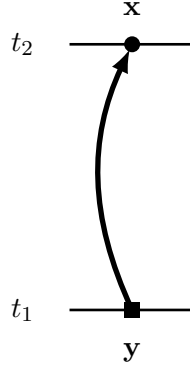


FIG. 3.5: A point-to-all propagator from a fixed point (box at $y_0 = t_1$) to every site on the lattice (circle at $x_0 = t_2$). Both ends are “open” in color and spin.

3.4.2 Stochastic timeslice-to-all propagators

While the exact computation of the full propagator remains inaccessible, stochastic techniques allow to estimate it numerically. Widely used are so-called stochastic timeslice-to-all propagators, i.e. stochastically estimated propagators from any spatial point to any other spacetime point. Defining N stochastic timeslice-sources

$$\xi_{a,A}(x)[t_0, n] = \delta(x_0, t_0) \Xi_{a,A}(\mathbf{x})[n], \quad (3.27)$$

where $\Xi_{a,A}(\mathbf{x})[n]$ are uniformly chosen random numbers satisfying

$$\frac{1}{N} \sum_{n=1}^N \Xi_{a,A}(\mathbf{x})[n]^* \Xi_{b,B}(\mathbf{y})[n] = \delta_{a,b} \delta_{A,B} \delta(\mathbf{x}, \mathbf{y}) + \text{unbiased noise}. \quad (3.28)$$

A common choice is $\Xi_{a,A}(\mathbf{x})[n] \in \mathbb{Z}(2) \times \mathbb{Z}(2)$ which results in an unbiased noise proportional to $\mathcal{O}(1/\sqrt{N})$. As usual, since the noise average and the average over the gauge field commute, in practice one can take a fairly small number N of noise sources per gauge configuration, but not smaller than the number of propagators in the diagram. The linear system (3.22) takes the form

$$D_{a,A;b,B}^{(f)}(y; x) \phi_{b,B}^{(f)}(x)[t_0, n] = \xi_{a,A}(y)[t_0, n], \quad (3.29)$$

allowing an estimation of the propagator as

$$\begin{aligned} \frac{1}{N} \sum_{n=1}^N \phi_{b,B}^{(f)}(x)[t_0, n] (\xi_{c,C}(y)[t_0, n])^\dagger \\ = G_{b,B;a,A}^{(f)}(x; z) \frac{1}{N} \sum_{n=1}^N \xi_{a,A}(z)[t_0, n] (\xi_{c,C}(y)[t_0, n])^\dagger \\ = G_{b,B;c,C}^{(f)}(x; y) + \sum_{b,B,z} G_{b,B;a,A}^{(f)}(x; z) \times \underbrace{\mathcal{O}(N^{-\alpha})}_{\text{off-diagonal noise}}, \end{aligned} \quad (3.30)$$

where we applied (3.28) and expect an $\alpha \sim 1/2$ for the applied distribution of $\Xi_{a,A}(x)[n] \in \{(\pm 1 \pm i)/\sqrt{2}\}$. The example correlation function (3.20) expressed by stochastic timeslice-to-all propagators becomes

$$C(t) = -\frac{1}{N(N-1)} \sum_{n \neq n'} \frac{1}{V_s} \left\langle \left(\sum_{\mathbf{x}} \phi^d(\mathbf{x}, t_2)[t_1, n']^\dagger \gamma_5 \phi^u(\mathbf{x}, t_2)[t_1, n] \right) \left(\sum_{\mathbf{x}'} \xi(\mathbf{x}', t_1)[t_1, n]^\dagger \gamma_5 \xi(\mathbf{x}', t_1)[t_1, n'] \right) \right\rangle_U. \quad (3.31)$$

Note that each propagator needs to be estimated by different stochastic sources $\xi[n]$ and the corresponding solutions $\phi[n]$ (guaranteed by $\sum_{n \neq n'}$).

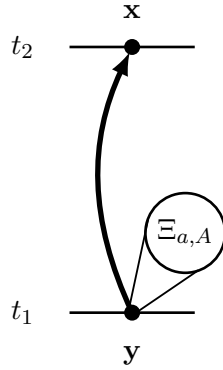


FIG. 3.6: Stochastic timeslice-to-all propagator from a fixed timeslice (circle at $y_0 = t_1$; including stochastic noise) to any point on the lattice (circle at $x_0 = t_2$). Both ends are “open” in color and spin.

Similar to point-to-all propagators stochastic propagators are described by both source and solution. In the former case the point sources do not explicitly appear in the construction of the propagator (3.25), but are implicitly taken into account by considering the color-spin structure of the correlation function, cf. (3.26). The latter propagators are explicitly build by the solutions of the linear systems in combination with their corresponding stochastic sources, cf. (3.30). Hence, point-to-all propagators and stochastic propagators provide great flexibility for all possible color-spin structures at source and sink of the correlator.

A severe drawback of stochastic propagators is that they introduce additional stochastic noise. The number of off-diagonal noise terms is $\approx V_s^{2M}$ multiplied with the number of signal terms, where M is the number of the stochastic timeslice-to-all propagators used. While using a single stochastic propagator, i.e. $M = 1$, typically leads to acceptable signal-to-noise ratios, the noise grows quite rapidly with the number of stochastic propagators. Already for $M > 2$, the signal can easily be lost in stochastic noise if these techniques are applied naïvely. We therefore avoid applying stochastic propagators as an estimate, whenever another technique presented in this section can be applied instead.

Nevertheless, this particular technique is crucial to our studies. Through the operator set (3.19) we inevitably require propagators with a starting and endpoint on a single timeslice, and, more precisely, create and annihilate quarks on all sites, i.e. small loops

$G^s(x; x)$ at every x . In general such a propagator can be estimated for a single site by a point-to-all propagator, truncated to propagate only to its origin. The situation becomes a lot more complicated if for any reason one can not omit the spatial sum $\sum_{\mathbf{x}}$ related to the arguments of the propagator, i.e. if x_0 happens to be the sink-timeslice, cf. Appendix B.2. In all these scenarios we estimate the fermion loops by truncating stochastic timeslice-to-all propagators to their source timeslices. These timeslice-to-timeslice propagators are then computed on $N_{\Delta t}$ consecutive timeslices to allow the measurement of the correlation function for in total $N_{\Delta t}$ temporal separations.

3.4.3 The one-end trick

The one-end trick is a technique to estimate the product of two propagators stochastically. While this might seem as an disadvantage at first glance, the one-end trick turns out to excel in efficiency to the prior introduced techniques. The product is of the form

$$\sum_{\mathbf{y}} G^{(f_1)}(x; \mathbf{y}, t) \Gamma G^{(f_2)}(\mathbf{y}, t; z), \quad (3.32)$$

i.e. the propagators are connected at every spacetime point (\mathbf{y}, t) , but no further propagators start or end at (\mathbf{y}, t) . With this condition the one-end trick is particularly suited to compute correlation functions where at least one interpolating operator is either a conventional meson or a two-meson creation operator, i.e. $\bar{\psi}^{(f_1)}\psi^{(f_2)}$ or $(\bar{\psi}^{(f_1)}\psi^{(f_2)})_{\mathbf{x}} (\bar{\psi}^{(f_3)}\psi^{(f_4)})_{\mathbf{y}}$.

The linear systems to be solved take the form

$$D_{a,A;b,B}^{(f_1)}(y; x) \phi_{b,B}^{(f_1)}(x)[t_0, n] = \xi_{a,A}(y)[t_0, n], \quad (3.33)$$

$$D_{a,A;b,B}^{(f_2)}(y; x) \tilde{\phi}_{b,B}^{(f_2)}(x)[t_0, \Gamma, n] = (\gamma_5 \Gamma^\dagger \xi)_{a,A}(y)[t_0, n], \quad (3.34)$$

where ξ is a stochastic timeslice source defined in (3.27). The resulting ϕ and $\tilde{\phi}$ estimate the product of propagators as

$$\sum_{\mathbf{y}} G^{(f_1)}(x; \mathbf{y}, t) \Gamma G^{(f_2)}(\mathbf{y}, t; z) = \frac{1}{N} \sum_{n=1}^N \phi^{(f_1)}(x)[t, n] \tilde{\phi}^{(f_2)}(z)[t, \Gamma, n]^\dagger \gamma_5 + \text{unbiased noise}. \quad (3.35)$$

Both γ_5 in (3.34) and (3.35) arise as a consequence of utilizing γ_5 -hermiticity on one of the two propagators in (3.32). Applying the one-end trick to the example correlation function (3.20) yields

$$C(t) = -\frac{1}{N} \sum_{n=1}^N \frac{1}{V_s} \left\langle \sum_{\mathbf{x}} \tilde{\phi}^d(\mathbf{x}, t_2)[t_1, \mathbf{1}, n]^\dagger \gamma_5 \phi^u(\mathbf{x}, t_2)[t_1, n] \right\rangle_U. \quad (3.36)$$

The advantage of the one-end trick in comparison to naïve stochastic propagators comes with the shared stochastic source terms. The stochastic noise introduced by the signal terms is only accompanied by a single noise term, introduced by this source setup. For the example at hand (3.20) we count two signal terms with a single source term for the one-end trick (3.36) and two source terms for stochastic timeslice-to-all propagators

(3.31). Effectively leaving us with $\propto V_s^3$ compared to $\propto V_s^4$ stochastic noise terms for the two methods, respectively.

The main disadvantage of the one-end trick is introduced by the shared source terms as well. Emphasized by the Γ in (3.34) we find that the spin structure is fixed at the source. While this might not be an issue for relatively small interpolator bases, it will become impractical for larger ones. To circumvent this situation spin indices at the source can be installed explicitly by *spin dilution*. The introduced procedure remains the same, but stochastic sources are modified according to

$$\xi_{a,A}(y)[t_0, n] \longrightarrow \xi_{a,A}(y)[t_0, B, n] = \delta(y_0, t_0) \delta_{A,B} \Xi_{a,B}(y)[n]. \quad (3.37)$$

The inversion for a particular Γ is afterwards redundant, but the total amount required inversions becomes four, one for each spin index. The solutions of the linear system are then applied similar to point-to-all propagators, i.e.

$$C(t) = -\frac{1}{N} \sum_{n=1}^N \frac{1}{V_s} \left\langle \sum_{\mathbf{x}} (\gamma_5)_{A;B} \left(\phi^d(\mathbf{x}, t_2)[t_1, B, n]^\dagger \gamma_5 \phi^u(\mathbf{x}, t_2)[t_1, A, n] \right) \right\rangle_U. \quad (3.38)$$

Spin dilution does not further improve the signal-to-noise ratio of the calculated two-point function. Determining factor is still the total number of inversions performed, i.e. $4N$ with or N without dilution.

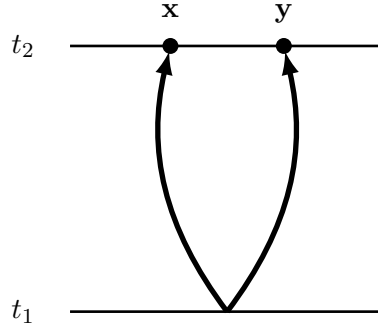


FIG. 3.7: The one-end trick applied to a product of quark propagators, resulting in two signal terms $\phi(x), \tilde{\phi}(y)$ to all lattice sites. These are inseparably connected at t_1 to a fixed color and spin structure, hence the missing symbol.

3.4.4 Sequential propagators

In contrast to the previous subsections sequential propagators do not label a technique to efficiently estimate a quark propagator, or a product of such. Instead, sequential propagators label a procedure to solve linear systems successive, in order to allow the estimation of a propagator product as a single propagator. The only condition for the procedure itself is identical to the one for the one-end trick (3.32)

$$\sum_{\mathbf{y}} G^{(f_1)}(x; \mathbf{y}, y_0) \Gamma G^{(f_2)}(\mathbf{y}, y_0; z) = G^{(f_1; f_2)}(x, z)[\Gamma], \quad (3.39)$$

i.e. no other propagator shares spacetime point y . Any other constraints come from whatever technique is applied to estimate $G^{(f_1;f_2)}[\Gamma]$, e.g. breaking of translational symmetry for sequential point-to-all propagators, or the presence of a suited third propagator $G^{(f_3)}(z, w)$ to combine sequential propagation with the one-end trick. As the techniques for propagator estimation were discussed in the previous subsections, we focus on the procedure of solving linear systems to estimate $G^{(f_1;f_2)}[\Gamma]$ below. This procedure may then replace the respective linear system of the technique, as soon as the structure (3.39) is identified. While there are in principle no limitations to the timeslices x_0 , y_0 and z_0 , we will focus on two cases.

For $x_0 \neq y_0 = z_0$ flavor (f_2) in (3.39) will propagate within timeslice z_0 , i.e. the timeslice of the source term ξ . The linear system taking the shape

$$D_{a,A;b,B}^{(f_2)}(x; y) \phi_{b,B}^{(f_2)}(y)[z_0, \cdot] = \xi_{a,A}(x)[z_0, \cdot], \quad (3.40)$$

where the open indices $[\cdot]$ reflect the freedom to apply any of the prior discussed techniques. Note, that this also implies the particular features of the techniques, e.g. color and spin dilution $[a, A]$ for point-to-all propagators. In a subsequent linear system the just obtained solution $\phi^{(f_2)}$ serves as a source term

$$D_{a,A;b,B}^{(f_1)}(y; x) \psi_{b,B}^{(f_1;f_2)}(x)[z_0, \Gamma; \cdot] = (\Gamma \phi)_{a,A}^{(f_2)}(y)[z_0, \cdot] \delta(y_0, z_0). \quad (3.41)$$

Notice the timeslice dilution of $\phi^{(f_2)}$ to ensure the propagation only within $y_0 = z_0$, as well as the need to insert the spin structure Γ at this joint element. Then

$$\begin{aligned} \left(\sum_{\mathbf{y}} G^{(f_1)}(x; \mathbf{y}, y_0) \Gamma G^{(f_2)}(\mathbf{y}, y_0; z) \right)_{a,A;b,B} &= \left(G^{(f_1;f_2)}(x, z)[\Gamma], \right)_{a,A;b,B} \\ &= \psi_{a,A}^{(f_1;f_2)}(x)[z_0, \Gamma; \cdot]. \end{aligned} \quad (3.42)$$

For $x_0 = y_0 \neq z_0$ flavor (f_1) will propagate within timeslice x_0 and the steps are essentially analogous to the previous situation, except for the limitation of propagation within timeslices. $(\Gamma \phi)^{(f_2)}$ is diluted with $\delta(y_0, z_0)$, as before, and additionally is the solution of the second linear system modified according to

$$\psi^{(f_1;f_2)}(x)[z_0, \Gamma; \cdot] \rightarrow \psi^{(f_1;f_2)}(x)[z_0, \Gamma; \cdot] \delta(x_0, y_0). \quad (3.43)$$

In order to achieve an appropriate temporal separation for the correlation function $C(\Delta t)$ (here $\Delta t = |x_0 - z_0|$) it is thus required to repeat the procedure $N_{\Delta t}$ times, i.e. for $N_{\Delta t}$ consecutive timeslices $x_0 = y_0$ to a fixed source timeslice z_0 . Appendix B.3 provides a simple example for the application of sequential propagators in the practical context of matrix element C_{15} .

It can be quickly understood that the procedure is more efficient if the timeslice propagation is placed into the source timeslice, both due to fewer required inversions and by covering the whole temporal lattice extent. In the end, however, it is necessary to implement both, in order to compute the full correlation matrix.

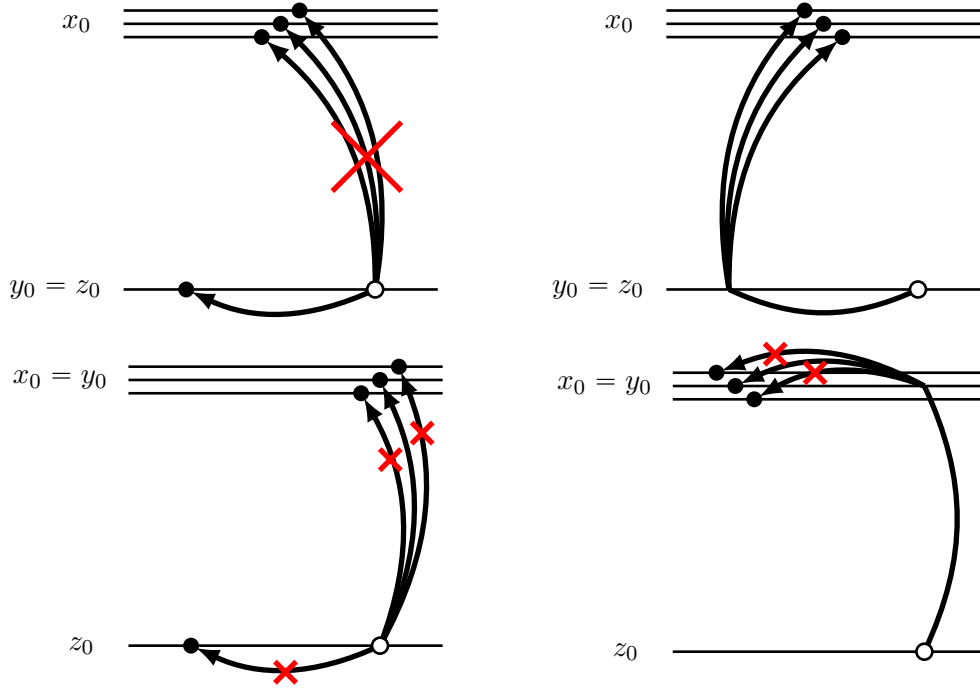


FIG. 3.8: Procedure to estimate sequential quark propagators with propagation within source (upper row) and sink (lower row) timeslices. The white dots mark one end of the joint propagator $G^{(f_1:f_2)}[\Gamma]$ on the source timeslice. Red crosses represent the requirement for δ -functions to limit the propagation after solving the first (left column) and second (right column) stage of linear systems. Neighboring timeslices to the sink are shown to emphasize the gain by placing the timeslice propagation into the source timeslice, as well as the importance of limiting the propagation for the sink scenario. Notice how the lower procedure only yields a single temporal separation $\Delta t = |x_0 - z_0|$.

3.5 Smearing Techniques

To obtain the best possible signal-to-noise ratio for the measured correlators, the operator set is required to have a large overlap with the expected physical states. The operators introduced in (3.19) are designed to model the quark, color and spin structure but they are also local, i.e. all quark pairs share the same lattice site. To improve the overlap to the physical states we hence consider *smear*ed gauge and fermion fields for our operators. By replacing the fields through local averages we create spatially extended trial states that provide a significantly improved overlap to the present low energy eigenstates.

3.5.1 Gauge link smearing

To smear out the fermion fields in the spatial directions of the lattice we require link variables to preserve gauge invariance. Similarly to the fermion fields we also smear the link variables involved. The signal of the correlator is then further enhanced by

smoothing short distance fluctuations of the gauge field. We employ APE smeared [94, 95] spatial link variables $U_i^{(N_{\text{APE}})}$ by iteratively replacing the links according to

$$\tilde{U}_i^{(n)}(x) = U_i^{(n-1)}(x) + \alpha \sum_{i \neq j} \Pi_{ij}^{(n-1)}(x), \quad (3.44)$$

where $U^{(0)}$ are the unsmeared links and Π are the four perpendicular forward and backward staples

$$\begin{aligned} \Pi_{ij}^{(n)}(x) = & U_j^{(n)}(x) U_i^{(n)}(x + \hat{j}) U_j^{(n)}(x + \hat{i})^\dagger \\ & + U_j^{(n)}(x - \hat{j})^\dagger U_i^{(n)}(x - \hat{j}) U_j^{(n)}(x + \hat{i} - \hat{j}). \end{aligned} \quad (3.45)$$

The averages of link variables $\tilde{U}^{(n)}$ are, however, not group elements of $SU(3)$ and hence usually projected back to a $SU(3)$ matrix. This is realized by maximizing $\text{Re tr} \left[X^{(n)} \tilde{U}_i^{(n)\dagger} \right]$ for an $X \in SU(3)$. The so determined group element can then serve as the next iteration of link variables, i.e.

$$U_i^{(n)}(x) = P_{SU(3)} \left(\tilde{U}_i^{(n)}(x) \right). \quad (3.46)$$

For the present calculations we employed a weighting of $\alpha_{\text{APE}} = 0.45$ and performed $N_{\text{APE}} = 20$ iteration steps. APE smeared gauge fields are only used to smear sources and solutions of the linear systems (3.22) of each technique. For the linear systems themselves the unsmeared gauge field is applied to preserve fluctuations as well as the coupling strength.

3.5.2 Smeared quark sources and sinks

Fermion fields of local operators are spatially extended by Gaussian smearing [96, 97]. Such smeared fields are a common practice in lattice QCD as they minimize contributions of excited states to the ground state. The smeared fermion field $\psi^{(N_{\text{Gauss}})}$ is obtained after iteratively distributing the field to neighboring sites, i.e.

$$\psi^{(n)}(x) = \frac{1}{1 + 6\kappa_{\text{Gauss}}} \left(\psi^{(n-1)}(x) + \kappa_{\text{Gauss}} \sum_{\pm i} U_i^{(N_{\text{APE}})}(x) \psi^{(n-1)}(x + \hat{i}) \right), \quad (3.47)$$

where $\psi^{(0)}$ is the unsmeared quark operator and $U^{(N_{\text{APE}})}$ labels the gauge field with APE smeared spatial links, cf. the previous subsection. The free parameters κ_{Gauss} and N_{Gauss} are chosen to adjust the width of the quark field to an approximately Gaussian shape. For our calculations we used $\kappa_{\text{Gauss}} = 0.5$ and $N_{\text{Gauss}} = 50$. The width of the smeared quark fields can then be estimated [98] by $\sigma \approx \sqrt{2\kappa_{\text{Gauss}} N_{\text{Gauss}} / (1 + 6\kappa_{\text{Gauss}})} a \approx 0.3 \text{ fm}$. Implementing extended operators in principle implies that every linear system considered to estimate a quark propagation (introduced in Section 3.4) needs to be surrounded by operations that smear the source terms ξ beforehand and the solutions ϕ afterwards. This applies also for the procedure of sequential propagation. After the first solution (3.40) is obtained it needs to be smeared twice as it is both solution and source to a linear system. For stochastic timeslice-to-all propagators, cf. Section 3.4.2, the sources are explicitly in use. Hence, it is advisable to smear both, source and sink, *after* solving the corresponding linear system.

4

TECHNICAL ASPECTS

Before we analyze the results of our lattice computations, we discuss the technical aspects of our study in this chapter. Although a lot of the information has been already given throughout this thesis, Section 4.1 summarizes the simulation details in a compact style, providing a quick overview of the input parameters to our calculations. Since we aim to study a tetraquark candidate of a flavor that is not contained in the gauge field simulations we need to fix a valence charm quark mass so that states on the lattice coincide with physical states. Section 4.2 is the central piece of this chapter and discusses various methods to compute every diagram of the correlation matrix in the most efficient way. As the diagram structures become more sophisticated it is no longer obvious which techniques or combination of techniques yield the smallest relative error at comparable computational costs. The efficiency is not sensitive to the spin structure of the interpolators and hence results shown are of great value for various projects involving multi-quark operators. Results presented in this section are also to be found in [27]. In Section 4.3 the $2\times$ connected diagrams occurring in four-quark flavor structures of the form $\{\bar{\psi}^{(f_1)}\psi^{(f_2)}\bar{\psi}^{(f_3)}\psi^{(f_3)}\}$ are examined in more detail. We are especially interested in the impact of these diagrams to the overall studies and will show that their contribution is essential.

4.1 Simulation details

All numerical investigations presented in this thesis are based on gauge link configurations generated by the PACS-CS collaboration [65]. The gluonic action is the Iwasaki gauge action [42, 43] and the quark action for $N_f = 2 + 1$ is a non-perturbatively $\mathcal{O}(a)$ -improved Wilson-clover fermion action [55, 56].

We consider a single ensemble with gauge coupling $\beta = 1.9$, corresponding to a lattice spacing of $a \approx 0.091$ fm and a pion mass of $m_\pi \approx 300$ MeV. Further details of the gauge field ensemble are listed in table 4.1.

β	$(L/a)^3 \times T/a$	$\kappa_{u,d}$	κ_s	c_{SW}	a [fm]	m_π [MeV]	N_{conf}
1.90	$32^3 \times 64$	0.1377	0.1364	1.715	0.091	300	500

TAB. 4.1: PACS-CS gauge link ensemble in use (cf. also [65]).

To enhance the groundstate overlap of trial states $O^i|0\rangle$ generated by our interpolating field operators 3.19 we apply standard smearing techniques, cf. Section 3.5. For the quark field operators $\psi^{(f)}, \bar{\psi}^{(f)}$ we use Gaussian smearing with APE smeared spatial links, with parameters $N_{\text{Gauss}} = 50$, $\kappa_{\text{Gauss}} = 0.5$, $N_{\text{APE}} = 20$ and $\alpha_{\text{APE}} = 0.45$.

For every measurement the source timeslices is chosen randomly. Every point-to-all propagator is computed on a single set of 12 inversions, corresponding to a set of 12 point sources at the same randomly chosen point in space. Each stochastic timeslice-to-all propagator is estimated by 15 independently chosen stochastic source terms, i.e. $N_{\text{sto}} \equiv N = 15$ in (3.30). Each one-end trick, which provides a much better signal to noise ratio than simple stochastic propagators, is computed for three independently chosen stochastic sources, i.e. $N_{\text{one}} \equiv N = 3$ in (3.35). Moreover, whenever the application of a method is restricted to a single temporal separation we perform $N_{\Delta t} = 15$ inversions for consecutive sink timeslices. This results in a range of $0 \leq t/a \leq 14$ for the $2\times$ connected pieces of the respective correlation functions, which are typical temporal separations where a signal is expected. Whenever possible we average correlation functions in positive and negative time direction and determine the errors by a standard jackknife procedure.

In total we discuss two simulation runs. One for a $\{\bar{d}, u, \bar{s}, s\}$ flavor setup to investigate the properties of the light tetraquark candidate $a_0(980)$ and a second run for the flavors setup $\{\bar{c}, s, \bar{u}, u\}$ to investigate the heavy tetraquark candidate $D_{s_0}^*(2317)$. The simulation parameters do not change between the two runs, but they differ in the number of total measurements taken into account. For the light tetraquark candidate we perform seven independent measurements on each gauge configuration, while only four independent measurements are computed on each gauge configuration for the investigation of the heavy candidate.

4.1.1 Fixing a charm quark mass

We consider a partially quenched setup to obtain quantitative insights on the tetraquark candidate $D_{s_0}^*(2317)$. The charm quark mass is determined by tuning the hopping parameter κ to coincide with pseudoscalar open-charm mesons. In particular the D and D_s states are of great relevance, as they will determine the neighboring infinite volume two-particle levels. The results for several independent simulation runs are shown in Figure 4.1. Colorized straight lines indicate pseudoscalar energy levels in MeV [29] that we aim to reproduce on the lattice. With respect to the unphysically heavy light quark mass of our ensemble we determine

$$m_D^{\text{lat.}}(\kappa_{u,d}, \kappa_c) \approx m_D^{\text{phys.}} \quad \text{and} \quad m_{D_s}^{\text{lat.}}(\kappa_s, \kappa_c) \approx m_{D_s}^{\text{phys.}}, \quad (4.1)$$

which is given for a $\kappa_c = 0.1237$. At this value pseudoscalar states from the lattice coincide with the physical D and D_s mesons, as it can be seen on the right of Figure 4.1. Due to relatively heavy light quark the η_c meson is tuned to a lighter mass than in nature, but is of no further concern for our studies with a valence charm quark.

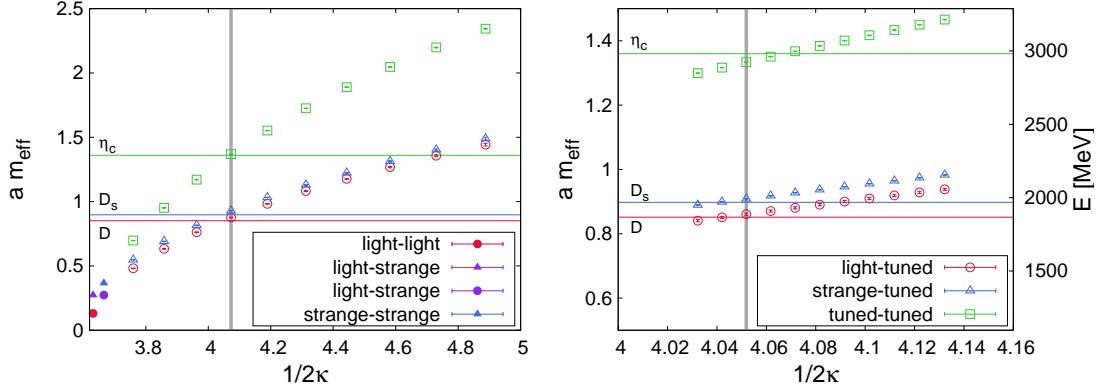


FIG. 4.1: Partially quenched two-step tuning of a quark mass to a charm quark. Pseudo-scalar mesonic states as function of $1/2\kappa$. A first simulation run with in κ (left) and a second run with a narrow range (right) are shown. Vertical gray lines emphasize relevant κ values. Closed symbols refer to states from quarks existing in the ensemble, open symbols contain a tuned quark mass. Circle, triangle and square symbols contain at least one light, strange and tuned quark, respectively. Straight horizontal lines correspond to the energies of charmed mesons in MeV [29].

4.2 Computation of the correlation matrix

The techniques introduced in Chapter 3 allow the computation of the whole correlation matrix (3.8) resulting from the selected operator set (3.19), cf. Figure 3.3. It is important to note that one relies on *all* of the introduced techniques, as several diagrams are inaccessible for one technique alone. In this section we discuss and compare promising strategies to compute two-point correlation functions of two- and four-quark interpolating operators of different structures. An efficient method satisfies the following three criteria,

- (A) requires only a small number of inversions
- (B) averages the diagram over space
- (C) introduces no or only a moderate number of stochastic noise terms

In practice ideal methods do not exist. In particular the criteria (B) and (C) exclude each other. Stochastic noise is only avoided by fixed point sources, which in return do not average the correlation function over space on one of the two timeslices. In the following subsections every diagram type appearing in the correlation matrix is analyzed with respect to its efficiency. To compare two methods in a quantitative way we employ a quality ratio

$$R^{(a),(b)}(t) = \frac{\Delta C^{(a)}(t) \cdot \sqrt{\tau^{(a)}}}{\Delta C^{(b)}(t) \cdot \sqrt{\tau^{(b)}}}, \quad (4.2)$$

where $\Delta C^{(x)}(t)$ denotes the statistical error of the correlation function at temporal separation t and $\tau^{(x)}$ is the required computing time to obtain every propagator for method (x) , respectively. A ratio $R^{(a),(b)}(t) < 1$ hence indicates that method (b) is inferior to method (a) , i.e. that the obtained statistical error of (a) is smaller at comparable computational cost. In the following the investigated methods are labeled alphabetically and arranged according to decreasing efficiency. Hence (a) is superior to (b) , etc. By comparing all methods exclusively to (a) it is convenient to use the notation $R^{(b)}(t) \equiv R^{(a),(b)}(t)$.

The computational effort estimated by $\tau^{(x)}$ is determined by the number of inversions required to realize method (x) . Throughout each evaluation of a single gauge field configuration we employed the same set of input parameters for the inversions to be performed, cf. Section 4.1. The resulting quality ratios $R^{(x)}$ are by its construction only weakly dependent on the number of stochastic source terms. Improvements in terms of smaller statistical errors $\Delta C^{(x)}$ are compensated with an increase in the associated computational effort $\tau^{(x)}$.

Results shown in the following subsections belong to a computation of the flavor setup $\{\bar{d}, u, \bar{s}, s\}$. For this scenario a large number of inversions is always performed on the relatively heavy strange quark mass, which again leaves the quality ratios $R^{(x)}$ weakly dependent on variations of the computed temporal range. In the flavor setup $\{\bar{c}, s, \bar{u}, u\}$ this large number of inversions is required for the light quark mass. The majority of results shown are qualitatively in agreement for both flavor setups. At the end of this section we discuss the similarities and differences between the two flavor setups by selected examples. If not stated otherwise results shown refer to computations of the flavor setup $\{\bar{d}, u, \bar{s}, s\}$.

For every method we discuss the spatial appearance of the diagram type is printed once. Quark propagators are again represented by arrows and color differently for each method, to indicate different combinations of techniques used to compute the overall diagram. Point-to-all propagators are colored in blue, stochastic timeslice-to-all propagators in red and two propagators estimated by the one-end trick are colored in green, cf. Section 3.4. Sequential propagators were introduced rather as a procedure than as an independent technique and, hence, are not emphasized by a distinct color code. They are applied whenever a propagator is restricted to a single timeslice connecting two independent spatial sites (not to be confused with loops). Sequential propagators are colored according to the technique they are applied to. Fixed point sources are represented by black boxes, while stochastic timeslice sources and the solutions of the linear systems are represented by black circles. Spatial sums that are calculated explicitly or implicitly are further emphasized by a sum and a double headed arrow ($\Sigma \longleftrightarrow$), colored in black or gray, respectively. Implicit summations occur while either employing the one-end trick or sequential propagators, cf. Figure 4.2. The sink-timeslice is either characterized by at least one explicit summation, and/or the timeslice which has at least two arrowheads pointing towards it.

In addition to the colored diagrams Appendix B.4 presents a table for each diagram type studied. Therein the minimal amount of required inversions to realize the respective methods is given for each quark flavor. In combination with the colored diagrams this provides a detailed exposure of the computation of every matrix element.

We do not compare all possible methods, but focus on the ones that are promising

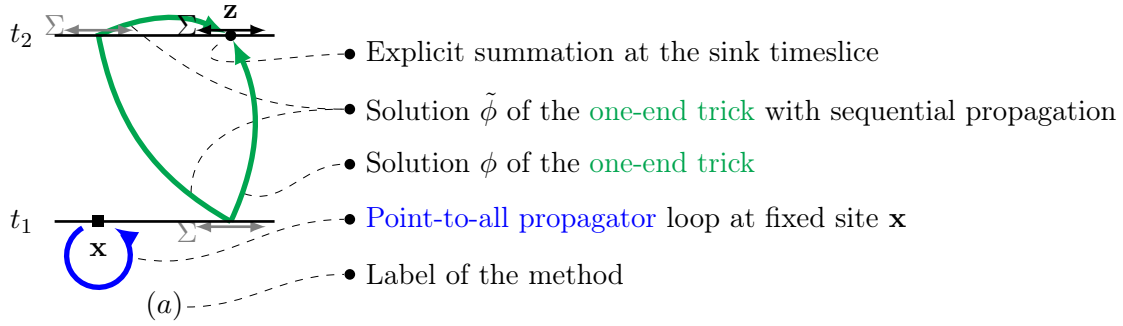


FIG. 4.2: Color scheme illustrated by the example of one method for the diagrammatic representation of $C_{56}^{(2 \times \text{connected})}$.

a priori. In particular, we do not consider methods making excessive use of stochastic timeslice-to-all propagators. These are in principle applicable at every instance, but introduce a large number of stochastic noise terms. The maximum number of stochastic techniques we want to employ is either a stochastic timeslice-to-all propagator in combination with the one-end trick, or twice the one-end trick. Moreover, whenever possible, techniques for propagator computation are combined in such a way that multiple inversions for consecutive sink timeslices are not necessary. Especially sequential point-to-all propagators which involve a propagation within the sink timeslice are incredibly inefficient, due to the large amount of necessary inversions of the various color and spin configurations.

4.2.1 Two-quark – two-quark

The numerical implementation of this diagram type has been extensively discussed in Section 3.4. Here, we consider two methods as promising. The one-end trick, which averages the diagram over space at both timeslices t_1 and t_2 , but introduces stochastic noise terms, and point-to-all propagators, which fix one side of the correlator, but introduce no additional stochastic noise.

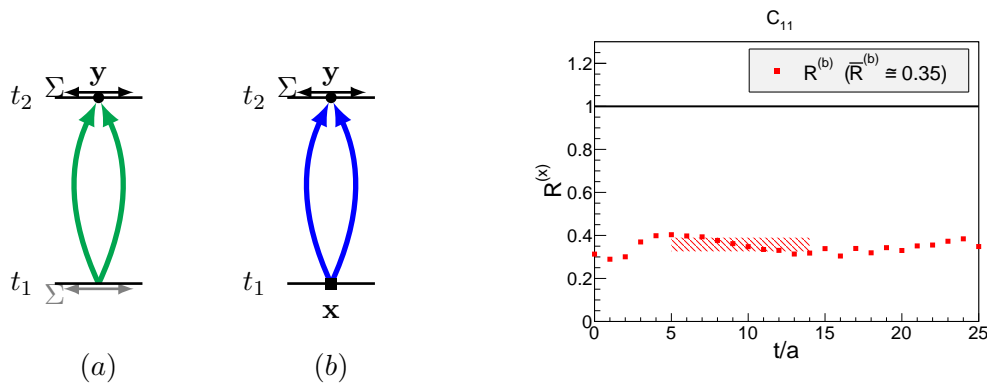


FIG. 4.3: Efficiency of different methods for C_{11} .

A numerical comparison for our lattice setup [65] shows the clear superiority of the one-end trick at early and late times at comparable numerical effort. An average quality ratio $\bar{R}^{(b)} \simeq 0.35$ is taken in a range of $5 \leq t/a \leq 14$, which corresponds to a typical region to extract energy levels.

4.2.2 Two-quark – four-quark

This particular correlation is represented by only a single diagram type, which however applies for three matrix elements in Figure 3.3. The quality ratios shown in Figure 4.4 for all three diagrams C_{12} , C_{13} and C_{14} show that method (a), which does not introduce any stochastic noise terms, is clearly more efficient.

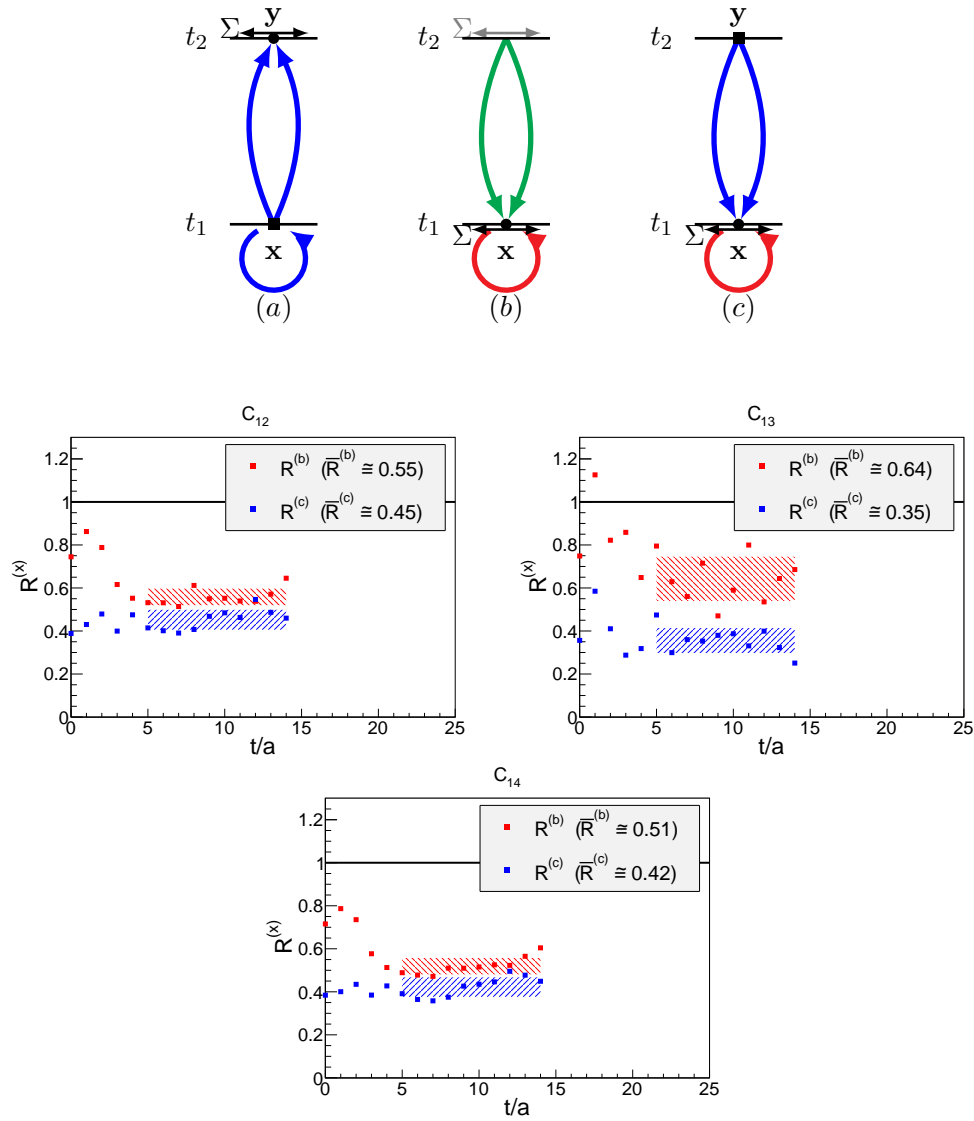


FIG. 4.4: Efficiency of different methods for C_{12} , C_{13} and C_{14} .

What does not become evident from the quality ratios is, that method (a) also provides temporal separations for the whole lattice extent T , while method (b) and (c) are restricted to a predefined range. More severe statistical fluctuations are observed for the C_{13} element. This is caused by the loop propagator, which in this scenario is found in an isolated trace with respect to the rest of the correlator, cf. Figure 3.4. Consequently, we try omit methods that involve such traces of lone quark loops if possible.

4.2.3 Two-quark – two-meson

Correlators in this section of the matrix are the spatially extended variants of the previously discussed diagram type. Depending on the operator structure the $2 \times$ connected diagram takes the shape of a triangle or becomes truly “disconnected”.

C_{15} ($1 \equiv q\bar{q}$; $5 \equiv K\bar{K}$, 2part)

With a propagation of one quark flavor only within one of the two timeslices, C_{15} can be computed efficiently using sequential propagators in the source timeslice. Here, the relative difference in computational effort between the two techniques is comparable to matrix element C_{11} , and, similarly, is the one-end trick also here the method of choice, cf. Figure 4.5.

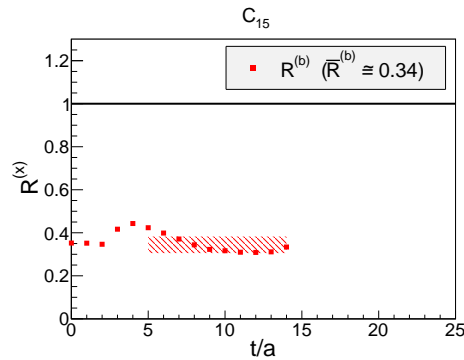
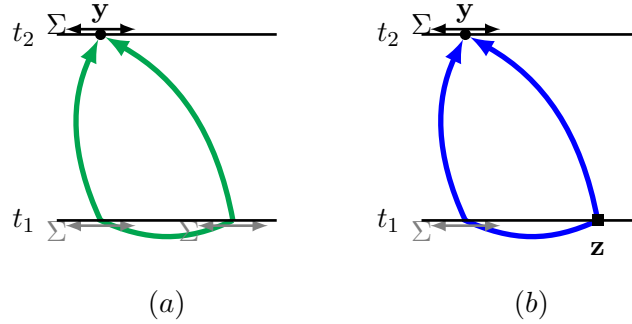


FIG. 4.5: Efficiency of different methods for C_{15} .

C_{16} ($1 \equiv q\bar{q}$; $6 \equiv \eta_s\pi$, 2part)

C_{16} becomes a product of two disconnected pieces. The quark loop can either be computed using a point-to-all propagator, truncated to a propagation to its origin, or a stochastic timeslice-to-all propagator, truncated to its source timeslice. With this remark on stochastic timeslice-to-all propagators and the experience from C_{13} we safely exclude diagrams with stochastic loops in their sink timeslice and consider the following methods as promising.

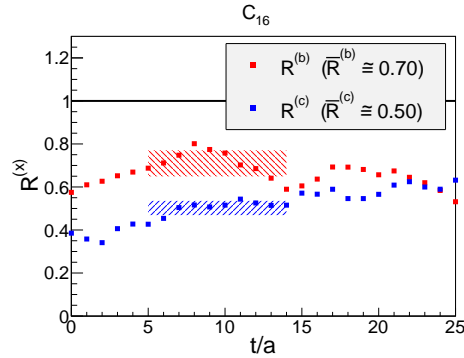
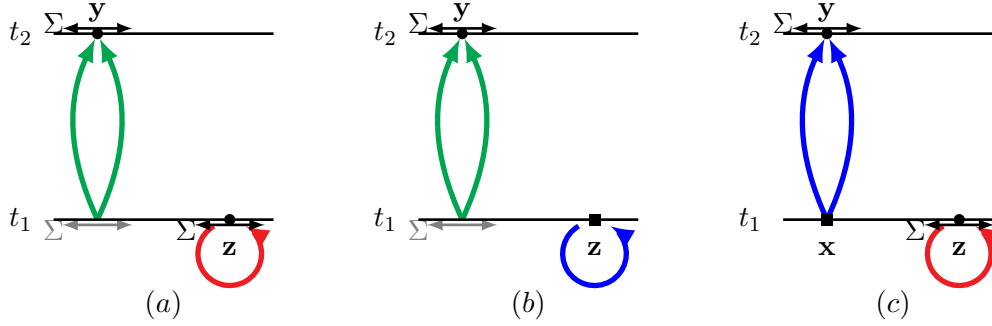


FIG. 4.6: Efficiency of different methods for C_{16} .

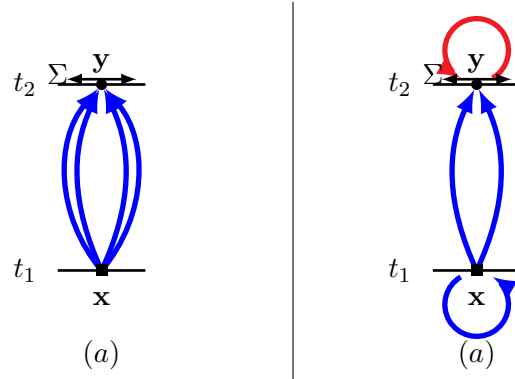
Certainly do method (a) and (c) suffer from stochastic noise similarly as C_{13} does. For these two methods, however, the noise generated by the stochastic loop is located only on the source timeslice, affecting each temporal separation of the correlator equally. With a stochastic loop in the sink timeslice, as it was the case for C_{13} , each temporal separation is affected by an always different stochastic noise for the loop. Consequently, do we obtain a much smoother signal for the diagram by this approach, reflected in a smooth behavior of the quality ratios.

Although method (a) introduces a rather large number of stochastic noise terms in comparison to (b) and (c), it averages the diagram over space at both timeslices and eventually proves itself to be the most efficient choice.

4.2.4 Four-quark – four-quark

$C_{22}, C_{23}, C_{24}, C_{33}, C_{34}, C_{44}$ 4×4 & 2×2 connected ($2 \equiv K\bar{K}$, point; $3 \equiv \eta_s\pi$, point; $4 \equiv Q\bar{Q}$)

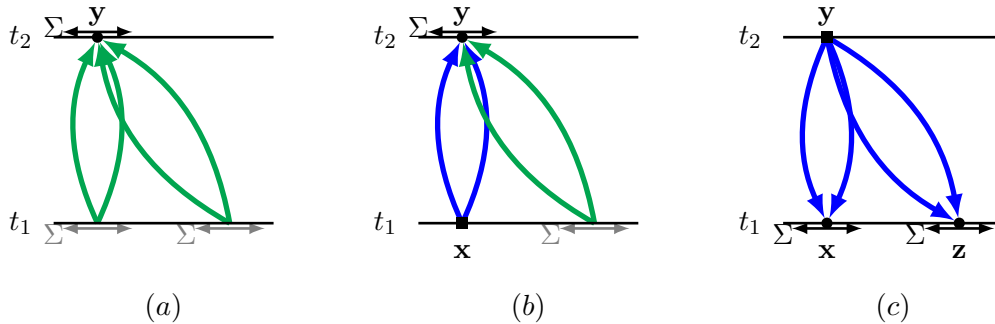
The cross-correlators of the three four-quark interpolators have different color and spin structures, but are identical with respect to spacetime, cf. Figure 3.3 where the sub 3×3 matrix is emphasized by thick lines. Therefore, it is reasonable to discuss these diagram types together. Due to their compact structure where all four quarks are located at the same point in space, both at t_1 and t_2 , there is only a single possibility to compute these types of diagrams efficiently.



4.2.5 Four-quark – two-meson

$C_{25}, C_{26}, C_{35}, C_{36}, C_{45}, C_{46}$ 4×2 connected ($2 \equiv K\bar{K}$, point; $3 \equiv \eta_s\pi$, point; $4 \equiv Q\bar{Q}$; $5 \equiv K\bar{K}$, 2part; $6 \equiv \eta_s\pi$, 2part)

The spatial representation of the 4×2 connected cross-correlators between all two-meson and all four-quark interpolators is identical and only differs in their color and spin structure. As before, these diagrams are computed with the same methods, independently of where they appear in the matrix.



Method (b) splits into two possible realizations (b_1) and (b_2) for all diagrams that include operator $O^{\eta_s\pi, 2\text{part}}$. For these correlators each technique can be assigned to a single quark flavor, i.e. point-to-all propagators for the emerging η_s meson and the one-end trick for the Pion (method (b_1)), or vice-versa (method (b_2)).

Figure 4.7 shows the numerical comparison of these methods for all six scenarios. The conclusions are in agreement with the tendencies seen in nearly all prior diagram types. The one-end trick is an excellent choice and estimating both propagator products with this technique results in the most efficient method to compute this element for all six cases. To some extent surprising is the fact that method (b) without translational invariance but with stochastic noise surpasses method (c), which only sacrifices translational invariance.

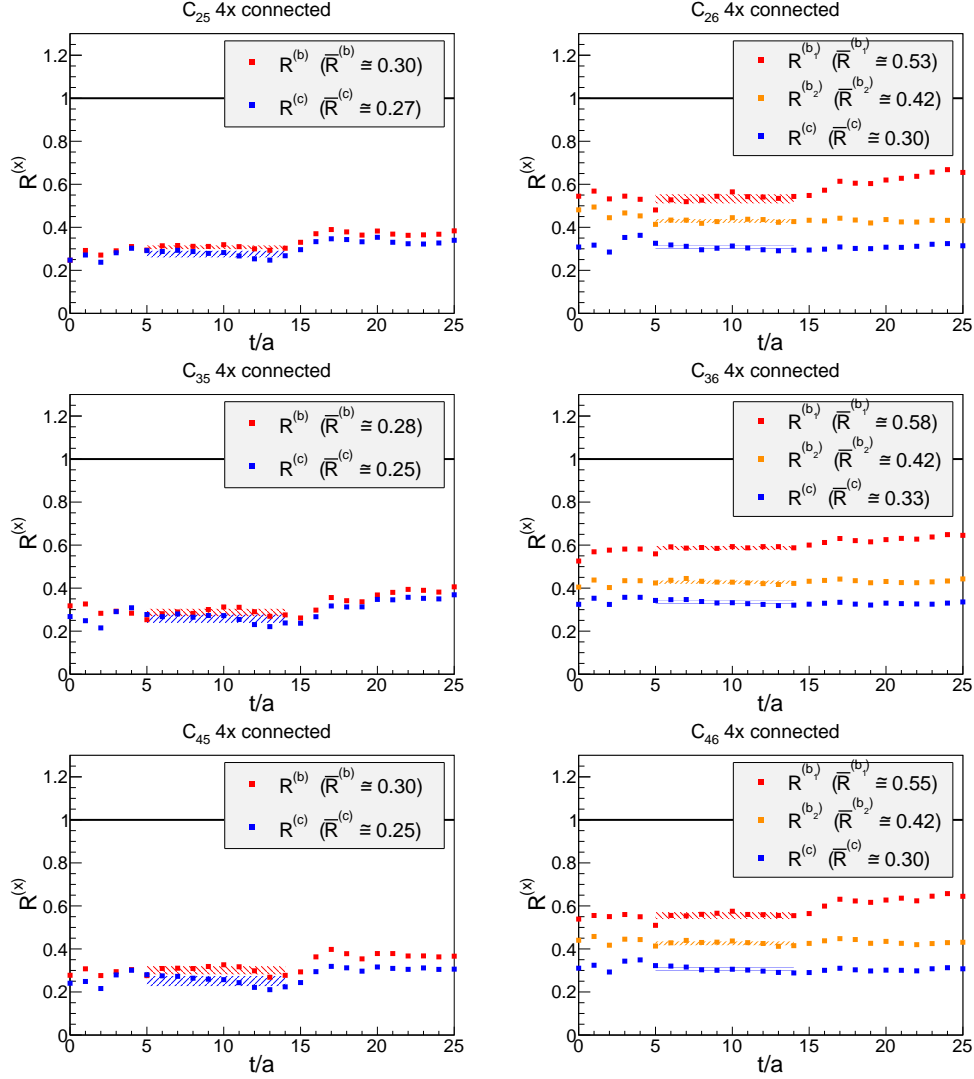


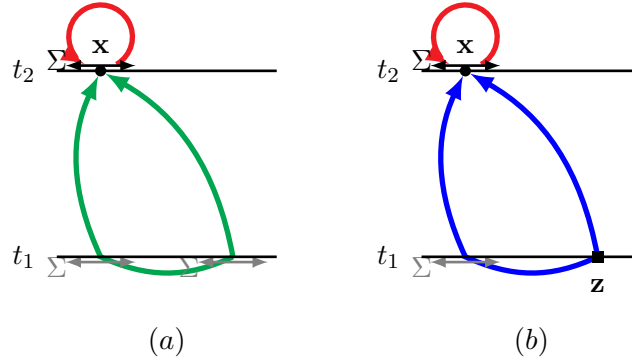
FIG. 4.7: Efficiency of different methods for $C_{25}, C_{26}, C_{35}, C_{36}, C_{45}, C_{46}$ 4x-connected. Methods (b) splits into two versions in the right column due to the possibility to assign one technique solely to one quark flavor.

It appears that omitting a sum over space where only two quark lines end (cf. method (b)) is more efficient than omitting a sum over space where four quark lines end (cf. method (c)).

The findings that method (b_1) is superior to method (b_2) is consistent with our expectation. One reason is that the 12 inversions needed for the point-to-all propagators require less computing time for the heavier s quark than for the lighter u/d quarks. Secondly has the one-end trick been found to be more efficient in comparison to point-to-all propagators with decreasing quark masses [99].

C_{25}, C_{35}, C_{45} $2 \times$ connected ($2 \equiv K\bar{K}$, point; $3 \equiv \eta_s\pi$, point; $4 \equiv Q\bar{Q}$; $5 \equiv K\bar{K}$, 2part)

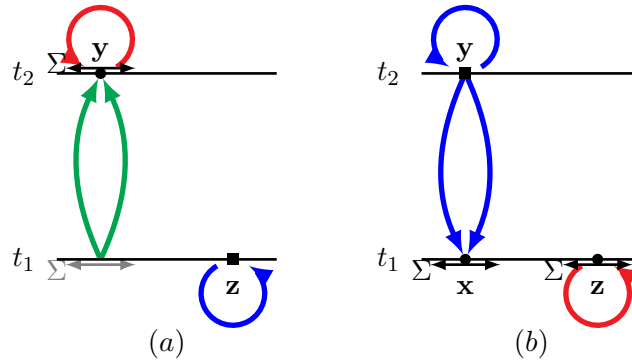
Similar to C_{15} is the procedure of sequential propagation required to compute the triangular part of the diagram. In addition, there is now also a loop propagator at the end points of the propagators connecting the timeslices, which is estimated in both scenarios by a stochastic timeslice-to-all propagator.



For C_{35} the quark loop is again disconnected in spin space, which leads to more severe statistical fluctuations, shown in Figure 4.8. Especially for larger temporal separations of the correlator, cf. Section 4.2.2.

C_{26}, C_{36}, C_{46} $2 \times$ connected ($2 \equiv K\bar{K}$, point; $3 \equiv \eta_s\pi$, point; $4 \equiv Q\bar{Q}$; $6 \equiv \eta_s\pi$, 2part)

With quark loops at both timeslices of the correlator, at least one of them needs to be computed using a stochastic timeslice-to-all propagator. The candidate methods are



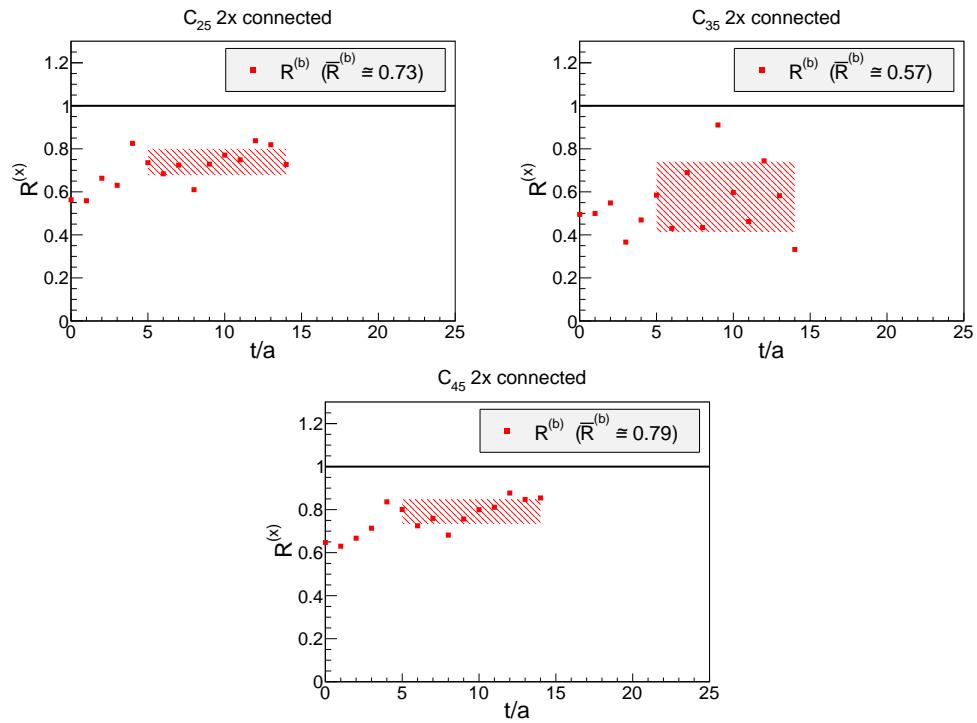


FIG. 4.8: Efficiency of different methods for C_{25}, C_{35}, C_{45} 2 \times connected.

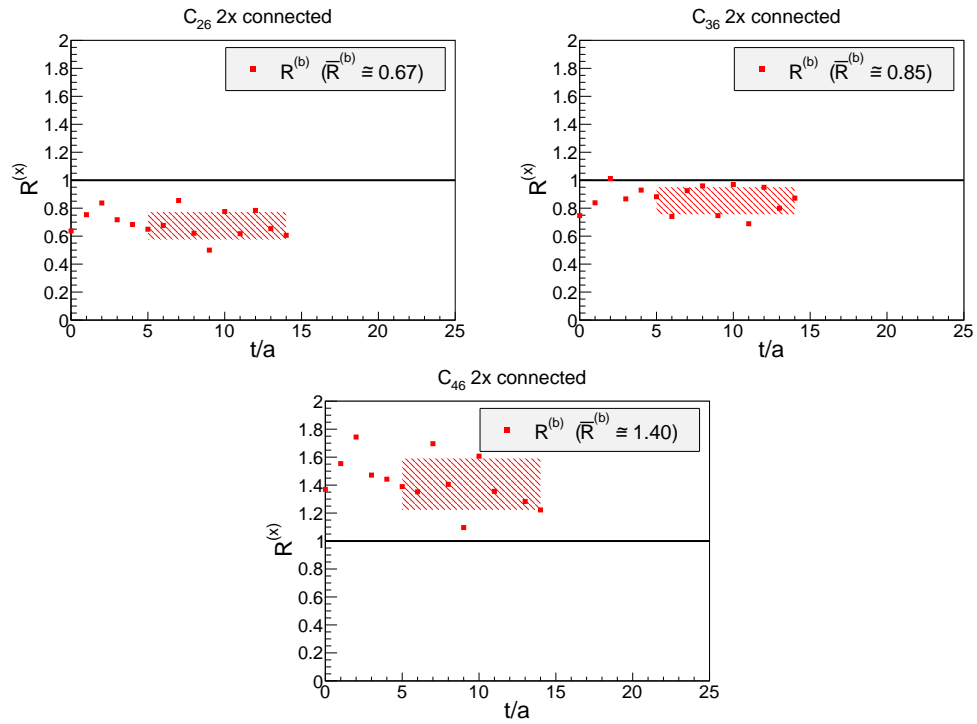


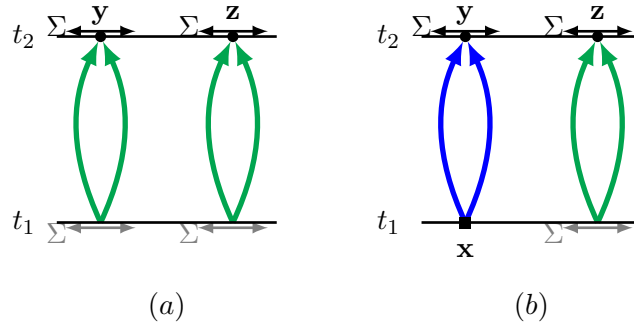
FIG. 4.9: Efficiency of different methods for C_{26}, C_{36}, C_{46} 2 \times connected.

Figure 4.9 shows the numerical comparison of these methods. It is interesting to note that for the first time a method is significantly influenced by the color and spin structure of a diagram. Method (a) remains to be superior for C_{26} and C_{36} , while this is no longer the case for C_{46} .

4.2.6 Two-meson – two-meson

C_{55}, C_{66} 4×connected ($5 \equiv K\bar{K}$, 2part; $6 \equiv \eta_s\pi$, 2part)

Each of the two disconnected pieces of these diagrams corresponds to a C_{11} -like correlator and thus the methods discussed in section 4.2.1 are applied to both parts.



Again, method (b) splits into two possible realizations for C_{66} , due to the flavor structure of the creating operator $O^{\eta_s\pi, 2\text{part}}$. (b_1) is where the light quarks are estimated with the one-end trick and strange quarks with point-to-all propagators, and (b_2) describes the opposite scenario.

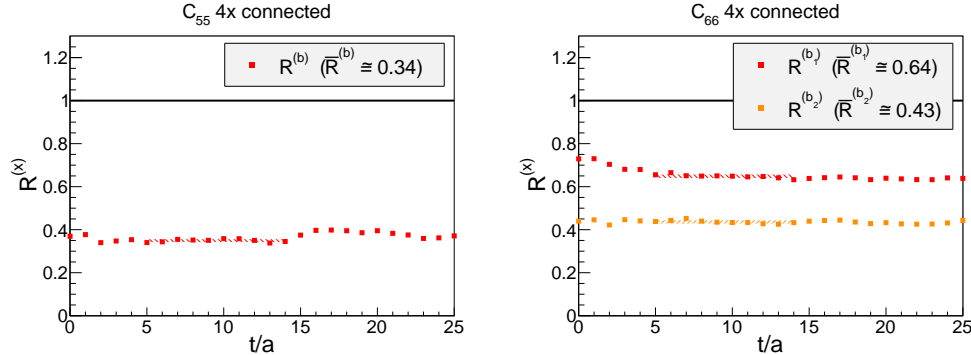
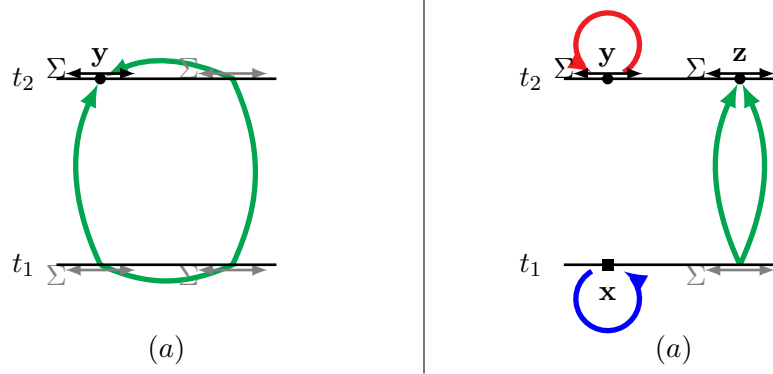


FIG. 4.10: Efficiency of different methods for C_{55}, C_{66} 4×connected.

The results of comparing these methods are essentially the same as in Section 4.2.5 for the 4×connected diagrams. Only difference here is that the inner products of the solutions of the linear systems are summed at two independent space-points (\mathbf{y} and \mathbf{z}) at the sink timeslice. The consistent application of the one-end trick proves to be more efficient as it estimates the full dynamics of the system at both timeslices. Method (b_1) is superior to method (b_2), due to a reduced numerical effort but also due to the increased efficiency of the one-end trick if applied to light quarks [99].

C_{55}, C_{66} $2\times$ connected ($5 \equiv K\bar{K}$, 2part; $6 \equiv \eta_s\pi$, 2part)

The $2\times$ connected pieces of both diagonal two-meson–two-meson elements are each computed efficiently by only a single method.

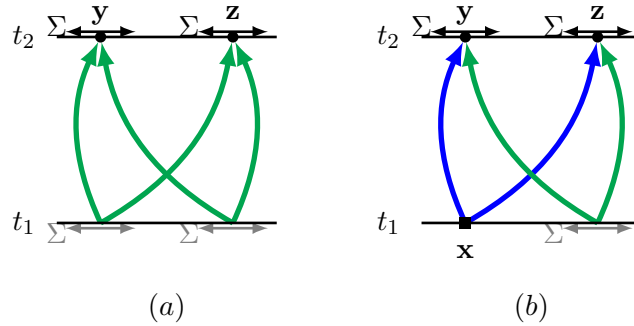


$O^{K\bar{K}, 2\text{part}}$ (left diagram) connects the quark fields to a box-like diagram, so that sequential source and sink propagators become mandatory. This diagram can be computed efficiently with the one-end trick, as prior discussed diagram types strongly suggest.

$O^{\eta_s\pi, 2\text{part}}$ (right diagram) introduces spatially separated loop propagators, which splits the correlator into three disconnected pieces. The loop at the sink needs to be estimated by a stochastic timeslice-to-all loop, inevitably resulting in large stochastic noise contributions to the correlator.

C_{56} $4\times$ connected ($5 \equiv K\bar{K}$, 2part; $6 \equiv \eta_s\pi$, 2part)

Similar to its diagonal partners C_{55}, C_{66} $4\times$ connected, there are two promising methods.



To maximize efficiency it is advisable to let $O^{\eta_s\pi, 2\text{part}}$ act as the creating operator on the source timeslice. Doing so reduces the amount of inversions necessary for each quark flavor as degenerate quark masses share their source terms. One can think of method (b) with inverted propagator directions and interchanged source/sink timeslices as method (c). This method would correspond to $O^{K\bar{K}, 2\text{part}}$ as source operator and require twice the computational effort compared to method (b). Results of the numerical comparison shown in Figure 4.11 are in agreement with the rest of the study. Effects from the application of the one-end trick on different quark masses are observed to be

absent. The reason for this is that the inner products of solutions consist of mixtures of propagator techniques *and* are averaged independently.

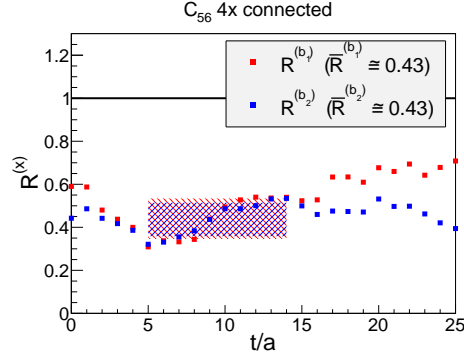
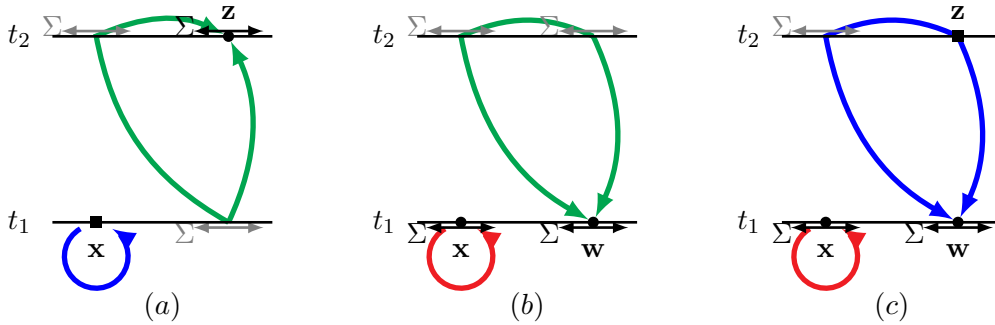


FIG. 4.11: Efficiency of different methods for C_{56} 4×connected.

C_{56} 2×connected ($5 \equiv K\bar{K}$, 2part; $6 \equiv \eta_s\pi$, 2part)

The last diagram type we discuss is again of triangular shape, but in contrast to C_{25}, C_{35} and C_{45} , with a truly disconnected quark loop. We utilize sequential propagation in combination with a point-to-point or a stochastic timeslice-to-timeslice loop.



A numerical comparison of the methods is shown in Figure 4.12. Method (a) and (b) perform on a similar level. This is in relation to the results for C_{16} not too surprising. There, methods which placed the loop on the source timeslice were considered to be the most efficient. From the perspective of computational costs this might be evident, but also the signal obtained from these methods was superior compared to methods which place the loop on the sink timeslice (results which are not presented here). This observation basically remains true for element C_{56} 2×connected. An additional method which considers a stochastic timeslice-to-timeslice loop instead of a point-to-point loop in method (a) was not considered. It can be expected that this option further increases the efficiency of the computation of this diagram type by $\approx 20 - 30\%$.

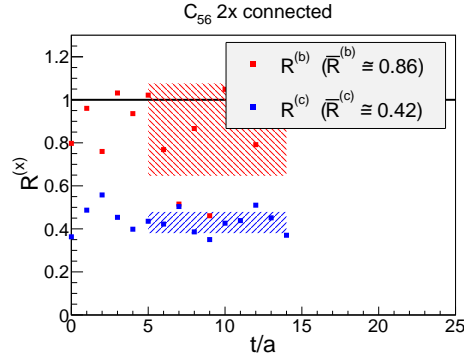


FIG. 4.12: Efficiency of different methods for C_{56} $2\times$ connected.

4.2.7 Efficiency for different flavor setups

In addition to the flavor setup $\{\bar{d}, u, \bar{s}, s\}$ we employ to study the $a_0(980)$ we also consider the flavor setup $\{\bar{c}, s, \bar{u}, u\}$, in order to investigate the $D_{s_0}^*(2317)$. Since color and spin structure of the respective diagrams remain unchanged and only quark flavors of propagators have to be rearranged, it is interesting to see, whether the efficiency of different methods is affected by these changes.

The most obvious change is that for the heavy flavor setup the light quark will have starting and endpoints on a single timeslice. As mentioned several times such diagrams are more expensive to compute, but also provide a much worse signal-to-noise ratio compared to diagrams without such propagators, cf. Section 3.4. However, for our computations we utilize an adaptive multigrid solver, rather than a conventional iterative procedure like BiCGSTAB. Consequently, inversions of light quark masses are much faster compared to regular setups, which leaves us with relatively small $\sqrt{\tau^{(\text{light})}}/\sqrt{\tau^{(\text{heavy})}}$ in the quality ratios (4.2). Numerical setups which do not treat light quark masses in a refined way are hence expected to be affected even more severely by the wrong choice of methods than presented in the following.

Diagrams whose expenses are dominated by a quark loop are expectedly sensitive to the change of the flavor setup.

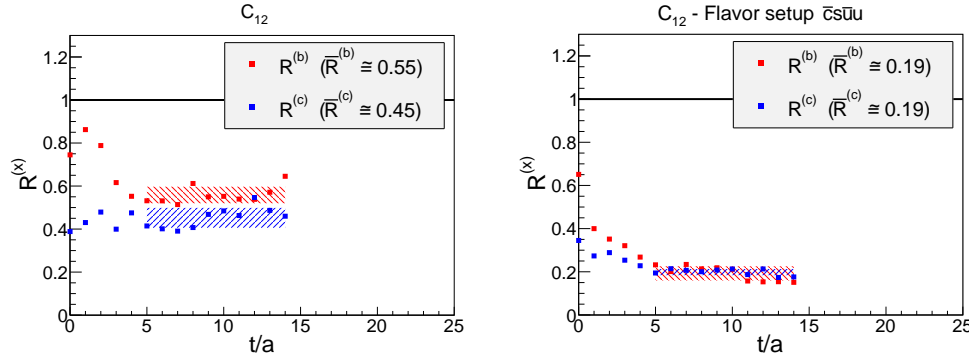


FIG. 4.13: Efficiency of different methods for C_{12} in two flavor setups: $\{\bar{d}, u, \bar{s}, s\}$ (left) and $\{\bar{c}, s, \bar{u}, u\}$ (right).

The choice of techniques becomes more important seen in e.g. element C_{12} plotted in Figure 4.13. Method (b) and (c) are dominated by a stochastic timeslice-to-all propagator. Hence their efficiency can be expected to decrease even further in the absence of sound solver procedures that allow an accelerated computation of light quark propagators.

The transition to another flavor setup leaves the efficiency ratings of all $4\times$ connected diagrams qualitatively unchanged, shown by the example of $C_{26}^{4\times\text{connected}}$ in Figure 4.14. These diagram types are barely sensitive to the flavor content at all, as they are simply computed by mere timeslice-to-all techniques.

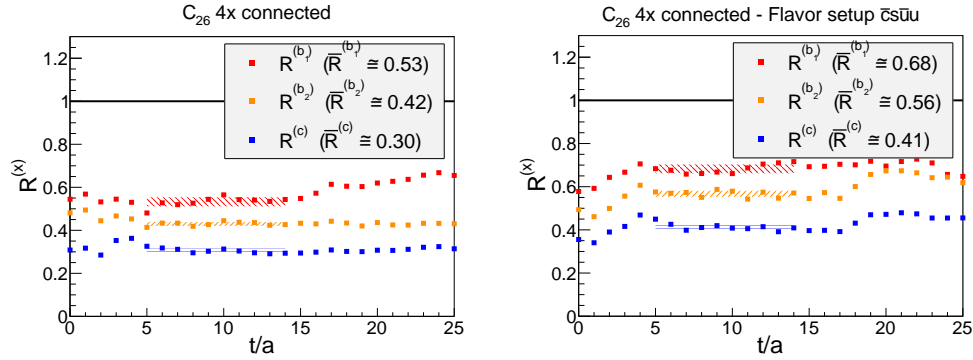


FIG. 4.14: Efficiency of different methods for C_{26} $4\times$ connected in two flavor setups: $\{\bar{d}, u, \bar{s}, s\}$ (left) and $\{\bar{c}, s, \bar{u}, u\}$ (right). Efficiencies remain qualitatively unchanged due to the sole presence of source-sink propagators.

The most drastic changes in quality ratios are observed for four-quark–two-meson $2\times$ connected diagrams. Yet the magnitudes of the changes are still too small to speak of any significant alteration. Altogether do the diagrams C_{25} , C_{35} , C_{45} , C_{26} and C_{36} show an increased tendency for a balanced quality ratio between the two respective methods, cf. Figure 4.15, where $C_{26}^{2\times\text{connected}}$ is plotted as an example. C_{46} $2\times$ connected remains to favor method (b) over method (a).

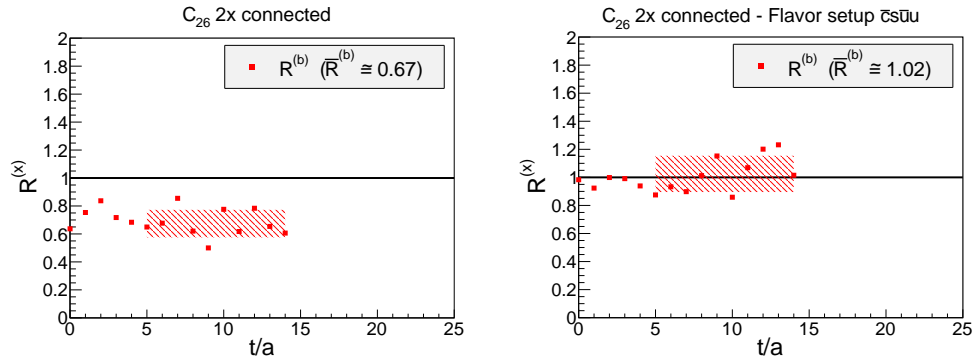


FIG. 4.15: Efficiency of different methods for C_{26} $2\times$ connected in two flavor setups: $\{\bar{d}, u, \bar{s}, s\}$ (left) and $\{\bar{c}, s, \bar{u}, u\}$ (right). Similar to the other four-quark–two-meson $2\times$ connected diagrams become the quality ratios balanced for the heavy flavor setup.

4.3 Relevance of $2\times$ connected contributions

After the most efficient methods are determined for every diagram we restrict ourselves to utilize only these particular methods. We have already seen that $2\times$ connected contributions to correlators with four quarks pose an exceptional effort to compute. Yet to this point it remains unclear how large the statistical errors on these contributions actually are and, more interestingly, how large they are in comparison to the statistical errors of the $4\times$ connected contributions. Since, ultimately, the larger of the two errors will dominate the error of the matrix element. To compare the statistical errors of both contributions we use again the quality ratio defined in (4.2), but instead of different methods we plug in the two different contributions to the correlator, i.e. $R^{2\times\text{con}}(t) \equiv R^{4\times\text{con},2\times\text{con}}(t)$.

In the top row of Figure 4.16 the quality ratios are shown for all six correlation matrix elements with four quarks on the same site from the $\{\bar{d}, u, \bar{s}, s\}$ flavor setup, i.e. C_{ij} with $i, j \in [2, 3, 4]$. They decrease rapidly and already at a temporal separation of $t/a \gtrsim 6$ they are below 0.1, or even significantly smaller. Consequently, the statistical error of the correlation matrix elements will be governed by the $2\times$ connected diagrams. Determining the optimal method of computation for the $2\times$ connected is thus much more important than for the $4\times$ connected diagrams.

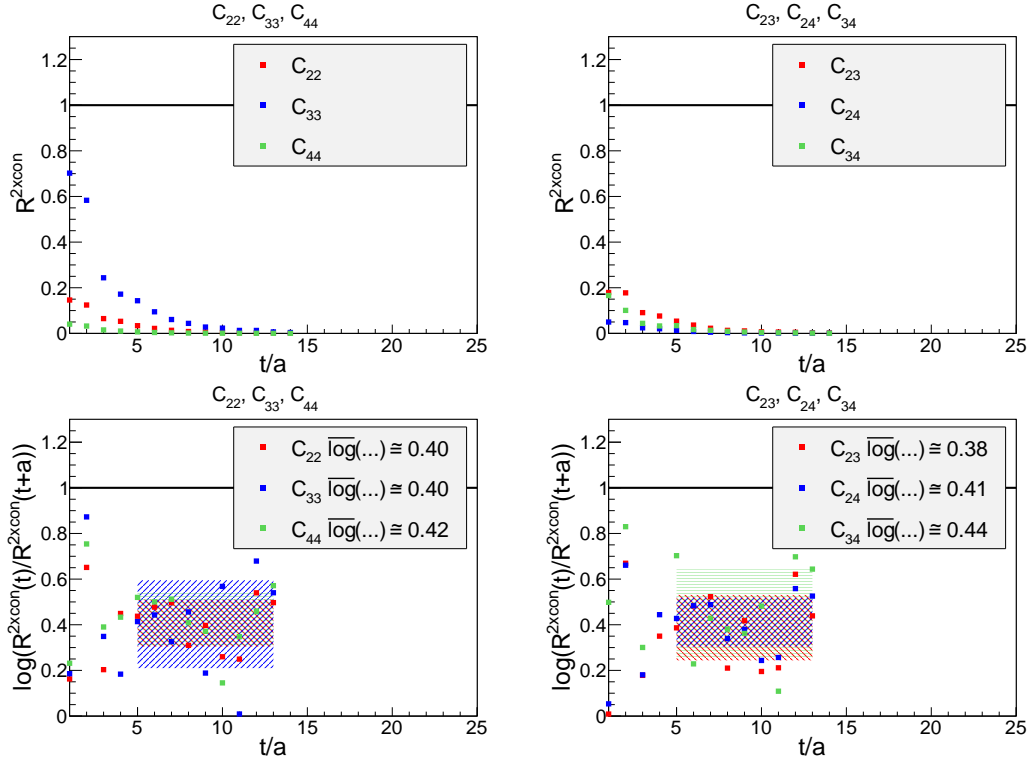


FIG. 4.16: Comparison of $4\times$ and $2\times$ connected contributions for C_{ij} with $i, j \in [2, 3, 4]$ for the $\{\bar{d}, u, \bar{s}, s\}$ flavor setup.

In the bottom row of Figure 4.16 we plot a related quantity to investigate the drastic

difference in the statistical errors in more detail. Assuming an exponential behavior $R^{2 \times \text{con}}(t) \propto e^{-\alpha t}$ the plotted quantity $\log(\dots)$ extracts the exponent α . For all six cases shown the mean of $\log(\dots)$ fluctuates around the same constant value, i.e. $\alpha \approx 0.4$, which indeed shows that the statistical error of the $2 \times$ connected diagrams increases exponentially in comparison to the $4 \times$ connected diagrams, i.e. proportionally to $e^{\alpha t}$. The remaining elements of the correlation matrix consisting of $4 \times$ and $2 \times$ connected contributions exhibit the same feature and are presented in [27].

To understand this behavior we want to consider squared diagrams, which are proportional to the squared statistical error of a diagram. From the resulting quantum numbers we can then derive the respective decay of the correlation function. The squared diagrams of correlation functions from three point-interpolators C_{ij} with $i, j \in [2, 3, 4]$ are shown in Figure 4.17.

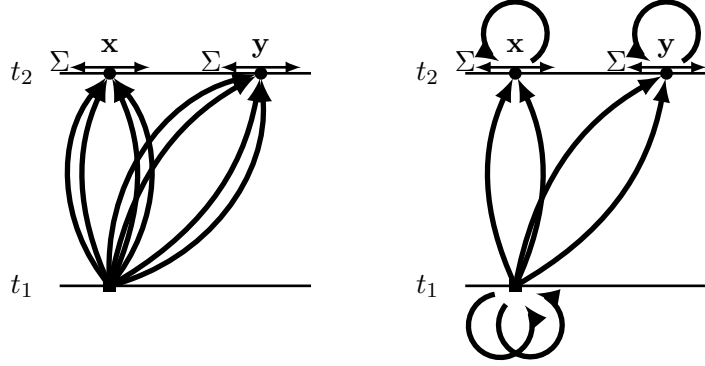


FIG. 4.17: Squared diagrams, which are proportional to the squared statistical errors of the $4 \times$ connected diagram (left) and the $2 \times$ connected diagram (right) of C_{ij} with $i, j \in [2, 3, 4]$.

Such a structure corresponds to a correlation function of two eight-quark operators with appropriately chosen color, spin and spacetime structure, e.g.

$$\left(\Delta C_{22}^{4 \times \text{connected}}(t)\right)^2 \propto \left\langle O^{2\text{part}}[s^{(1)}, s^{(2)}, s^{(3)}, s^{(4)}](t_2) O^{\text{point}}[s^{(1)}, s^{(2)}, s^{(3)}, s^{(4)}]^\dagger(t_1) \right\rangle, \quad (4.3)$$

$$\left(\Delta C_{22}^{2 \times \text{connected}}(t)\right)^2 \propto \left\langle O^{2\text{part}}[s^{(1)}, s^{(1)}, s^{(2)}, s^{(2)}](t_2) O^{\text{point}}[s^{(3)}, s^{(3)}, s^{(4)}, s^{(4)}]^\dagger(t_1) \right\rangle, \quad (4.4)$$

with operator structures

$$\begin{aligned} O^{2\text{part}} &= \left(\sum_{\mathbf{x}} \left(\bar{s}_1(\mathbf{x}) \gamma_5 u(\mathbf{x}) \right) \left(\bar{d}(\mathbf{x}) \gamma_5 s_2(\mathbf{x}) \right) \right) \left(\sum_{\mathbf{y}} \left(\bar{s}_3(\mathbf{y}) \gamma_5 u(\mathbf{y}) \right) \left(\bar{d}(\mathbf{y}) \gamma_5 s_4(\mathbf{y}) \right) \right), \\ O^{\text{point}} &= \sum_{\mathbf{x}} \left(\bar{s}_1(\mathbf{x}) \gamma_5 u(\mathbf{x}) \right) \left(\bar{d}(\mathbf{x}) \gamma_5 s_2(\mathbf{x}) \right) \left(\bar{s}_3(\mathbf{x}) \gamma_5 u(\mathbf{x}) \right) \left(\bar{d}(\mathbf{x}) \gamma_5 s_4(\mathbf{x}) \right), \end{aligned} \quad (4.5)$$

where different degenerate strange quarks $s^{(i)}$ are introduced to ensure that the correlation functions (4.3) and (4.4) reproduce exactly the squared diagrams shown in

Figure 4.17. Both $O^{2\text{part}}$ and O^{point} with flavor structure $\{s^{(1)}, s^{(2)}, s^{(3)}, s^{(4)}\}$ generate quantum numbers $I(J^P) = 2(0^+)$ and strangeness $S^{(1,3)} = +1$ and $S^{(2,4)} = -1$ for the four strange flavors, corresponding to an asymptotic decay according to $e^{-4m_K t}$. Similarly, in (4.4) the quantum numbers will again be $I(J^P) = 2(0^+)$, but strangeness $S^{(1)} = S^{(2)} = S^{(3)} = S^{(4)} = 0$ for all four strange flavors. Hence, the correlation function will decay asymptotically according to $e^{-2m_\pi t}$. Consequently we obtain a ratio of relative errors of the two diagrams of

$$\left. \frac{\Delta C^{4\times\text{connected}}(t)}{\Delta C^{2\times\text{connected}}(t)} \right|_{\bar{d}u\bar{s}s} \propto e^{-(2m_K - m_\pi)t}. \quad (4.6)$$

Inserting the mass values for our lattice setup (cf. Figure 5.2) yield an $\alpha_{\bar{d}u\bar{s}s} \approx 0.41$, which is in agreement with the numerical findings from Figure 4.16. Similarly, for the $\{\bar{c}, s, \bar{u}, u\}$ flavor setup we find a ratio of

$$\left. \frac{\Delta C^{4\times\text{connected}}(t)}{\Delta C^{2\times\text{connected}}(t)} \right|_{\bar{c}s\bar{u}u} \propto e^{-(m_K + m_D - m_{D_s})t}. \quad (4.7)$$

Mass values of our setup (cf. Figure 5.16) yield this time a much milder $\alpha_{\bar{c}s\bar{u}u} \approx 0.224$, which is also in agreement to analogous findings for this flavor setup, shown in Figure 4.18.

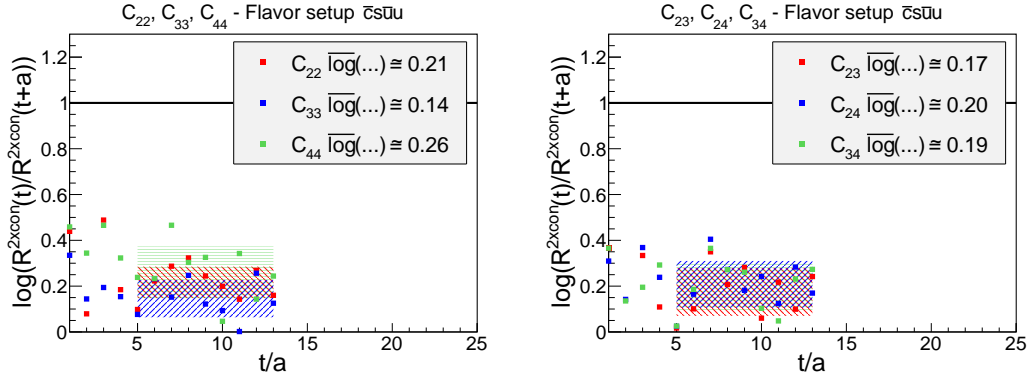


FIG. 4.18: Comparison of $4\times$ and $2\times$ connected contributions for C_{ij} with $i, j \in [2, 3, 4]$ for the $\{\bar{c}, s, \bar{u}, u\}$ flavor setup.

In conclusion is the relative exponential increase of the statistical errors of the $2\times$ connected diagrams not to be associated with the employed method of computation, but much rather an intrinsic property of these diagrams.

After identifying $2\times$ connected diagrams of correlators as numerically expensive and inherently affected by large statistical fluctuations it is eventually interesting to consider their impact on the total correlation matrix. Rather obvious is their importance in regard to connecting the conventional two-quark operator analysis with a four-quark operator analysis. It becomes evident in Figure 3.3 that correlation functions on the off-diagonal to the quark-antiquark operator O^1 are solely composed of $2\times$ connected diagrams and connect these otherwise separated bases. Hence, their omission in any computation

makes a complete analysis of even conventional mesonic states in the neighborhood of multi-particle states impossible.

On the other hand it might possibly be that these elements, in our case C_{1i} with $i \in [2, \dots, 7]$, of the matrix are negligible nevertheless. This would lead to a scenario similar to their omission, where any $n \times n$ study would effectively break down into an approximate $1 \times 1 + (n - 1) \times (n - 1)$ study. In return, one could not undoubtedly claim having studied a tower of states, but possibly rather two independent sectors. In Figure 4.19 we plot off-diagonal correlation functions of the quark-antiquark operators scaled to their related diagonal correlation functions for both flavor setups. From ratios $\gg 0$ we anticipate non-negligible interactions between the two-quark states and the respective multi-quark states. In Figure 4.19 it can be seen that this is the case for both correlation matrices.

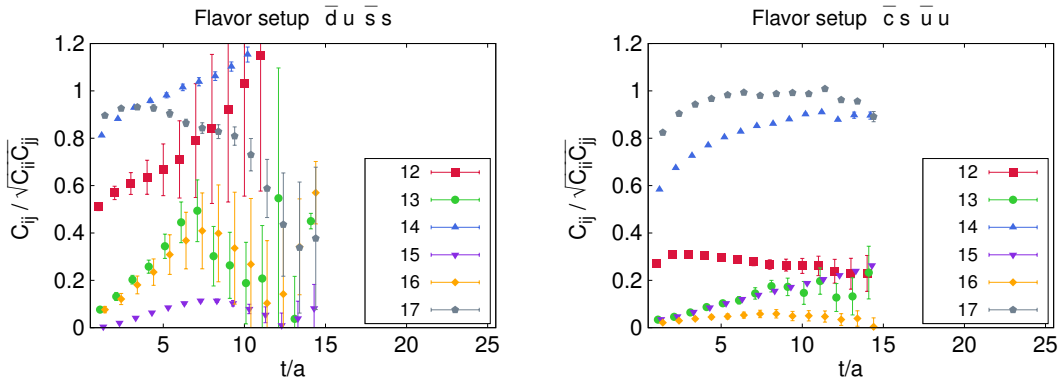


FIG. 4.19: Off-diagonal elements C_{1i} normalized to their related diagonal elements for the flavor setups $\{\bar{d}, u, \bar{s}, s\}$ (left) and $\{\bar{c}, s, \bar{u}, u\}$ (right). Effects in the light tetraquark study for $t/a \gtrsim 8$ are caused by finite size effects, which are addressed later on.

For the light and heavy tetraquark candidate studied in this thesis, the conventional quark-antiquark interpolating field operators are of the form $O^1|_{\bar{d}u\bar{s}s} \simeq (\bar{d}u)$ and $O^1|_{\bar{c}s\bar{u}u} \simeq (\bar{c}s)$, respectively, while O^7 refers to a heavier diquark-antidiquark structure than O^4 , cf. Section 3.3.1.

The most striking difference is the much more drastic error on the results from the light setup. This is not alone an effect of the intrinsically worse $2 \times$ connected diagrams within this setup, but mainly caused due to finite size effects. Such effects are anticipated in (3.7) and the detailed discussion is postponed to Chapter 5.1.

However, for $t/a < 8$ operator $O^1|_{\bar{d}u\bar{s}s} \simeq (\bar{d}u)$ is evidently integrated to the rest of the matrix and in both setups we observe a strong relation to the diquark-antidiquark operators. In the study of the $D_{s0}^*(2317)$ we observe a weak coupling of the quark-antiquark operator to a majority of the multi-quark operators, except for the diquark-antidiquark structures.

Another important aspect of $2 \times$ connected diagrams concerns their relevance to the total correlator. Since they are numerically expensive and still characterized by usually poor signal-to-noise ratios is their computation often omitted in earlier studies [21, 100].

To demonstrate their impact to the total correlator we plot in Figure 4.20 the absolute value of selected $2\times$ connected diagrams divided by the sum of the absolute values of both diagram types. For the example correlation functions we show the diagonal elements of the matrices in the light and heavy flavor setup. Again the note of caution, that obvious changes in the behavior of some correlators in the light flavor setup for $t/a \gtrsim 8$ are caused by finite size effects. For reliable results we thus focus on values of the correlators for $t/a < 8$. One striking exception in both scenarios is C_{55} . In both flavor setups is the box contribution to the correlator two orders of magnitudes smaller than the diagram with four propagators connecting the two timeslices. The addition of $2\times$ connected diagrams is hence affecting the total correlator only by a few percent. It can be expected that the large spatial separation of the strange-antistrange quark pair is the reason for this large suppression.

In the heavy flavor setup finite size effects to the $2\times$ connected diagrams are not nearly as severe as in the light setup. Instead we observe a very smooth behavior of these diagrams, where the total correlators are not drastically affected by $2\times$ connected diagrams, but rather receive an increase of statistical errors.

Mutual agreement between both analysis is found in regard to the relevance of $2\times$ connected contributions to correlators deriving from a diquark-antidiquark operator structure. In Figure 4.20 this corresponds to C_{44} and C_{77} in both setups. Although the light setup provides reliable evidence only at small temporal separations are these correlators evidently dependent on these diagrams. This extends also to the respective off-diagonal elements. In conclusion it is expected that the computation of all contributing pieces to this correlator structure is vital to correctly model a diquark-antidiquark structure and, hence, to introduce any chance of observing a bound four-quark state of this structure.

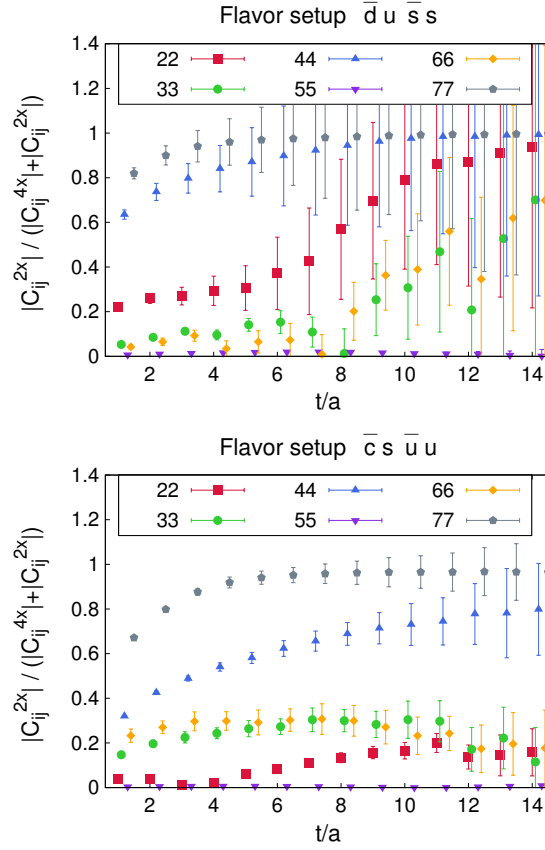


FIG. 4.20: Relevance of $2\times$ connected contributions to the total correlator, shown for all diagonal elements of both flavor setups. Relative signs between the two contributing diagrams are not taken into account. In the study of the light flavor setup the increasing relevance of $2\times$ connected contributions $t/a \gtrsim 8$ is caused by finite size effects. In both scenarios the diquark-antidiquark correlator receives large contributions from the $2\times$ connected diagrams.

5

INVESTIGATION OF SCALAR TETRAQUARK CANDIDATES

In this chapter we present our results for the investigation of the light scalar tetraquark candidate $a_0(980)$ and the heavy scalar tetraquark candidate $D_{s0}^*(2317)$. Our analyses are based on a variational approach - introduced in Section 3.2 - allowing us an extensive study of the particles of interest by employing several operator sets with well-suited quark structures (3.19). The presentation of both candidates follows the same scheme. In a first step we compute the pseudoscalar single particle levels within our lattice setup to calculate the infinite volume two particle levels. These levels differ from physical observations [29], but provide an energy range where the possible candidate is expected to be found within computations.

For the analysis of four-quark states we omit in a first step $2\times$ connected contributions to correlators. These diagrams are inherently worse in their signal and, as we will see, are also be affected by finite volume effects. As they are excluded for a first study the employed operator set decouples, i.e. two-quark and four-quark operators are studied separately. Eventually, we include all diagrams to our analysis and check for a possible third low-lying state close to the two-particle levels.

5.1 The light candidate: $a_0(980)$

The $a_0(980)$ is an isovector in the poorly understood nonet of light scalars ($J^P = 0^+$). The other scalars are the $\sigma \equiv f_0(600)$ and $f_0(980)$ with isospin 0, and the $\kappa \equiv K(800)$ with isospin 1/2. In contrast to expectations from the naïve quark model is the observed mass hierarchy of these scalars inverted. The $a_0(980)$ is measured around $\sim 1\text{GeV}$ and features a surprising mass degeneracy with the $f_0(980)$.

Based on the conventional quark-antiquark interpretation isospin $I = 1$ can only be realized with two light quarks, whereas for $I = 0$ either two light or two strange quarks are possible. Hence the conventional flavor structure of these scalars in an $SU(3)$ flavor nonet reads

$$\begin{aligned} I = 0 & \quad \rightarrow \quad \sigma = \frac{1}{\sqrt{2}}(u\bar{u} + d\bar{d}) \quad , \quad f_0 = s\bar{s}, \\ I = 1/2 & \quad \rightarrow \quad \kappa^+ = u\bar{s} \quad , \quad \kappa^0 = d\bar{s} \quad , \quad \bar{\kappa}^0 = s\bar{d} \quad , \quad \kappa^- = s\bar{u}, \\ I = 1 & \quad \rightarrow \quad a_0^+ = u\bar{d} \quad , \quad a_0^0 = \frac{1}{\sqrt{2}}(u\bar{u} - d\bar{d}) \quad , \quad a_0^- = d\bar{u}. \end{aligned} \tag{5.1}$$

Alternatively could one assume a four-quark structure with quark content

$$\begin{aligned}
 I = 0 & \quad \rightarrow \quad \sigma = ud\bar{u}\bar{d} \quad , \quad f_0 = \frac{1}{\sqrt{2}}(us\bar{u}\bar{s} + ds\bar{d}\bar{s}), \\
 I = 1/2 & \quad \rightarrow \quad \kappa^+ = udd\bar{s} \quad , \quad \kappa^0 = ud\bar{u}\bar{s} \quad , \quad \bar{\kappa}^0 = us\bar{u}\bar{d} \quad , \quad \kappa^- = ds\bar{u}\bar{d}, \quad (5.2) \\
 I = 1 & \quad \rightarrow \quad a_0^+ = us\bar{d}\bar{s} \quad , \quad a_0^0 = \frac{1}{\sqrt{2}}(us\bar{u}\bar{s} - ds\bar{d}\bar{s}) \quad , \quad a_0^- = ds\bar{u}\bar{s}.
 \end{aligned}$$

Within the interpretation as tetraquark states [29, 30, 31, 32] both the mass degeneracy of $f_0(980)$ and $a_0(980)$, and the mass ordering of the whole nonet, resolve rather naturally, cf. Figure 5.1. Furthermore are the larger widths of σ and κ easier to explain, since the decay channels to $\pi + \pi$ and $K + \pi$, respectively, are OZI allowed. Last to mention is experimentally known that $a_0(980)$ couples well to $K\bar{K}$, since its decay channel is sizeable although most of the phase space for $a_0 \rightarrow K\bar{K}$ is closed. The tetraquark structure allows a cheap decay into $K\bar{K}$, while $u\bar{d} \rightarrow K\bar{K}$ is suppressed by the creation of a $s\bar{s}$ pair.

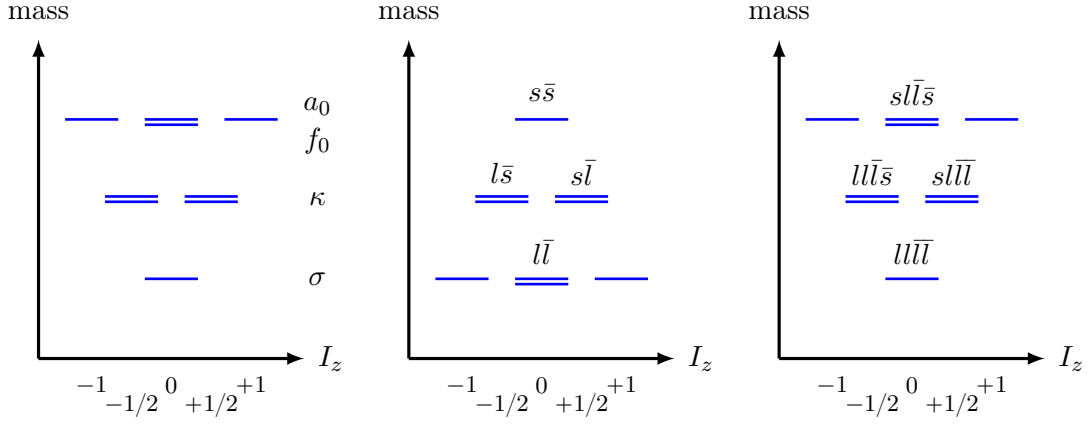


FIG. 5.1: Flavor structure and mass hierarchy for the spectrum of light scalar mesons ($J^P = 0^+$). Experimental observations (left), expectation based to the conventional $q\bar{q}$ model (center), interpretation as tetraquark states, i.e. $qq\bar{q}\bar{q}$ (right).

Several lattice QCD studies on light scalar mesons have been published in the last couple of years and the $a_0(980)$ has turned out to be a challenging task. Early quenched studies revolve around the differentiation whether the observed lattice state extrapolates to $a_0(980)$ or to its excitation $a_0(1400)$ [101, 102, 103]. Once the state on the lattice was mutually identified with an energy ~ 1 GeV (cf. [104] and references therein), its content still remained unclear. The near presence of two scattering states with similar energies complicates a clear extraction drastically. In contrast to the conventional quark-antiquark content stands a possible tetraquark interpretation. This quark setup also involves loop contributions that have to be taken into account, i.e. quark propagators with a starting and end point on a single timeslice. In absence of such contributions no indications of a tetraquark structure for the a_0 have been seen in [21, 100]. Altogether is

the identification of the internal structure of the a_0 difficult, but more recent results tend to a non-tetraquark structure [26, 28, 105]. It is important to mention the particular reference [106]. Therein the a_0 is investigated as a coupled channel scattering state for a first time, which we will comment on at the end of the thesis.

Results presented in this section are the continuation of the project [21, 22, 23], where Wilson twisted mass fermions are employed. The continuous progress of this work is documented in [24, 25, 26, 27, 28].

To set the stage for the analysis of a tetraquark candidate we need to identify the infinite volume two-particle levels first. They differ from the finite volume two-particle levels by finite size interactions [16, 17]. Following the standard procedure (3.18) we compute single diagonal correlators from operator structures $O \simeq (\bar{\psi}^{(f_1)}\gamma_5\psi^{(f_2)})$ to obtain the pseudoscalar mesons π , K , and η_s within our lattice setup. To fit the pseudoscalar mass of the unphysical η_s state we neglect fully disconnected pieces of the correlator. Their involvement reduces the possible range for a fit to the effective mass to only a few noisy points, which are within errors in agreement to the connected-only signal. Figure 5.2 shows the results for the pseudoscalar masses in lattice units and the corresponding GeV. The infinite volume two-particle levels are calculated at $am_{\eta_s+\pi} = 0.502(1)$ and $am_{K+\bar{K}} = 0.548(4)$, and are represented by dashed lines. This corresponds to an energy range of ≈ 1.1 - 1.2 GeV for the anticipated $a_0(980)$ candidate within our setup with $m_\pi \approx 300$ MeV.

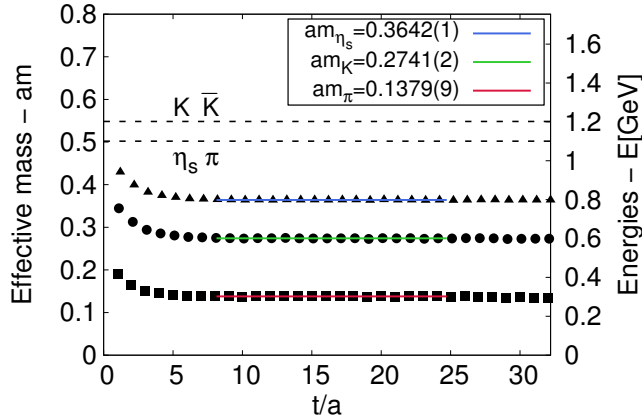


FIG. 5.2: Identification of pseudoscalar mesons π , K and η_s within our lattice setup. Infinite volume two-particle levels $\eta_s + \pi$ and $K + \bar{K}$ are calculated from single particle results.

The following two sections aim to observe an $a_0(980)$ candidate in our setup by application of various two-quark and four-quark creation operator sets (3.19). We split the discussion of results into two scenarios: At first we neglect all diagrams that involve quark propagators with a starting and end point on a single timeslice. This effectively breaks our 6×6 correlation matrix, cf. Figure 3.3 and 3.4, into two independent 1×1 and 5×5 problems. Afterwards we consider all contributing diagrams and study the resulting matrix and submatrices anew.

5.1.1 Omitting quark loop contributions

The 1×1 problem

Studying the single diagonal correlator C_{11} with $O^1 = O^{q\bar{q}} \simeq (\bar{d}u)$ corresponds naïvely to a simple 1×1 problem. However, the extraction of scalar states by $q\bar{q}$ operators remains a challenge to lattice computations. The major problem is that these states are usually scattering states of two pseudoscalar mesons and that a naïve quark-antiquark interpretation might not be well suited to describe the channel. This problematic single scalar channel motivated the transition from an initial setup with twisted mass fermions [21, 22, 23] and an explicitly broken parity symmetry, to the now employed clover improved Wilson fermion action. Figure 5.3 shows the result for this channel, obtained by identical methods and the same set of statistics as the just presented pseudoscalar mesons, cf. Figure 5.2.

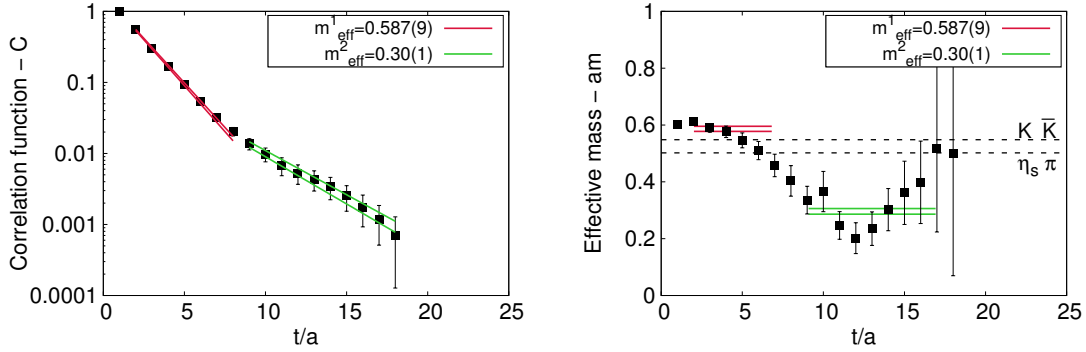


FIG. 5.3: Correlation function C_{11} (left) with $O^1 \simeq (\bar{d}u)$ and the corresponding effective mass (right), extracted by assuming contributions from a single exponential.

The signal of the correlation function is drastically worse compared to the pseudoscalar states and shows an apparent change in the slope around $t/a = 8$. This is emphasized by two independent single exponential fits $\propto A^{(n)} \exp(-m^{(n)} t)$ at different temporal separations.

At small temporal separations a plateau $am^{(1)} = 0.587(9)$ above both two-particle levels is found. In this region higher energy eigenstates contribute to the correlator, such that a larger energy is expected. Thereafter the signal fails to converge to a clear ground state in the two-particle region, but further decreases for increasing temporal separations. At larger temporal separations a satisfying fit becomes impossible, due to drastically increasing noise. Depending on the range of the fit one can estimate a slope of the correlation function around $am^{(2)} = 0.30(1)$.

It is important to note that what appears to be a lower energy level does not correspond to an energy eigenstate. The reason for this behavior are two particles created by the operator at t_1 that are propagating in opposite directions around the torus to t_2 . This particular contribution is suppressed by the finite temporal extent of the lattice,

but also leads to the impression of another light state. In the following we refer to these effects of particles propagating in opposite directions as artificially light signals, as they are governed by the mass difference of the two particles, cf. (3.7). Although artificially light signals are treated like energy contributions to the correlator, they are not energy eigenstates, but finite size effects. In Figure 5.4 different signals to a correlation function of two particles are illustrated.

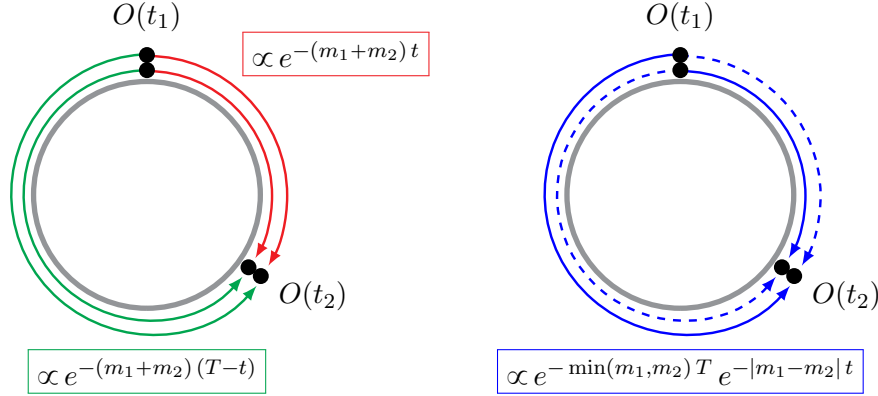


FIG. 5.4: Two particle propagation around the torus with $t = t_2 - t_1$ and $t_2 > t_1$. Joint propagation analogous to a single particle (left) and propagation in opposite directions (right). Two scenarios of particles propagating in opposite directions are distinguished by solid and dashed lines. To consider all three contributions to a correlation function (red, green, blue) effective masses have to be extracted accordingly.

A simple log-fitting scheme to a correlator is strictly speaking only valid far from any boundary of the lattice. To account for the finite temporal extent of the lattice, more sophisticated strategies are required.

The issue is certainly relevant for the a_0 due to the neighboring $\eta_s\pi$ and $K\bar{K}$ states. What we expect are time dependent contributions from an artificially light signal $am_{\text{art}}^{(\eta_s-\pi)} = 0.226(1)$ and constant contaminations from the $K\bar{K}$ channel, due to particles of equal mass. To obtain an estimate of the leading artificial signal we fit a sum of two exponentials $\propto A^{(1)} \exp(-m^{(1)}t) + A^{(2)} \exp(-m_{\text{art}}^{(2)}t)$ to the correlator C_{11} .

Fitting both contributions simultaneously increases the splitting of the signals towards $am^1 = 0.65(1)$ [previously: $am^1 = 0.587(9)$] and $am_{\text{art}}^2 = 0.23(1)$ [previously: $am^2 = 0.30(1)$]. This shows that in the presence of sizeable finite volume effects energy contributions at small temporal separations are underestimated in the naïve log fitting scheme. Furthermore is an artificial signal around $0.23(1)$ inverse lattice units a sound indication for the finite size effect of an $\eta_s\pi$ signal propagating in opposite directions, where $am_{\text{art}}^{(\eta_s-\pi)} = 0.226(1)$.

It is clear that from this correlator alone an extraction of any possible a_0 candidate is problematic. One might assume a plateau at small temporal separations, yet without resolution of neighboring states this is a questionable assumption.

The 5×5 problem

In the following we want to study the 5×5 correlation matrix $C_{ij} = \langle O_i O_j \rangle$ with $i, j \in [2, \dots, 6]$, referring to the notation of (3.19). For now we neglect $2 \times$ connected contributions to all correlators, which corresponds to prohibiting quark loop contributions. We hence expect states around and above the two-particle thresholds as lighter states are inaccessible. In particular we are interested in whether the molecule-like interpolators $O^2 = O^{K\bar{K}, \text{point}}$ and $O^3 = O^{\eta_s \pi, \text{point}}$ or the diquark-antidiquark interpolator $O^4 = O^{Q\bar{Q}}$ succeed in observing a candidate for the $a_0(980)$, i.e. resolve a third low-lying state near the expected two-particle levels.

At first we analyze the 2×2 and 4×4 submatrices corresponding to the $\eta_s \pi$, $K\bar{K}$ point and point+two-particle operator sets, i.e. $[O^{K\bar{K}, \text{point}}, O^{\eta_s \pi, \text{point}}]$ and $[O^{K\bar{K}, \text{point}}, O^{\eta_s \pi, \text{point}}, O^{K\bar{K}, 2\text{part}}, O^{\eta_s \pi, 2\text{part}}]$, respectively. Results obtained from solving the GEP are shown in Figure 5.5.

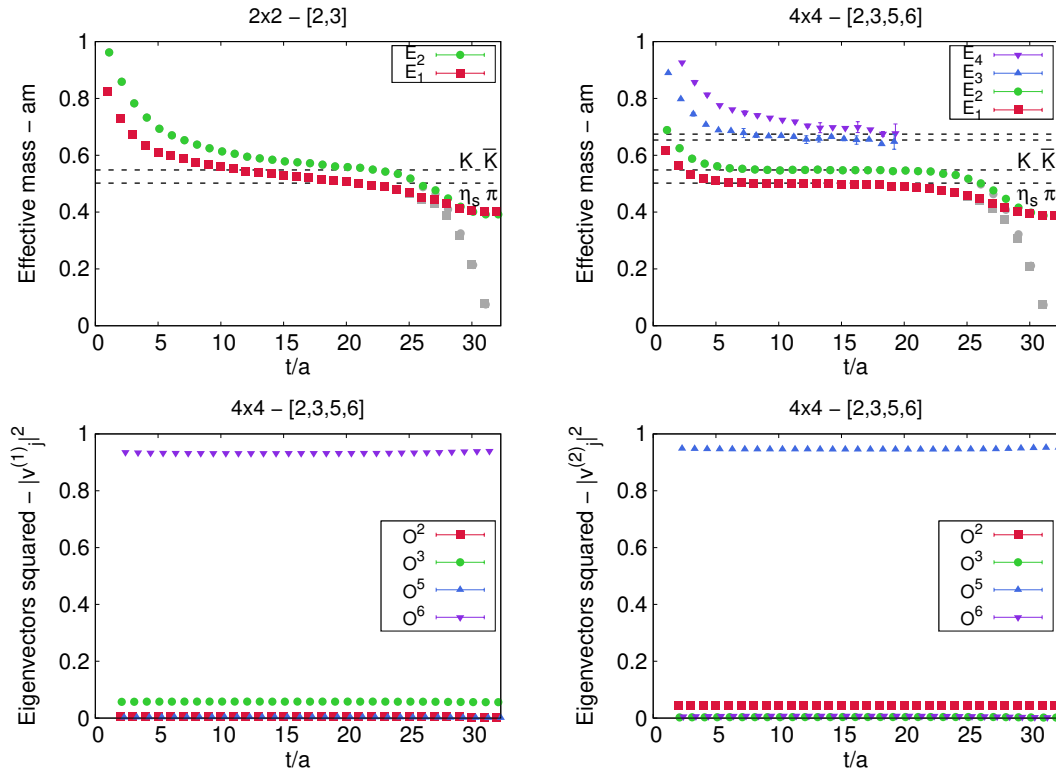


FIG. 5.5: GEP analysis of the correlation matrix omitting quark loop contributions. Analysis of the 2×2 problem with $[O^2, O^3]$ (top left) compared to the 4×4 problem with $[O^2, O^3, O^5, O^6]$ (top right). Squared eigenvector components corresponding to E_1 and E_2 of the 4×4 analysis are given on the (bottom left) and (bottom right), respectively. Dashed lines refer to the infinite volume two-particle levels. Gray and colored points refer to different fitting schemes.

It can be seen that the molecule-like operators alone provide a certain overlap with the two-particle levels, cf. Figure 5.5 top left. In comparison with the two-particle

operators this overlap is, however, largely composed of excited state contributions. The signals converge only slowly towards the infinite volume two-particle levels and do not reach a plateau. The two-particle operators excel in regard of resolving the two-particle energies, cf. Figure 5.5 top right, which is why such operators are very important to compute for studies of possible tetraquark candidates. They reach a plateau, but at large temporal separations decrease to what appears to be lower energies.

In the top row of Figure 5.5 gray points indicate an effective mass extracted from the eigenvalues by a simple $\log(\dots)$, while colored points take the periodicity of the lattice into account and energies are extracted by a $\cosh(\dots)$. Both strategies show a distinct behavior towards the center of the lattice that do not coincide with the infinite volume two-particle levels. It is thus clear that additional effects must contribute to the correlators. Similar to the case of C_{11} with $O^1 = O^{q\bar{q}}$, we expect particles propagating in opposite directions around the torus.

Contrary to the 1×1 study of $O^1 = O^{q\bar{q}}$ we observe contaminating finite size effects only at large temporal separations $t/a \gtrsim 20$. Previously, these effects were already observed at small temporal separations $t/a \gtrsim 8$. Since the correlators cover the whole temporal extent of the lattice and show only small statistical errors, we are able to analyze the artificially light contributions precisely. We modify our fitting procedure (3.12) to not only account for the periodicity of the lattice, but also to include finite volume effects of two-particle states propagating in opposite directions. Therefore, we assume contributions to correlators following (3.7)

$$\begin{aligned}
C(t) &\simeq A \left(\underbrace{e^{-Et}}_{\text{red}} + \underbrace{e^{-E(T-t)}}_{\text{green}} \right) + B \left(\underbrace{e^{-m_1 t} e^{-m_2 (T-t)}}_{\text{blue}} + \underbrace{e^{-m_1 (T-t)} e^{-m_2 t}}_{\text{dashed blue}} \right), \\
&\simeq A e^{-ET/2} \left(e^{-E(t+T/2)} + e^{-E(t-T/2)} \right) \\
&\quad + B e^{-(m_1+m_2)T/2} \left(e^{(m_1-m_2)T/2} e^{-(m_1-m_2)t} + e^{(m_2-m_1)T/2} e^{-(m_2-m_1)t} \right), \\
&\simeq A e^{-ET/2} 2 \cosh(-E(t-T/2)) + B e^{-ET/2} 2 \cosh((m_1-m_2)(t-T/2)),
\end{aligned} \tag{5.3}$$

where $E = m_1 + m_2$ and underlined contributions are colored to match with the illustration in Figure 5.4. Consequently, after solving the generalized eigenvalue problem, effective masses $m_{\text{eff}}^{(k)}$ can be extracted from subsequent eigenvalues $\lambda^{(k)}$ according to

$$\frac{\lambda^{(k)}(t, t_r) - C \cosh\left(a m_{\text{art}}^{(k)}(t - T/2)\right)}{\lambda^{(k)}(t + a, t_r) - C \cosh\left(a m_{\text{art}}^{(k)}(t + a - T/2)\right)} = \frac{\cosh\left(a m_{\text{eff}}^{(k)}(t)(t - T/2)\right)}{\cosh\left(a m_{\text{eff}}^{(k)}(t)(t + a - T/2)\right)}, \tag{5.4}$$

where $m_{\text{art}}^{(k)}$ is the leading artificial signal contributing to the (k) -th eigenvalue and C is a constant proportional to $\propto e^{-T}$.

The single leading finite size effect to each eigenvalue is difficult to determine precisely. By *guessing* contributions corresponding to the respective two particles of the channel, we observe restored behaviors for the effective masses. In particular, these artificial signals $m_{\text{art}}^{(k)}$ correspond in the $K\bar{K}$ and $\eta_s\pi$ channel to $m_{\text{art}}^{K\bar{K}}$ and $m_{\text{art}}^{\eta_s\pi}$, respectively. Inserting signals following $am_{\text{art}}^{K\bar{K}} \rightarrow am_{\text{art}}^{(K-\bar{K})} \approx 0$ and $am_{\text{art}}^{\eta_s\pi} \rightarrow am_{\text{art}}^{(\eta_s-\pi)} \approx 0.226$ both groundstates coincide with the infinite volume two-particle levels, cf. Figure 5.6.

Figure 5.6 shows three different effective masses for the two-particle signals, obtained by applying different fitting procedures. Again, colors emphasize which contributions of two particles on the torus are considered, referring to Figure 5.4. Based on the same two-particle correlation functions (represented by circles and squares) only a fitting scheme following (5.4) provides an effective mass close to the infinite volume two-particle levels.

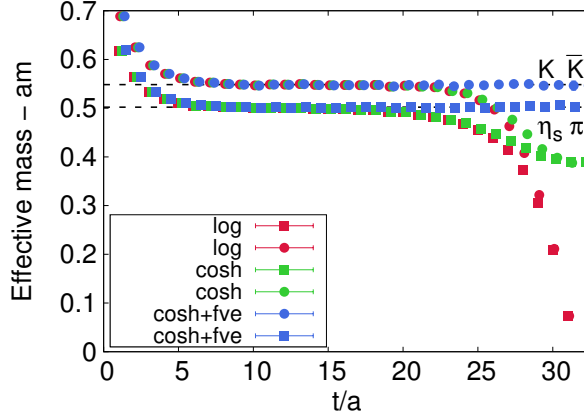


FIG. 5.6: Effective masses extracted from different fitting schemes to the eigenvalues. A simple exponential $\lambda \propto \log(\dots)$ [red], including the periodicity of the lattice $\lambda \propto \cosh(\dots)$ [green] and considering the periodicity + finite volume effects $\lambda \propto \cosh(\dots) + \text{fve}$ [blue]. Squares and circles correspond to $\eta_s \pi$ and $K \bar{K}$ states, respectively.

Thus we confidently confirm two particles propagating around the lattice in opposite directions as leading, artificially light, contribution to the correlators.

Above the groundstate two-particle levels we observe additional states in the top right of Figure 5.5. These states are found around $\approx 0.65 - 0.67$ inverse lattice units, which coincides with the expected first momentum excitations of the two-particle energies, i.e.

$$\begin{aligned} aE_{\eta_s}(1) + aE_{\pi}(-1) &= \sqrt{am_{\eta_s}^2 + (2\pi/L)^2} + \sqrt{am_{\pi}^2 + (2\pi/L)^2} \approx 0.65, \\ aE_K(1) + aE_{\bar{K}}(-1) &= \sqrt{am_K^2 + (2\pi/L)^2} \approx 0.67. \end{aligned}$$

Note that the upper two dashed lines in Figure 5.5 correspond to the infinite volume two particle levels with a momentum excitation. Both these states are dominated by a mixture of the two point operators $O^2 = O^{K\bar{K}, \text{point}}$ and $O^3 = O^{\eta_s \pi, \text{point}}$. Hence, we do not observe a third low-lying state of a possible molecule-like structure from investigating this set of four operators.

Eventually, after including also diquark-antidiquark operators, we analyze the complete set of operators. Figure 5.7 shows the observed states from this set. The inclusion of diquark-antidiquark interpolating field operators does not resolve a third low lying state around the two particle thresholds either. Instead, additional excited states are indicated.

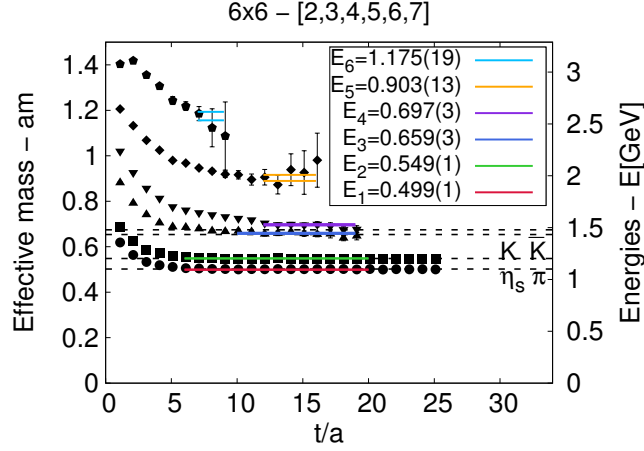


FIG. 5.7: GEP analysis for the full correlation matrix, neglecting quark loop contributions. The two low-lying states correspond to the expected two particle levels, followed by first momentum excitations. Diquark-antidiquark structures without loop contributions do not resolve a third low-lying state.

This conclusion is in agreement with previous studies [21, 100], where no additional state has been seen which could be interpreted as an a_0 candidate, by using four-quark interpolators with absent loop contributions. The following section will include these contributions to the correlators of the matrix and study the effects of these changes on several GEP analyses with varying operator sets.

5.1.2 Including quark loop contributions

The upcoming analysis including $2\times$ connected diagrams is restricted to a maximum amount of $N_{\Delta t} = 15$ temporal separations. From the analysis of a matrix consisting only of $4\times$ connected diagrams we expect that finite size contributions will affect our channels for $t/a \gtrsim 20$, making this a well-suited temporal range.

Although the study of a matrix composed of only $4\times$ connected diagrams is contaminated at large temporal separations its analysis is very well feasible. The inclusion of $2\times$ connected diagrams drastically worsens the circumstances. This can already be seen by looking at and comparing the diagonal elements of both matrices, plotted in Figure 5.8.

On the left side the diagonal correlation functions of the $4\times$ connected-only matrix split up at small separations, due to different excited state contributions. They continue to decay approximately in parallel, implying their ability to resolve *one* particular energy range, i.e. the range of interest $\sim 1.1 - 1.2$ GeV. As discussed earlier, this range is around $0.55a^{-1}$, the approximate energy of an $a_0(980)$ candidate within our lattice setup. Plotted by black squares is the $O^1 = O^{q\bar{q}}$ correlator C_{11} , which shows a distinct behavior and loses its ability to resolve the energy range of interest due to finite size effects for $t/a \gtrsim 8$.

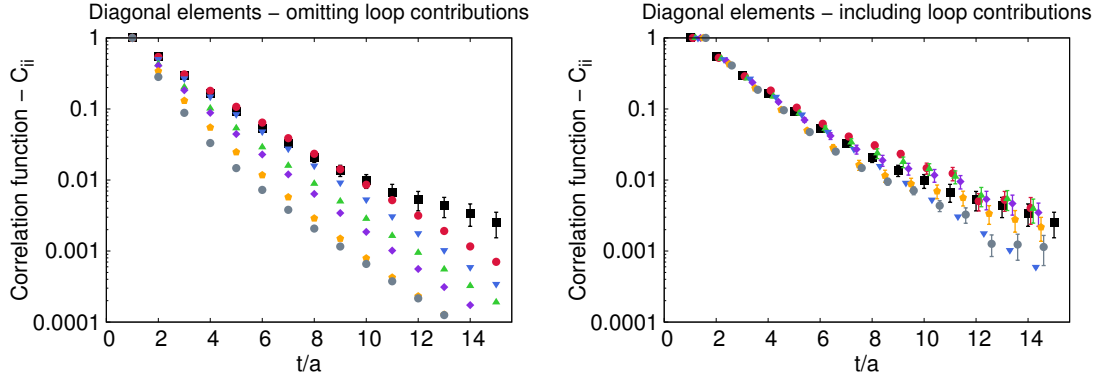


FIG. 5.8: Diagonal elements of correlation matrices omitting $2\times$ connected diagrams (left) and including $2\times$ connected diagrams (right). Off-diagonal elements are not considered. Black squares on both sides refer to C_{11} . On the left side only C_{11} is noticeably affected by finite size effects. On the right every element appears to be affected to a certain extent by the same effect.

On the right side the diagonal correlation functions of the full analysis is shown, i.e. considering both $4\times$ and $2\times$ connected contributions, but omitting off-diagonal matrix elements. The contaminated C_{11} correlation function is again plotted with black squares. What has previously been an exceptional bad behavior of a single channel is now observed in nearly every on-diagonal element of the full correlation matrix. Similar behaviors are observed in the off-diagonal elements as well.

An exception is the C_{55} correlation function with $O^5 = O^{K\bar{K}, 2\text{part}}$ plotted by blue triangles. There the $2\times$ connected diagram contributes only little to the total correlator, leaving the impact of the $4\times$ connected contribution nearly unchanged, cf. Figure 4.20. An explanation for this behavior can be found in the physical implications of this particular diagram type. There the antistrange and strange quark of a dynamical $K\text{-}\bar{K}$ pair annihilate. One would expect that this process is largely suppressed, due to the spatial separation of the two mesons.

With diagonal correlators following the trend of C_{11} one expects that these are also affected by sizeable contributions from finite size effects. Figure 5.9 presents for an example on the left the plain $4\times$ and $2\times$ connected correlation functions, that added together make the full C_{22} element. On the right a comparison between the $2\times$ connected correlation function of C_{22} with C_{11} is shown.

On the left a double exponential fit through the $2\times$ connected correlator emphasizes contributions from an artificially light signal. Far from the boundary of the lattice this fit corresponds to

$$C(t) \simeq A e^{-m t} + B e^{-m_{\text{art}} t}, \quad (5.5)$$

where m is an energy eigenstate and m_{art} a light signal from particles propagating around the torus. B is much smaller than A , as it is suppressed by the finite temporal extent of the lattice, i.e. $\propto e^{-T}$.

On the right it can be seen that the trend of this particular $2\times$ connected diagram follows very much the behavior of the C_{11} element, for which we observe evidence for contributions from particles propagating around the torus. Such a kink in the correlator

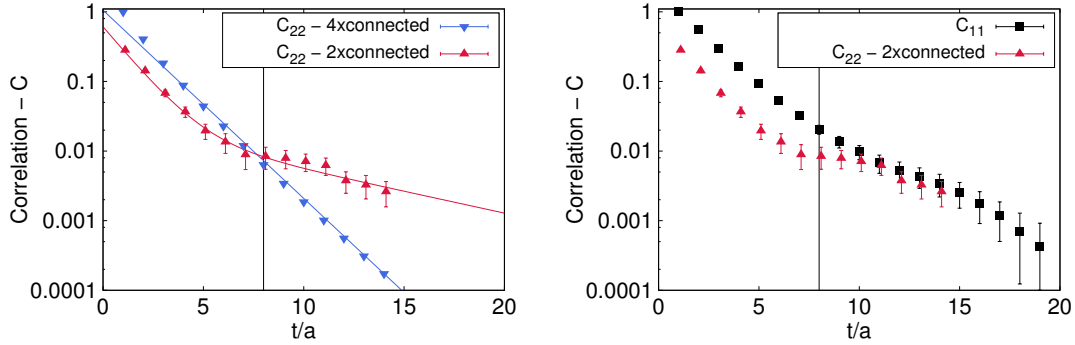


FIG. 5.9: Decay of the $4\times$ and $2\times$ connected contributions of C_{22} (left) and a comparison of the $2\times$ connected diagram of C_{22} with C_{11} (right). Fits on the left correspond to single and double exponentials to emphasize distinct characteristics. The vertical bar at $t/a = 8$ suggests the end of trustworthy analyses.

is visible also for other elements of the matrix, after including quark loop contributions, which implies sizeable finite size effects for all these elements as well.

However, the number of temporal separations $N_{\Delta t}$ of the $2\times$ connected diagrams is not large enough and statistical fluctuations are too large to obtain precise insights on all these contributions in particular. Thus we are not able to identify the characteristic finite size contributions of every $2\times$ connected diagram. To do so one would need to compute much more temporal separations, possibly include multiple contaminating states to the fitting procedures and increase the overall statistics of measurements to guarantee reliable precision of the data. Only then a precise identification of contaminating finite size contributions becomes possible, allowing an extraction of energy eigenstates at larger temporal separations.

We have seen that finite size contributions from two particles propagating around the torus in opposite directions are contaminating the $2\times$ connected correlation functions. Consequently our analysis of an a_0 candidate will be limited to small temporal separations. In the following we pursue with the analysis of energy eigenstates from solving the generalized eigenvalue problem.

We analyze the full matrix analogous to the previous $4 \times$ connected-only matrix, cf. Figure 5.5. In Figure 5.10 we present the GEP results of the 2×2 and 4×4 submatrices corresponding to the $\eta_s \pi$, $K \bar{K}$ point and point+two-particle sets, i.e. $[O^{K\bar{K}, \text{point}}, O^{\eta_s \pi, \text{point}}]$ and $[O^{K\bar{K}, \text{point}}, O^{\eta_s \pi, \text{point}}, O^{K\bar{K}, 2\text{part}}, O^{\eta_s \pi, 2\text{part}}]$ respectively.

Dashed lines correspond to the two particle levels calculated from correlation functions of pseudoscalar meson creation operators and do not include quark loop contributions. Their purpose is again to guide the eye and to set a range of where we expect to find an a_0 candidate. In the following, dashed horizontal lines will always refer to two-particle infinite volume levels.

It can be seen in the top left of Figure 5.10 that an analysis exclusively on the full molecule-like operators bears no information at all. Both signals decrease without regard of expected nearby energy levels towards what we identify to be the energy of an artificial signal around $am_{\text{art}}^{(\eta_s - \pi)} \approx 0.226$ inverse lattice units, cf. Figure 5.3. Just as before we find that the two-particle operators are essential to extract two-particle energy eigenstates from the GEP.

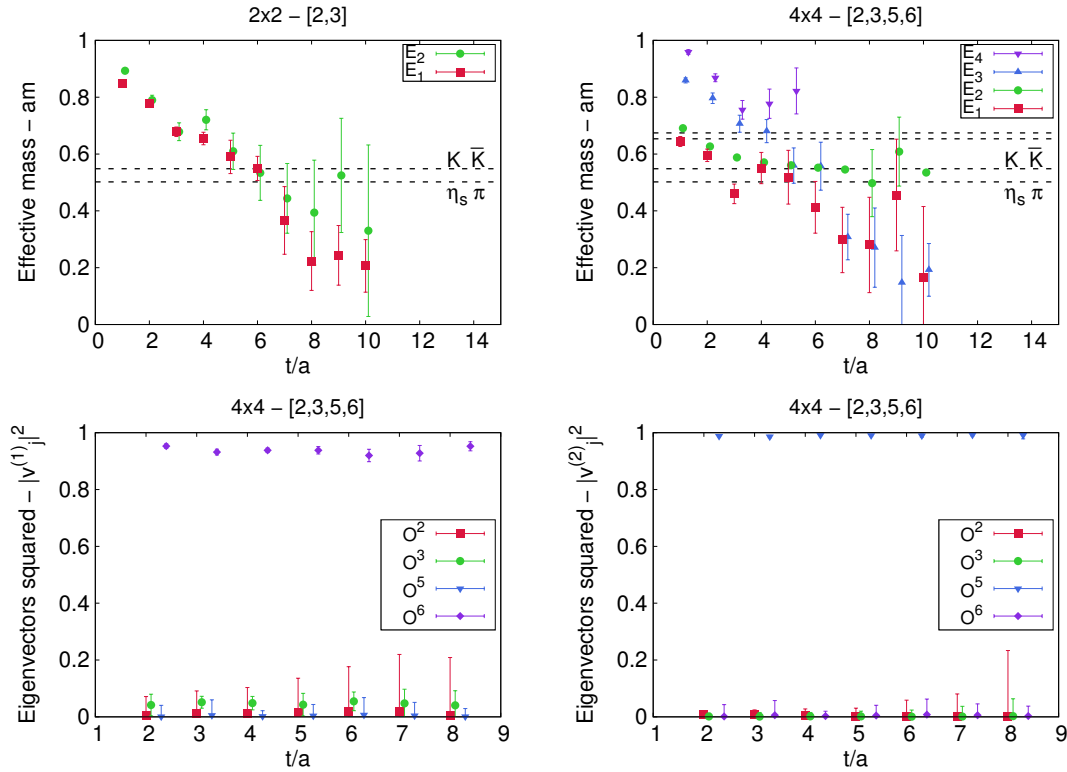


FIG. 5.10: GEP analysis of the full correlation matrix including all diagrams. Analysis of the 2×2 problem with $[O^2, O^3]$ (top left) compared to the 4×4 problem with $[O^2, O^3, O^5, O^6]$ (top right). Squared eigenvector components corresponding to E_1 and E_2 of the 4×4 analysis are given on the (bottom left) and (bottom right) respectively. Dashed lines refer to the infinite volume two-particle thresholds, calculated from single diagonal pseudoscalars without fully disconnected contributions.

A GEP analysis considering also the two-particle operators is shown in the top right of Figure 5.10. The characteristic disconnected strange quark loops associated to $O^{\eta_s\pi, 2\text{part}}$ contribute large noise fluctuations, as it can be seen by the effective mass plotted by red squares. Additionally, the channel shows an increased sensitivity towards an artificially light signal $m_{\text{art}}^{(\eta_s-\pi)}$. Hence, we can expect that the true $\eta_s\pi$ state is of higher energy than seen, since effective masses of Figure 5.10 are obtained by assuming a simple $\log(\dots)$ to the eigenvalues. This fitting procedure does not account for sizeable finite size effects, pulling the analysis to lower energies at small temporal separations. This observation has been made previously, while investigating the single C_{11} correlator, cf. Figure 5.3.

With only little contributions from quark loops provides $O^{K\bar{K}, 2\text{part}}$ a reasonable overlap to a $K\bar{K}$ groundstate. The corresponding effective mass is plotted by green circles and shows only small statistical fluctuations. This characteristic can be observed throughout our studies and makes it relatively easy to identify the respective energy level.

Excited states are created by the two point interpolators $O^2 = O^{K\bar{K}, \text{point}}$ and $O^3 = O^{\eta_s\pi, \text{point}}$ and remain to show contributions from finite size effects, already at small temporal separations. This leads to the observation of eigenvalues falling through energy levels down into the energy range of the expected finite volume effects, cf. the blue triangles on the top right of Figure 5.10. Although the signal coincides with nearby energy levels at some temporal separations it is no indication of an additionally energy level to those already resolved.

These contributions from finite size effects to the signals of the operators $O^{K\bar{K}, \text{point}}$ and $O^{\eta_s\pi, \text{point}}$, reduce the signal from first momentum excitations of $\eta_s\pi$ and $K\bar{K}$ largely. We are hence forced to extract the respective momentum levels from relatively short plateaus, indicating possible states in the best case. However, the splitting between the two resting two-particles and their first momentum excitation is relatively large for this particularly light tetraquark candidate. A possibly third low-lying state might hence still be very well distinguishable from these levels.

To check for an additional state close to the two-particle levels we include the remaining operators of diquark-antidiquark structure $O^4 = O^{Q\bar{Q}}$ and quark-antiquark structure $O^1 = O^{q\bar{q}}$. In a first step we want to do this by including them separately after one another to the already analyzed set [2, 3, 5, 6], corresponding to $[O^{K\bar{K}, \text{point}}, O^{\eta_s\pi, \text{point}}, O^{K\bar{K}, 2\text{part}}, O^{\eta_s\pi, 2\text{part}}]$. The results¹ of the GEP analyses are shown in Figure 5.11.

¹Colors of different effective masses do not imply an overlap to certain states.

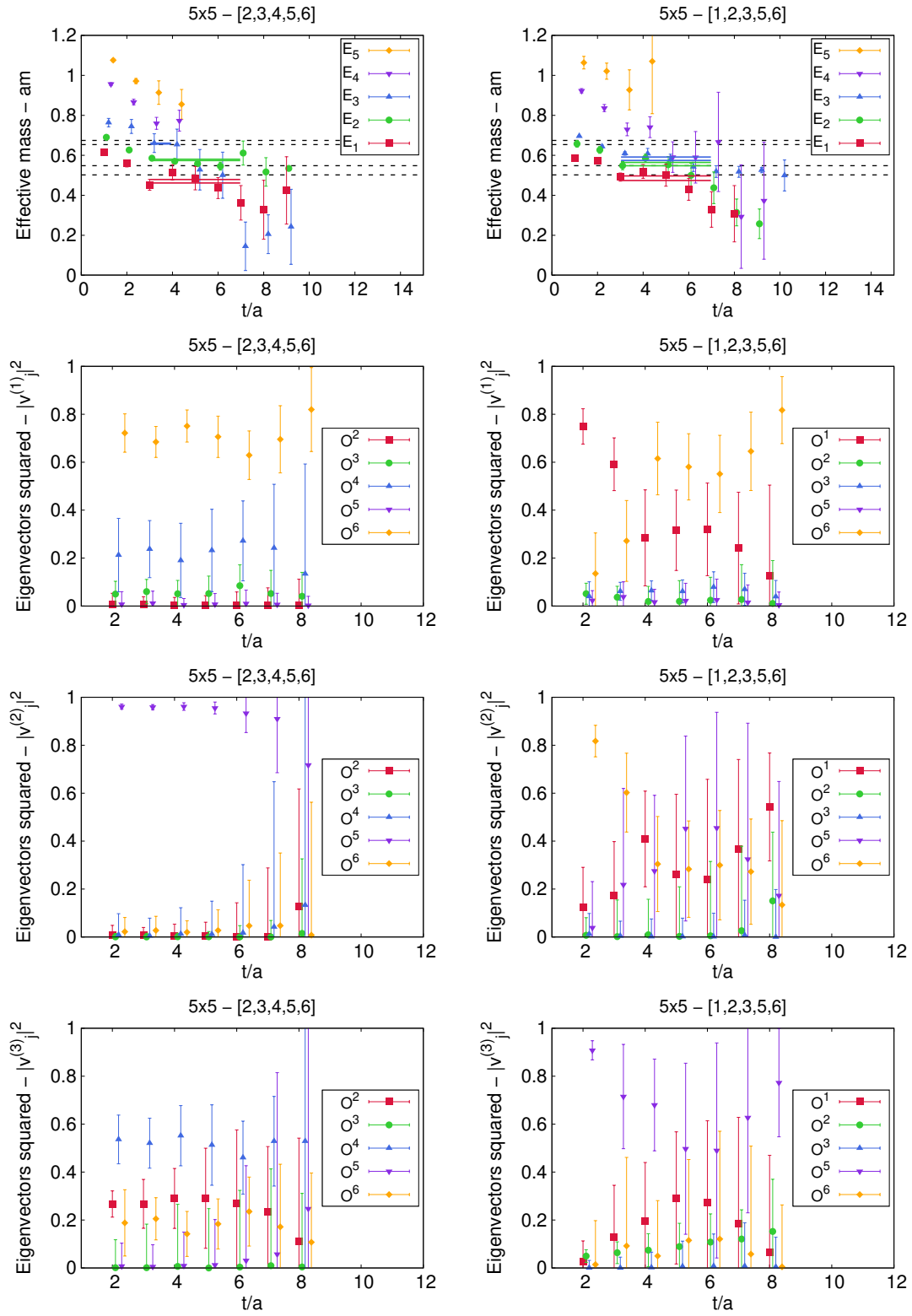


FIG. 5.11: GEP analyses of the full correlation matrix for the sets $[2, 3, 4, 5, 6]$ (left column) and $[1, 2, 3, 5, 6]$ (right column). In the top row effective masses are shown, followed by squared eigenvector components of the lowest three energy states.

In the left column energy levels of the operator set [2, 3, 4, 5, 6] and eigenvector components of the three lowest energies are shown. Qualitatively we observe in this column only minor alterations to the previously studied set [2, 3, 5, 6], which does not include a diquark-antidiquark operator. The signal of the lowest energy E_1 , plotted by red squares, has improved through contributions from the additional operator. E_2 , plotted by green circles, is still dominated by $O^{K\bar{K}, 2\text{part}}$, which is seen in the respective eigenvector, but also in a plateau that is seemingly unaffected by finite size effects.

Excited states still fall through the relevant energy range into an artificially light energy range around $\approx 0.22 a^{-1}$ or are quickly lost in statistical noise. It can be seen that $O^4 = O^{Q\bar{Q}}$ plays a dominant role in resolving the first momentum excitation. This is due to the fact that the overlap to this state with relative momentum is still sizeable and that explicit operators for momentum excitations are not included in our set of operators. While falling through the energy range of interest into the artificially light range, O^4 appears to indicate a third energy level in this region at two temporal separations. It is important to note that this is not to be understood as an indication for a possible tetraquark state at the respective energy. The signal merely indicates nearby energy levels, not excluding those which are already resolved. We include fits to the eigenvalues in appropriate ranges, which for the first momentum excitation often corresponds to just two points.

In the right column we plot energy levels of the set [1, 2, 3, 5, 6] and eigenvector components of the three lowest energies. In contrast to previous analyses without $O^1 = O^{q\bar{q}}$ we observe for a first time an additional third low-lying states between the two two-particle levels. This additional state E_2 is plotted by green circles and in the respective fitting range it is squeezed just below the $K\bar{K}$ state E_3 , pushing it to a higher energy than previously observed. It is worth mentioning that this energy is still significantly below the first momentum excitation and should not be interpreted as such. For $t/a \gtrsim 7$ the effective mass corresponding to state E_2 drops towards the range of artificially light signals, allowing E_3 to reach smaller energies again.

Table 5.1 collects the results of the fits to the eigenvalues of the GEP leading to the identification of two and three energy eigenstates. It can be seen that the energies corresponding to the two-particle levels are in agreement between the two operator sets, while only the inclusion of a $q\bar{q}$ structure leads to the observation of a third low-lying state.

	[2, 3, 4, 5, 6]	[1, 2, 3, 5, 6]
$[t_{\min}/a : t_{\max}/a]$	[3 : 8]	
$aE^{K\bar{K}}$	0.577(3)	0.583(8)
aE^{a_0}		0.556(8)
$aE^{\eta_s\pi}$	0.470(9)	0.486(12)

TAB. 5.1: Energy eigenstates in the region of interest extracted after solving the generalized eigenvalue problem for two different operator sets. States are obtained from the eigenvalues within the same frame of temporal separations. Agreement between the states corresponding to the two-particle levels is seen in addition to a third low-lying state of $q\bar{q}$ structure.

Comparing the eigenvectors of the lowest states with each other it can be seen that the composition evidently changes. In the left column of Figure 5.11 the lowest two energy levels are dominated by $O^6 = O^{\eta_s\pi, 2\text{part}}$ and $O^5 = O^{K\bar{K}, 2\text{part}}$, respectively. On the right the dominant contributions of these operators are seen in the eigenvectors corresponding to the states E_1 and E_3 . In the range of temporal separations where E_2 is extracted its signal is governed by the operators of the two neighboring energy levels, $O^5 = O^{K\bar{K}, 2\text{part}}$ and $O^6 = O^{\eta_s\pi, 2\text{part}}$, as well as the conventional quark-antiquark operator $O^1 = O^{q\bar{q}}$.

The overlap to the $K\bar{K}$ operator can be understood through the close proximity of the two states, where the third low-lying state is pushing the $K\bar{K}$ signal towards higher energies. The strong connection to the $\eta_s\pi$ operator can be motivated through similar finite size contributions, i.e. $\eta_s - \pi$. In preceding studies we have seen that both $O^1 = O^{q\bar{q}}$ and $O^6 = O^{\eta_s\pi, 2\text{part}}$ show sizeable contributions from this artificial signal. Moreover, we also find sizeable contributions of O^1 in the eigenvectors of the two two-particle states. It can be assumed that with higher statistics the mixture of these states will reduce, providing a much better indication of the actual quark structures of the states.

Most importantly is the strong condition of a quark-antiquark operator in the operator set to resolve this third low-lying state. This condition is interpreted as a sound implication for a conventional quark-antiquark structure of this state and not a four-quark structure, although a sizeable overlap to the two-particle operators is seen in its eigenvector. For an increased statistics it can be expected that the diagonalization of GEP will further improve, allowing a clearer identification of the additional state as $q\bar{q}$.

It is further important to note, that due to finite size contributions to the signal of the quark-antiquark operator the energy level of the third state is in the naïve $\log(\dots)$ underestimated as well. Similar to the $\eta_s\pi$ signal one would thus expect the $q\bar{q}$ state at higher energies than seen in Figure 5.1. Hence, it becomes difficult to predict this state below or above the $K\bar{K}$ level for future analyses with lighter pion masses.

Due to the strong condition of a present quark-antiquark structure in the operator set is the identification of the third low-lying plateau as an energy eigenstate only valid if O^1 is connected with the rest of the matrix. If this would not be the case, one would effectively study two independent problems, i.e. a 1×1 problem and a 5×5 problem of the remaining operator set. We have seen in Section 4.3 that the off-diagonal elements associated to the O^1 interpolator are indeed non-negligible.

To support the results of the generalized eigenvalue problem that indicate a third low-lying state, we also conduct an analysis utilizing the AMIAS method¹, cf. Section 3.2. By defining probability distribution functions (3.14) for the fit parameters, AMIAS applies Monte Carlo techniques to deal with a rather large number of fitting parameters, i.e. energies $\Delta\mathcal{E}_n$ and amplitudes c_n^j . An advantage to the GEP plateau regions or temporal fitting ranges are not necessary to define. Figure 5.12 shows at the top the probability distribution functions for energies $\Delta\mathcal{E}_i$ based on analysis of the 4×4 correlation matrix [2, 3, 5, 6] without quark loops and on the bottom [1, 2, 3, 4, 5, 6] including quark loops.

¹Analyses utilizing the AMIAS method have kindly been provided by Theodoros Leontiou, i.e. results shown in Figure 5.12 and Figure 5.13.

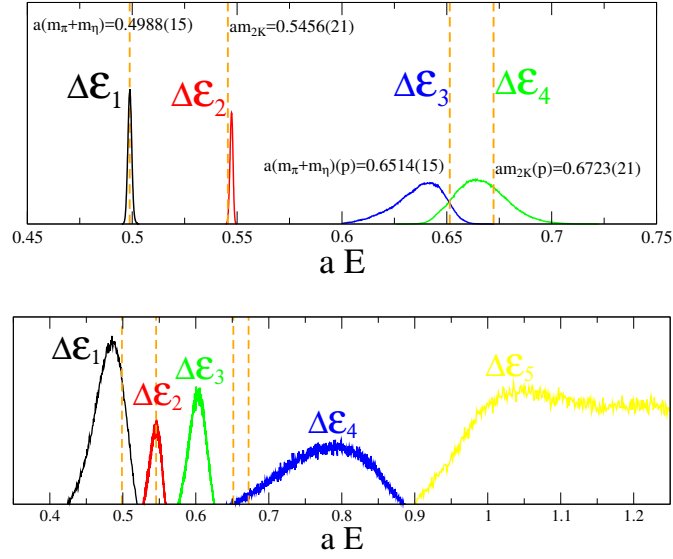


FIG. 5.12: AMIAS analyses of the operator set [2, 3, 5, 6] without considering quark loop contributions (top) and the operator set [1, 2, 3, 4, 5, 6] considering quark loop contributions (bottom).

Results shown in Figure 5.12 are in agreement with the findings of the GEP analyses, presented in the first row and second column of Figure 5.5 and Figure 5.11. Here it can be seen in the bottom plot, that the third additional state $\Delta\mathcal{E}_3$ is found above the $K\bar{K}$ state. A strong advantage of this method compared to the generalized eigenvalue is the freedom to omit particular matrix elements from the analysis. Hence, we can probe a system without element C_{11} to see whether the observed additional third low-lying state is in fact just a remnant of a weakly coupled O^1 operator. The observed probability distributions of energy states are shown in Figure 5.13.

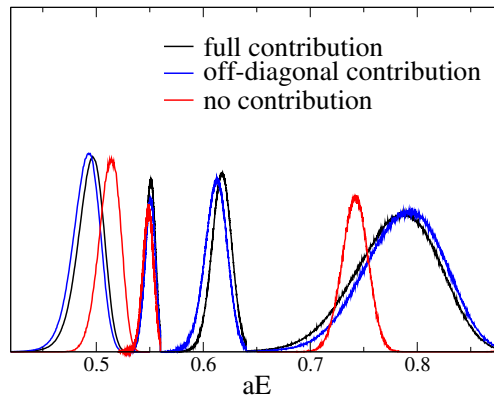


FIG. 5.13: Energy states obtained from correlation matrices including quark loops. The energies shown correspond to the full 6×6 problem (black line), the 5×5 problem omitting $q\bar{q}$ contributions (red line) and a problem with only off-diagonal $q\bar{q}$ contributions (blue line).

The agreement of the probability densities given in black and blue describing the present energy eigenstates of the full 6×6 analysis supports the conclusion of an additional low-lying state. Similar to the analysis with the GEP all three low-lying states are resolved below the first momentum excitations of the two-particle states. Note that in Figure 5.12 infinite volume two-particle levels are indicated by vertical dashed lines. The blue line demonstrates that the state is not obtained from the C_{11} element alone.

To conclude the analysis of the $a_0(980)$ candidate, we perform multiple GEP analyses of varying operator sets. The main objective is to confirm the existence of an additional state between the two-particle levels and to identify the major operators contributing to this state. In Figure 5.14 various energy levels from different operator sets are presented. Symbols and colors of energies are chosen to emphasize certain characteristics that indicate the structure of the states, derived from the eigenvectors of the states presented in Figure 5.15.

The lowest energy level found throughout our studies is presented by red squares and corresponds to an $\eta_s\pi$ state. After considering quark loop contributions to the matrix its energy is observed lower with regard to the infinite volume two-particle level. As we have seen before, this observation is linked to a finite size effect of two particles wrapping around the torus in opposite directions. This effect has sizeable contributions to the correlator similar to an artificially lighter state, contaminating the two-particle signal at small temporal separations. We are not able to include these contributions explicitly to our analysis and are forced to extract masses at relatively short temporal separations. Extracting the effective mass assuming a simple exponential behavior is hence underestimating the true energy of the two-particle signal, causing the shift from the infinite volume two-particle level, which is seen in Figure 5.14.

Plotted by green circles is the heavier two-particle level of the spectrum, a state corresponding to $K\bar{K}$. These states are throughout all studies dominated by the respective two-particle operator and have an exceptionally good signal. Contributions from $2\times$ connected diagrams to the correlator are almost negligible, so that finite size effects have no impact to the plateau at relevant temporal separations. In Figure 5.14 the states occur higher with regard to the infinite volume two-particle level. This is due to the fact that the shown mass plateaus are always extracted at relatively small temporal separations. The signal generally reaches also into larger temporal separations. To keep consistency with the lower $\eta_s\pi$ state we extract the energy within the same range of temporal separations. At such small separations we inevitably include also excited state contributions to the correlator when extracting the energy.

In blue triangles (pointing upwards) we plot the lowest energy level of a state close to the first momentum excitation of the two-particle states. Explicit momenta are not included in our operator set and therefore first momentum excitations are created by mixtures of operators with sizeable overlap to these state. These correlators are affected by artificially light signals and as a consequence fall into an energy range of artificially light signals around ≈ 0.22 inverse lattice units. At best, the extracted levels are an indication of the first momentum states. In the case of the light tetraquark candidate of interest the first momentum excitations are, however, well separated from the ground-state levels and do not threaten the analysis of the relevant energy range.

Plotted by violet triangles (pointing downwards) is a third low-lying state. We observe this state exclusively by including operator $O^1 = O^{q\bar{q}}$ to the set of operators, shown in the last four columns of Figure 5.14. It appears close to the $K\bar{K}$ level, with contributions from the two two-particle operators and the conventional quark-antiquark operator. Similar to the $\eta_s\pi$ state a signal is found only for a few small temporal separations before it drops towards a lower artificial signal.

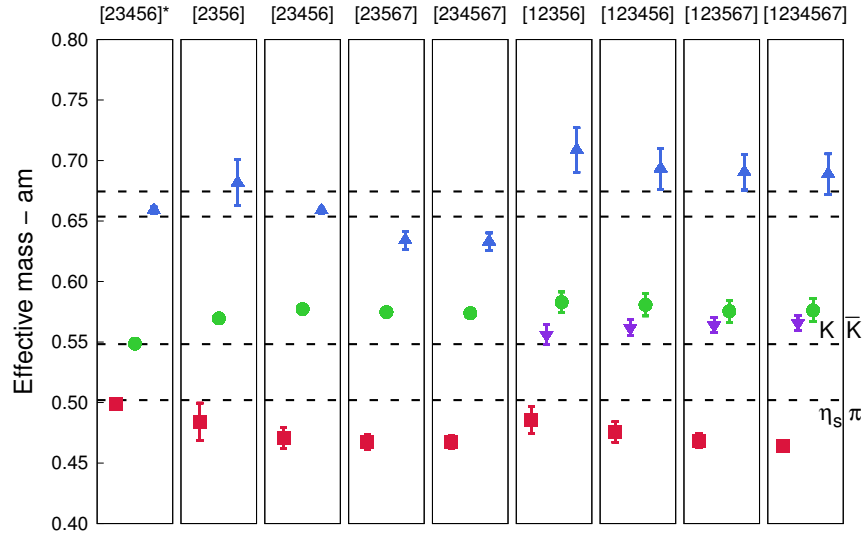


FIG. 5.14: Multiple energy levels from various GEP analyses. The title of each column refers to the operator set of each GEP. The asterisk on the first column indicates the absence of quark loop contributions from the analysis. Red and green symbols refer to states dominated by two-particle operators O^6 and O^5 respectively. Blue symbols represent the first state well-separated from the groundstate levels. Violet symbols correspond to a low lying state observed only in combination with O^1 .

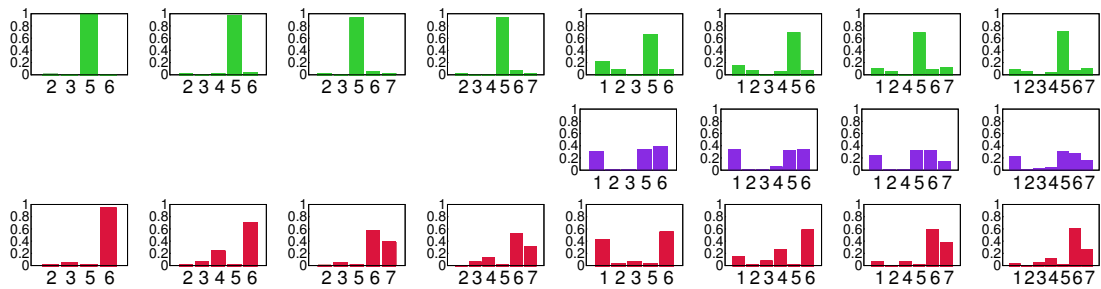


FIG. 5.15: Constants fitted to squared eigenvector components of the two and three lowest eigenvalues. The extracted effective masses from these eigenvalues are shown in Figure 5.14, matching colors refer to associated eigenvalues and eigenvectors. Operator sets are paired vertically, labels on the x-axis refer to the particular operator contribution to the eigenvalue.

In Figure 5.15 we show the squared eigenvector components of the two and three lowest states presented in Figure 5.14. Values are obtained by assuming constant contributions throughout the relevant temporal separations. The colors of eigenvectors are chosen to match between both figures. Errors to the fits are not provided as the purpose of this presentation is only to emphasize the characteristic operator composition of each state.

In this section we have seen that although the quality of the signals reduces drastically after quark loop contributions are included, the low energy range of light scalars can still be resolved at relatively small temporal separations. The two two-particle levels are shifted from their infinite volume levels due to finite volume effects and early plateau extractions, respectively. The addition of a quark-antiquark structure to the set of operators leads to a third state above the $\eta_s\pi$ level, close to the $K\bar{K}$ state. Finite size contributions to the signal complicate a localization of the state with respect to the $K\bar{K}$ level. This additional state couples to both two-particle operators, as well as the conventional $q\bar{q}$ creation operator. It can be assumed, given improved statistics, that the diagonalization of operators becomes much better, allowing a more distinct identification as a conventional $q\bar{q}$ state.

5.2 The heavy candidate: $D_{s_0}^*(2317)$

The heavy strange-charmed meson $D_{s_0}^*(2317)$ with $J^P = 0^+$ was expected by quark models above the DK threshold. However, experimental results [29] find a narrow state well below this threshold. These results in combination with a mass difference in $D_{s_0}^*(2317) - D_0^*(2400)$, which is too small to account for the s - u/d quark mass difference, have led to many possible interpretations. Hence, its internal structure is still under debate and ranges from conventional $\bar{c}s$ states [107, 108] to four-quark states [109, 110, 111, 112].

In [113] the $D_{s_0}^*(2317)$ and $D_{s_1}(2460)$ ($J^P = 1^+$) are referred to as “*charmed cousins of the light scalar nonet*”. There the coupling of the scalar $\bar{c}s$ to the DK threshold is suggested as a mechanism for a lighter mass as the physical state, in strong analogy to the light scalar nonet, i.e. the $a_0(980)$ just below the $K\bar{K}$ threshold, with a strong coupling to nearby channels .

Previous lattice studies [7, 81, 114, 115] calculate the mass of the $D_{s_0}^*(2317)$ using only quark-antiquark operators. The found energy levels have all been considerably above the DK threshold and interpretations do not include a definitive resolution of neighboring two-particle levels. Continuum extrapolations of these results show a sizeable difference in the energy in comparison to experimental results, possibly indicating a quark structure different from $q\bar{q}$.

In [116, 117] also DK and D^*K interpolating fields are employed in addition to $\bar{c}s$. The authors extract the phase shifts on two ensembles by an effective range approximation and obtain negative scattering lengths, supporting shallow bound states.

In our investigation of a $D_{s_0}^*(2317)$ candidate we utilize the same contraction code as in the previous study of the $a_0(980)$ but perform a change of the quark flavor basis

of interest according to

$$\{\bar{d}, u, \bar{s}, s\} \longrightarrow \{\bar{c}, s, \bar{u}, u\}.$$

Consequently, the relevant two-particle levels of our investigation become

$$\eta_s \pi \longrightarrow D_s \pi \quad \text{and} \quad K \bar{K} \longrightarrow D \bar{K}.$$

Although the flavor content differs with regard to the previous section we continue referring to the quark-antiquark and diquark-antidiquark operator as $O^{q\bar{q}}$ and $O^{Q\bar{Q}}$, respectively. Consecutive numbering of operators is also kept in analogy to (3.19), i.e. $O^1 = O^{q\bar{q}}$, $O^2 = O^{D\bar{K}, \text{point}}$, $O^3 = O^{D_s \pi, \text{point}}$, $O^4 = O^{Q\bar{Q}}$, $O^5 = O^{D\bar{K}, 2\text{part}}$ and $O^6 = O^{D_s \pi, 2\text{part}}$.

We conduct the investigation of this flavor setup in the same style as for the $a_0(980)$ candidate. First we calculate the infinite volume two-particle levels by computing correlation functions of pseudoscalar meson creation operators, with operator structures $O \simeq (\bar{\psi}^{(f_1)} \gamma_5 \psi^{(f_2)})$. Afterwards we analyze the variational approach of the four-quark operator set, excluding and including quark loop contributions, respectively.

It is worth mentioning that in a flavor setup of $\{\bar{c}, s, \bar{u}, u\}$ with degenerate light quarks a scenario with no light-antilight annihilation refers to an explicit flavor setup of $\{\bar{c}, s, \bar{d}, u\}$. Hence, excluding $2 \times$ connected contributions will correspond to the physical circumstances of decay channels with $\pi = \pi^\pm$, instead of $\pi = \pi^0$.

Effective masses of the relevant pseudoscalar mesons D and D_s result as a consequence of fixing the hopping parameter κ , such that the observed states on the lattice correspond to physical energies. This has been done in Section 4.1.1 by computing various pseudoscalars with a tuned quark mass. Since we employ unphysical pion masses of $m_\pi \approx 300$ MeV this value of the charm quark mass is underestimated.

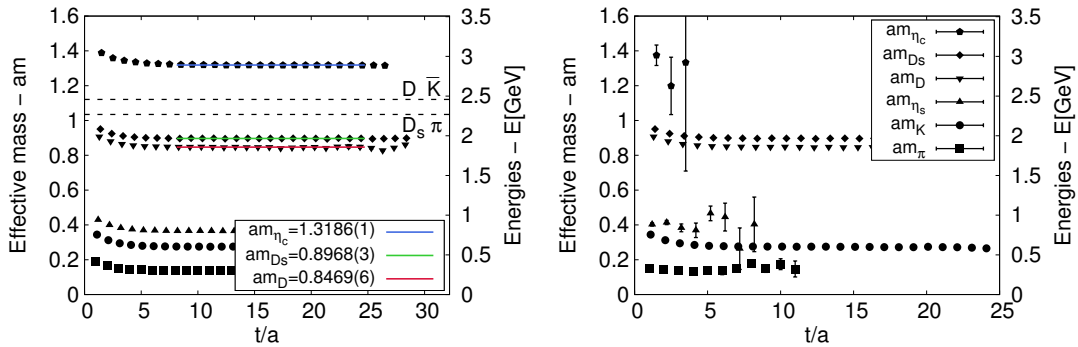


FIG. 5.16: Identification of pseudoscalar mesons D , D_s and η_c within our lattice setup (left). Infinite volume two-particle levels $D_s + \pi$ and $D + \bar{K}$ are calculated from single particle results. Effective masses extracted by assuming a simple one exponential behavior to the correlator, including fully disconnected diagrams (right). Stochastic noise increases drastically with increasing quark masses.

In Figure 5.16 we plot the effective masses of pseudoscalar quark-antiquark creation operators with all flavor combinations of this flavor setup. The three lightest states refer to π , K and η_s , and are not given explicitly, but can be found in Figure 5.2. Once

again we extract the pseudoscalar masses by omitting fully disconnected pieces of the correlator. The infinite volume two-particle levels are calculated at $am_{D_s+\pi} = 1.03(1)$ and $am_{D+\bar{K}} = 1.121(8)$. This corresponds to an energy range of $\approx 2.25 - 2.45$ GeV for the anticipated $D_{s0}^*(2317)$ candidate within our lattice setup with $m_\pi \approx 300$ MeV.

On the right of Figure 5.16 we show the change of plateaus after including fully disconnected diagrams. We observe that the increase of stochastic noise of fully disconnected pieces is proportional to the quark mass. This gives an estimate of how severe the impact of $2\times$ connected contributions to the $\{\bar{c}, s, \bar{u}, u\}$ noise in the correlation matrix is.

5.2.1 Omitting quark loop contributions

The 1×1 problem

The computation of a single diagonal correlator C_{11} with $O^1 = O^{q\bar{q}} \simeq (\bar{c}s)$ yields an effective mass with typical excited state contributions at small temporal separations. In Figure 5.17 we plot the correlation function and the corresponding effective mass. Although a plateau is reached at $t/a \gtrsim 7$, it is relatively short. Large statistical fluctuations occur for $t/a > 12$, preventing an identification of possible finite size effects contributing to the signal.

It also has to be mentioned that the state is above the ultraviolet cutoff and we hence expect additional contaminations to the correlator at large temporal separations. As before, this analysis does not include operators that resolve the neighboring two-particle levels, which thus have an implicit effect on the observed effective mass as well.

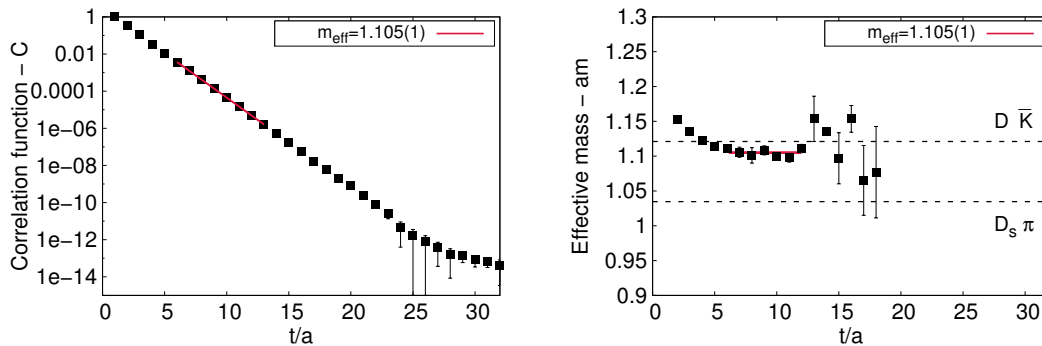


FIG. 5.17: Correlation function C_{11} (left) with $O^1 \simeq (\bar{c}s)$ and the corresponding effective mass (right), extracted by assuming contributions from a single exponential.

The 5×5 problem

We proceed to analyze the four-quark interpolator set $C_{ij} = \langle O_i O_j \rangle$ with $i, j \in [2, \dots, 7]$, excluding $2\times$ connected contributions to correlators, which corresponds to a flavor setup of $\{\bar{c}, s, \bar{d}, u\}$. Based on the experience of the previous study we do not expect the occurrence of a third low-lying state from analyzing this set of operators, but rather a resolution of the two-particle energy levels. At first we analyze the 2×2 and 4×4 submatrices corresponding to the $D_s\pi$, $D\bar{K}$ point and point+two-particle sets,

i.e. $[O^{D\bar{K}}, \text{point}, O^{D_s\pi}, \text{point}]$ and $[O^{D\bar{K}}, \text{point}, O^{D_s\pi}, \text{point}, O^{D\bar{K}}, \text{2part}, O^{D_s\pi}, \text{2part}]$, respectively. Results obtained from solving the GEP are shown in Figure 5.18.

Results shown are qualitatively in strong agreement to the previous analysis, cf. Figure 5.5. An analysis of only molecule-like operators is shown in the top left of Figure 5.18. They provide only a small overlap with the groundstate two-particle levels. Excited state contributions from various momenta slow the convergence to the ground states two-particle levels drastically. At temporal separations where the extracted signals reach the two-particle levels finite size effects within the correlator are sizeable and artificially light signals become the leading contribution. Both of these signals are not sufficient to identify plateau values and hence require an identification of the finite size effects to the correlator.

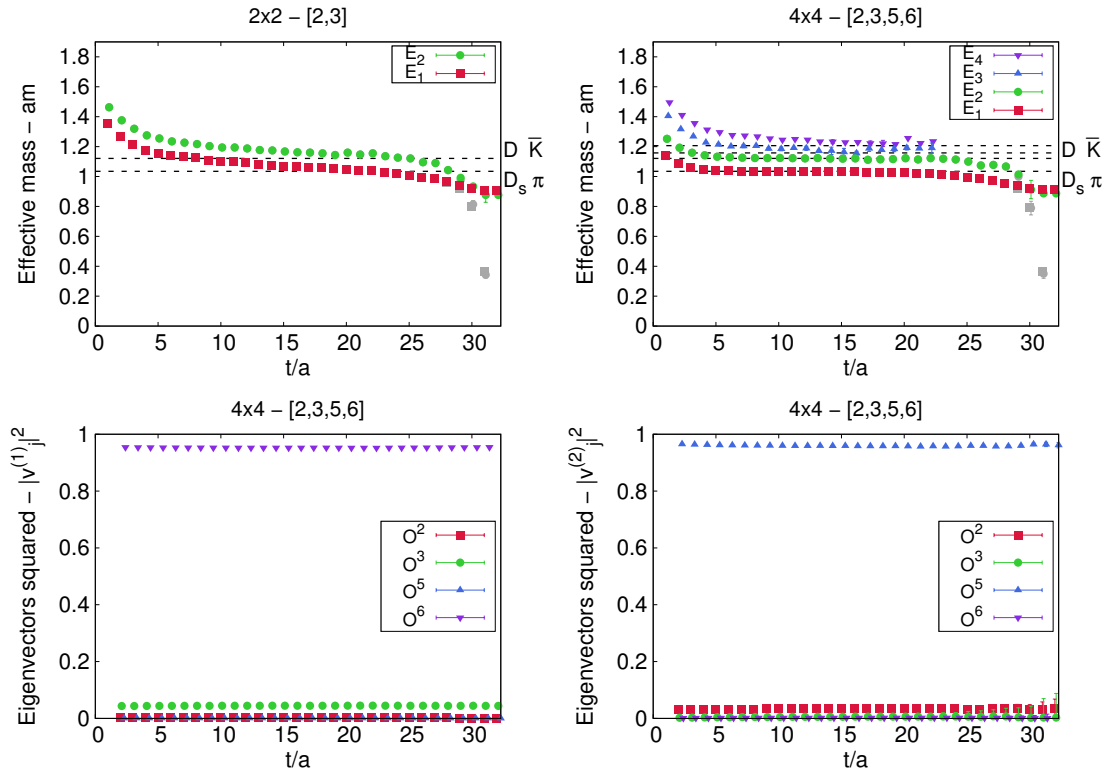


FIG. 5.18: GEP analysis of the correlation matrix omitting quark loop contributions. Analysis of the 2×2 problem with $[O^2, O^3]$ (top left) compared to the 4×4 problem with $[O^2, O^3, O^5, O^6]$ (top right). Squared eigenvector components corresponding to E_1 and E_2 of the 4×4 analysis are given on the (bottom left) and (bottom right) respectively. The lowest two dashed lines refer to the infinite volume two-particle levels.

In contrast to the point-like operators the two-particle operators excel at resolving the low energy two-particle spectrum shown in the top right of Figure 5.18. A plateau value is reached long before artificially light contributions dominate the signal, allowing a clear energy extraction. Instead of identifying a third low-lying state the molecule-like operators indicate first momentum excitations.

Compared with the analysis of the light tetraquark candidate are the first momen-

tum excitations of this flavor setup considerably close to the two-particle ground state energies. From the infinite volume levels, cf. Figure 5.2 and Figure 5.16, we calculate the energies of first momentum excitations in lattice units, i.e.

$$\begin{aligned}
aE_{D_s}(0) + aE_\pi(0) &\approx 1.03, \\
aE_D(0) + aE_{\bar{K}}(0) &\approx 1.12, \\
aE_{D_s}(1) + aE_\pi(-1) &= \sqrt{am_{D_s}^2 + (2\pi/L)^2} + \sqrt{am_\pi^2 + (2\pi/L)^2} \approx 1.16, \\
aE_D(1) + aE_{\bar{K}}(-1) &= \sqrt{am_D^2 + (2\pi/L)^2} + \sqrt{am_{\bar{K}}^2 + (2\pi/L)^2} \approx 1.21.
\end{aligned}$$

Evidently is the higher two-particle groundstate only ≈ 0.04 inverse lattice units separated from the lowest first momentum excitation.

This is troublesome for the analysis of a possible third low-lying state. As we have seen in the analysis of the $a_0(980)$ candidate, an additional signal might be squeezed in between the two-particle states. If an additional states occurs below the signal for a $D\bar{K}$ state it might happen that it will be pushed to higher energies, making it possibly difficult to distinguish between groundstates and first momentum excitations. It will thus be necessary for future computations to include definite momentum operators to the operator set as well.

Contrary to the two-particle energies of $\eta_s\pi$ and $K\bar{K}$ we do not succeed in identifying the finite size contributions to the signals of $D_s\pi$ and $D\bar{K}$ states at large temporal separations. We expect contaminations with leading artificially light signals of

$$am_{\text{art}}^{(D_s-\pi)} \approx 0.896 - 0.138 = 0.758 \quad \text{and} \quad am_{\text{art}}^{(D-\bar{K})} \approx 0.846 - 0.274 = 0.572,$$

to the two signals, respectively. However, altering the fitting procedure to (5.4) and inserting the expected artificial signals does not recover effective masses close to the infinite volume two-particle levels.

The reason for this issue is likely associated to the fact that the energies of states surpass the ultraviolet cutoff of our lattice. In this region correlation functions are affected by their own mirror image, an effect that becomes increasingly worse the further we exceed the cutoff. These additional contaminations prevent a clear identification of states wrapping around the lattice.

We will however come to realize that artificially light signals are not nearly as much an issue as it was the case for the previous investigation. Limiting the extraction of energies to temporal separations below $t_{\text{max}}/a < 20$ will suffice for the upcoming analyses.

Eventually, we include also diquark-antidiquark operators to our analysis of a $\{\bar{c}, s, \bar{d}, u\}$ flavor setup and analyze the complete set of operators. Figure 5.19 shows the observed states from this analysis. The signal for the sixth energy level is dominated by noise and not shown in the plot. The inclusion of diquark-antidiquark interpolating field operators does not resolve a third low-lying state around the infinite volume two-particle levels. Instead, an additional excited state is indicated.

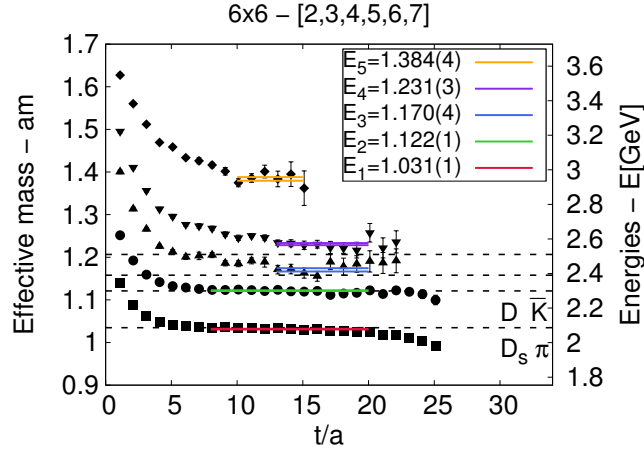


FIG. 5.19: GEP analysis for the full correlation matrix for the flavor setup $\{\bar{c}, s, \bar{d}, u\}$. The two low-lying states correspond to the expected two particle levels, followed by first momentum excitations. Diquark-antidiquark structures without loop contributions do not resolve a third low-lying state.

5.2.2 Including quark loop contributions

Like for the analysis of the light tetraquark candidate $a_0(980)$ we restrict the computation of $2\times$ connected diagrams to a maximum amount of $N_{\Delta t} = 15$ temporal separations. Consequently are observables in the following limited to temporal separations $t/a \leq 14$.

In the study of the previous flavor setup the inclusion of $2\times$ connected diagrams to the correlation matrix drastically complicated the analysis. Correlators were severely affected by finite size effects, contributing artificially light signals from particles propagating around the torus in opposite directions. Masses were extracted from relatively short plateaus at temporal separations $t/a < 10$.

This is not the case for the flavor setup $\{\bar{c}, s, \bar{u}, u\}$. Correlation functions of $2\times$ connected diagrams are not as much affected by finite volume effects as it is the case in the previous study, cf. Figure 5.9. Taking $2\times$ connected diagrams into account, the relative error of matrix elements is increased by several percent, but the particular exponential decays are not severely affected. Exceptions are the diquark-antidiquark correlators, which are largely composed of contributions from these particular diagrams, cf. Figure 4.20. A relatively mild stochastic noise on light quark propagators with starting and end points on single timeslices is expected after computing and comparing fully disconnected diagrams for all flavors in Figure 5.16. Moreover, we have seen in (4.7) that the relative exponential increase of the statistical errors of the $2\times$ connected diagrams is much better than for the light tetraquark candidate.

In Figure 5.20 we once again have a look at the diagonal elements of our correlation matrix before and after including $2\times$ connected diagrams. Due to increased energies of states the slopes of correlation functions are much steeper than before. To be able to get an impression of how severe the changes are, we zoom in on the final seven temporal separations of our computation. C_{11} is plotted by black squares.

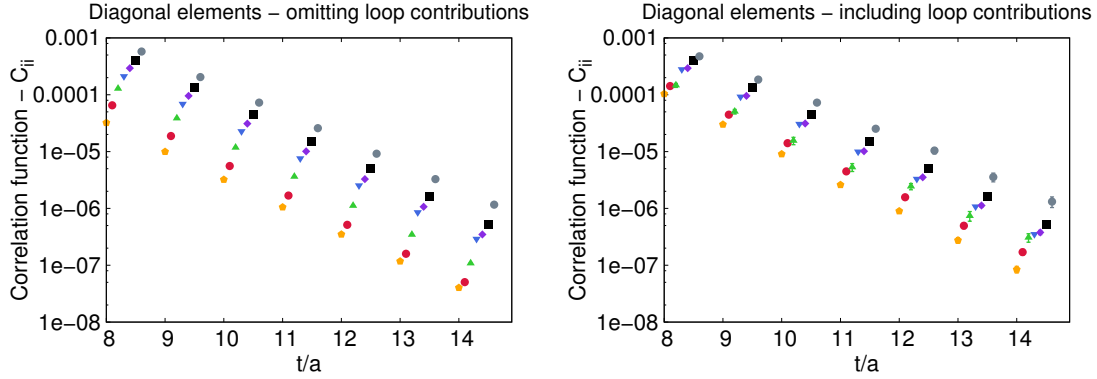


FIG. 5.20: Diagonal elements of correlation matrices omitting $2\times$ connected diagrams (left) and including $2\times$ connected diagrams (right). Off-diagonal elements are not considered. Black squares on both sides refer to C_{11} . Effects from including generally problematic diagrams are still well under control.

We repeat the analysis of the 2×2 and 4×4 submatrices including quark loops, corresponding to the $D_s\pi$, $D\bar{K}$ point and point+two-particle sets, i.e. $[O^{D\bar{K}, \text{point}}, O^{D_s\pi, \text{point}}]$ and $[O^{D\bar{K}, \text{point}}, O^{D_s\pi, \text{point}}, O^{D\bar{K}, \text{2part}}, O^{D_s\pi, \text{2part}}]$, respectively. Results obtained from solving the GEP are shown in Figure 5.21. As expected it can be seen in the top left of Figure 5.21 that the point-like operators alone are unable to resolve the two-particle states. With the addition of $2\times$ connected diagrams to the matrix only the two-particle operators provide a reasonable overlap with the states of interest.

Results from including the two-particle operators to the set is shown in the top right of Figure 5.21. The lowest state is plotted by red squares and dominated by $O^6 = O^{D_s\pi, \text{2part}}$. It shows large stochastic noise fluctuations, coming from the fully disconnected diagram of the respective two-particle operator correlation function. Nevertheless, in comparison to the previous $\eta_s\pi$ state the absence of dominating finite size effects allows for a plateau extraction on almost all temporal separations.

The quality of signal of the second lowest state plotted by green squares is comparable to the $K\bar{K}$ signal in Figure 5.18. The box diagram contributing to the two-particle correlator C_{55} with $O^5 = O^{D\bar{K}, \text{2part}}$ has a nearly negligible impact and thus allows a clear identification of the corresponding energy state.

However, states with higher momenta close to the two-particles levels are no longer resolved and can only be identified on a qualitative level. While a clear signal of these states is desirable we will see that the $D\bar{K}$ signal (green) is indeed sufficient as an upper threshold for our investigations. This once again emphasizes that future computations are obliged to include explicit momentum operators to the computation.

We proceed to extend our set of operators by including also the remaining operators to the variational approach, i.e. the diquark-antidiquark operators $O^{4,7} = O^{Q\bar{Q}}$ and the conventional quark-antiquark operator $O^1 = O^{q\bar{q}}$. As before, we add these separately one after another to the correlation matrix of point and two-particle operators and study possible differences.

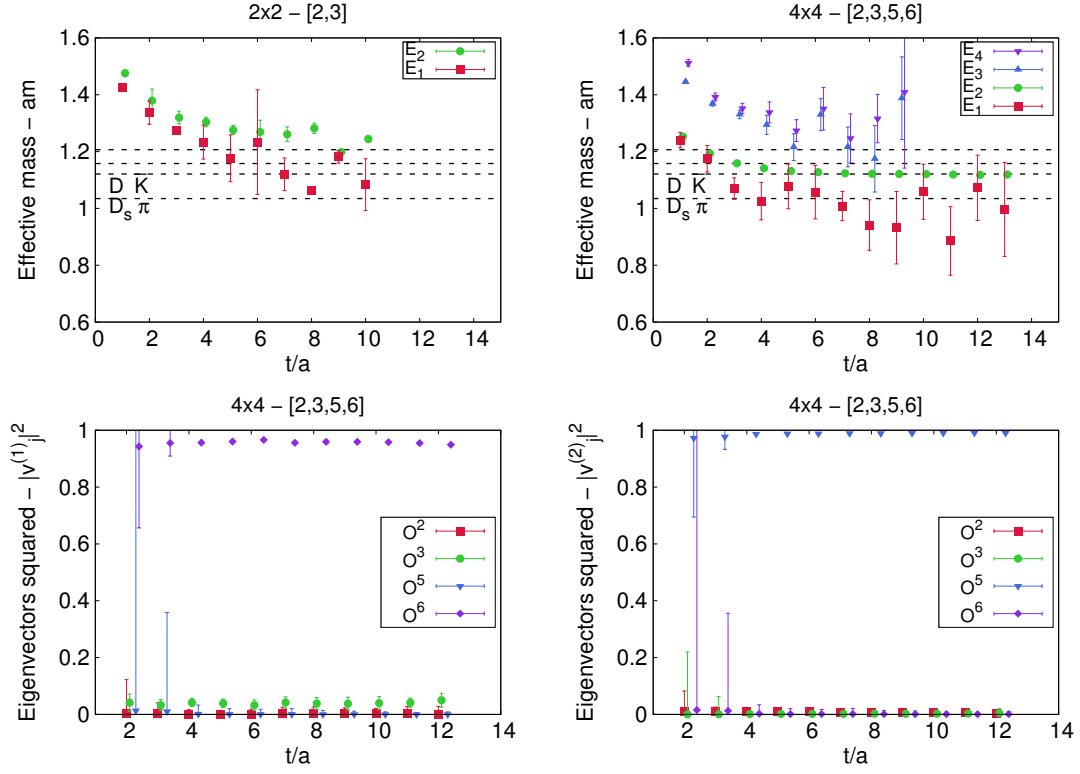


FIG. 5.21: GEP analysis of the full correlation matrix including all diagrams. Analysis of the 2×2 problem with $[O^2, O^3]$ (top left) compared to the 4×4 problem with $[O^2, O^3, O^5, O^6]$ (top right). Squared eigenvector components corresponding to E_1 and E_2 of the 4×4 analysis are given on the (bottom left) and (bottom right) respectively. Dashed lines refer to the infinite volume two-particle thresholds, calculated from single diagonal pseudoscalars without fully disconnected contributions.

In Figure 5.22 we show results of the solved GEPs of three different operator sets, in three rows i.e. $[2, 3, 4, 5, 6]$, $[1, 2, 3, 5, 6]$ and $[2, 3, 5, 6, 7]$. We present the effective masses together with the squared eigenvector components corresponding to the second and third lowest energy eigenstate. The eigenvectors to the lowest energy eigenstates (plotted by red squares) are not shown, as they are in all analyses largely dominated by O^6 , with only little statistical fluctuations.

In several aspects are the three spectra that emerge from the different operator sets in agreement with Figure 5.21. We observe a lowest energy state plotted by red squares that is very noisy through $2 \times$ connected diagrams, but allows a plateau extraction just below the expected $D_s \pi$ infinite volume level. The point operators $O^2 = O^{D\bar{K}, \text{point}}$ and $O^3 = O^{D_s \pi, \text{point}}$ show only little overlap to first momentum excitations and fail to resolve excited momenta states in a range that is of interest for our study.

However, the crucial difference of the three analyses evolves around the resolution of energy states close to the $D\bar{K}$ infinite volume level. The outcome of the first two analyses corresponding to the first two rows is in qualitative agreement to the previous investigation of the $a_0(980)$ candidate of our setup.

In the top row, for $[2, 3, 4, 5, 6]$, O^4 provides a reasonable overlap with an energy state E_3 that coincides with the first momentum excitation of $D_s\pi$. This has also been seen in the bottom left of Figure 5.10 for the relevant energy. We emphasize again, that this alone is not an indication towards a possible tetraquark structure at the respective energy. O^5 dominates the signal of E_2 , which is just on top of the anticipated $D\bar{K}$ infinite volume level.

The GEP analysis including the quark-antiquark operator to the set is shown in the center row and leads to the appearance of third low-lying energy state. This state E_1 is plotted by green circles and is found just below the $D\bar{K}$ level and pushes the respective two-particle energy level E_3 , plotted by blue triangles, slightly upwards. From the eigenvector of E_3 we see that this state is clearly dominated by $O^5 = O^{D\bar{K}, 2\text{part}}$ and still below the first momentum excitation of $D_s\pi$, making an identification with a $D\bar{K}$ state reasonable.

The appearing third state is largely dominated by O^1 , but its eigenvector components at $t/a = 6$ and $t/a = 7$ show huge statistical errors. At this point the respective eigenvalues become nearly degenerate making them difficult to distinguish, which leads to unstable solutions of the generalized eigenvalue problem. To not confuse the signals, eigenvectors are required to show a continuous behavior through all temporal separations. Statistical subsamples are in this process possibly mixed up, which eventually leads to the drastic increase of errors. However, since the effective masses show a clear behavior throughout all separations it is impossible that eigenvalues might have been mistakenly ordered in this particular analysis.

The third row of Figure 5.22 is where things become interesting. In the absence of a quark-antiquark operator we resolve a third low-lying state just below the $D\bar{K}$ level in a similar appearing style as before with the present O^1 interpolator. In strong analogy to the center row is the $D\bar{K}$ signal E_3 , plotted in the bottom row by blue triangles, again pushed upwards slightly as the additional state appears. The eigenvector compositions of these two states of interest, E_2 and E_3 , are also drastically different to what we have previously seen. Both O^5 and O^7 show a sizeable overlap to both states. However, at increasing temporal separations it appears that $O^5 = O^{D\bar{K}, 2\text{part}}$ dominates the state that coincides with the $D\bar{K}$ level and $O^7 = O^{Q\bar{Q}}$ dominates the additional low-lying state, respectively. As already argued for E_3 of the center row is also E_3 of the bottom row of Figure 5.22 noticeably below the first momentum excitation of a $D_s\pi$ state. We hence identify the three lowest states as bound groundstates, obtained from a set of operators exclusively of four-quark interpolating field operators.

	[2, 3, 4, 5, 6]	[1, 2, 3, 5, 6]	[2, 3, 5, 6, 7]
$[t_{\min}/a : t_{\max}/a]$		[4 : 12]	
$aE^{D\bar{K}}$	1.124(2)	1.134(1)	1.131(1)
$aE^{D_{s0}^*}$		1.103(1)	1.105(2)
$aE^{D_s\pi}$	1.013(8)	1.011(9)	1.015(9)

TAB. 5.2: Energy eigenstates in the region of interest extracted after solving the generalized eigenvalue problem for three different operator sets. States are obtained from the eigenvalues with slightly less temporal separations for the third lowest state.

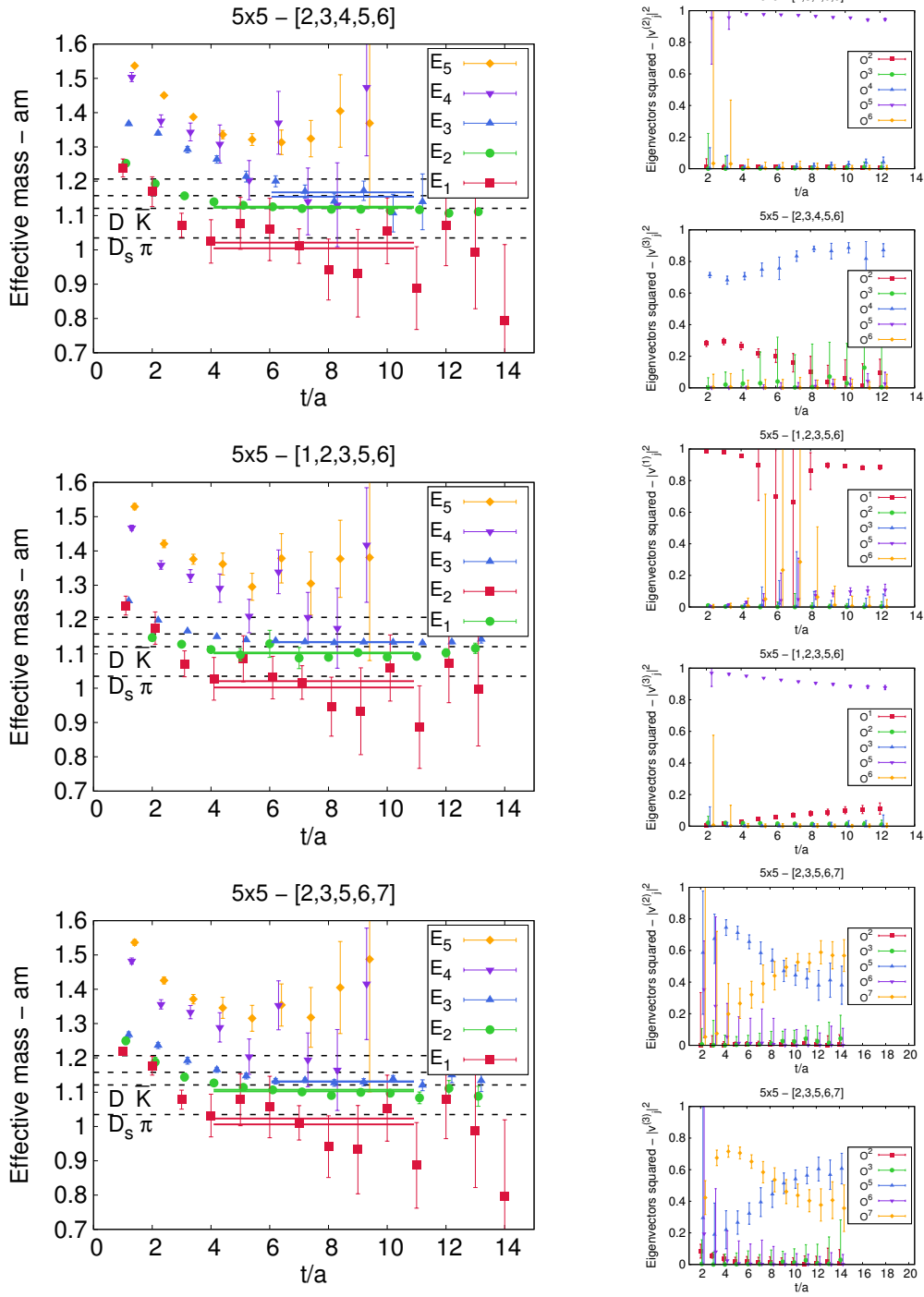


FIG. 5.22: Three GEP analyses of the full correlation matrix to the sets $[2, 3, 4, 5, 6]$ (first row), $[1, 2, 3, 5, 6]$ (second row) and $[2, 3, 5, 6, 7]$ (third row). Effective masses E_n are shown on the left and on the right the eigenvector components squared $|v_j^{(n)}|^2$ of the second and third lowest state are shown. In the analysis of $[2, 3, 5, 6, 7]$ a third low-lying state emerges in the absence of $q\bar{q}$ interpolating field operators.

It is important to note that this observation has not been made in the previous analysis of the very same heavy tetraquark candidate, i.e. for a flavor setup of $\{\bar{c}, s, \bar{d}, u\}$, cf. Figure 5.19.

In Figure 5.23 we present the extracted energy levels resulting from GEP analyses of various operator sets. In the relevant range of temporal separations the corresponding squared eigenvector components are fitted to constant values and shown in Figure 5.24.

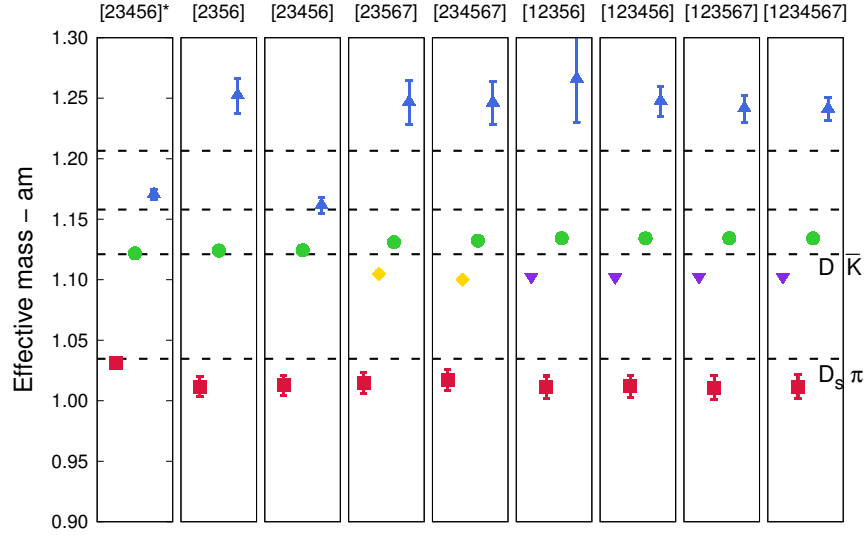


FIG. 5.23: Multiple energy levels from various GEP analyses. The title of each column refers to the operator set of each GEP. The asterisk on the first column indicates the absence of quark loop contributions from the analysis. Red and green symbols refer to states dominated by two-particle operators O^6 and O^5 respectively. Blue symbols represent the first state well-separated from the groundstate levels. Violet and yellow symbols are additional low-lying states between the two-particle levels.

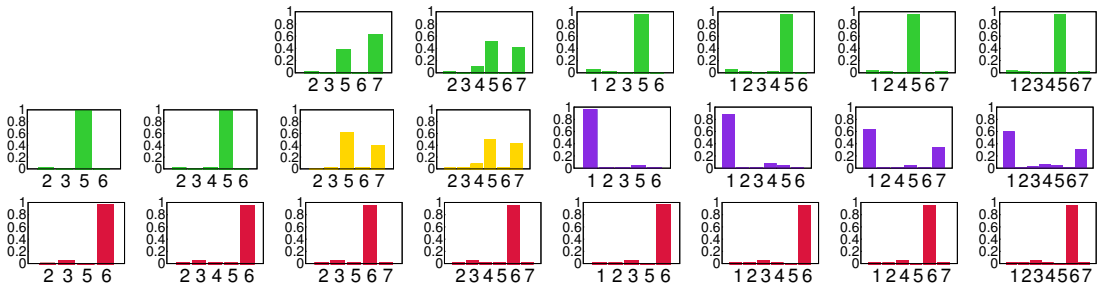


FIG. 5.24: Constants fitted to squared eigenvector components of the two and three lowest eigenvalues. The extracted effective masses from these eigenvalues are shown in Figure 5.23, matching colors refer to associated eigenvalues and eigenvectors. Bases are paired vertically, labels on the x-axis refer to the particular operator contribution to the respective eigenvalue.

The color of eigenvectors is chosen to emphasize characteristic operator compositions of each state. The same color is then accordingly applied to the energy states in Figure 5.23. Red and green emphasize states that are completely governed by $O^6 = O^{D_s\pi, 2\text{part}}$ and $O^5 = O^{D\bar{K}, 2\text{part}}$, respectively. Strictly speaking is thus the green color of the third state in $[2, 3, 5, 6, 7]$ and $[2, 3, 4, 5, 6, 7]$ not entirely correct. However, these two states show a dominant contribution of O^5 at increasing temporal separations. Since the range of the fit to the eigenvector components is determined by the range in which effective masses were read-off, the presented values tend to understate the actual operator contribution at large temporal separations.

Yellow and violet states emphasize a third low-lying state between the two-particle levels, which is found at the same energy value throughout our various operator sets. While only four-quark operators were utilized to obtain the states represented by yellow diamonds, the same state was found employing a quark-antiquark operator. Whenever $O^1 = O^{q\bar{q}}$ is included to the set of operators a third low-lying state emerges. If additionally an operator with a heavy diquark-antidiquark structure $O^7 = O^{Q\bar{Q}}$ is considered it also shows a sizeable overlap to the observed third low-lying state.

In this section we employ a tuned valence charm quark mass to study the heavy tetraquark candidate $D_{s0}^*(2317)$. In contrast to the previous section the inclusion of quark loop contributions to the correlation matrix does not drastically contaminate our analysis. Stochastic errors increase, but still allow a study at larger temporal separations. We identify both two-particle levels $D_s\pi$ and $D\bar{K}$. Quark loop contributions are sizeable in the former state, resulting in an increased stochastic error of the signal. The addition of a quark-antiquark structure to the set of two-particle operators leads to a third state, which is found between the two-particle levels just below the $D\bar{K}$ state. The same state is also found in the absence of a conventional quark-antiquark structure by including a heavy diquark-antidiquark structure to the set of operators. In this case the appearing state and the $D\bar{K}$ state show large overlap to two-particle structures. For larger temporal separations the third low-lying state is dominated by a diquark-antidiquark structure and $D\bar{K}$ by its respective two-particle operator. In the presence of both quark-antiquark and diquark-antidiquark structures in the operator set the third low-lying state is governed by the former structure with sizeable contributions from the latter. These findings are interpreted as a possible implication for a state beyond the conventional quark-antiquark structure.

The analyzed states surpass the ultraviolet cutoff of our lattice and hence, are in fact not accessible with our lattice setup. The fact that the emerging picture is quite consistent between the tetraquark candidates might indicate that effects from this violation are small, yet results should be taken with caution.

CONCLUSIONS & RESEARCH PERSPECTIVES

In this thesis we study two scalar tetraquark candidates on the lattice, the light scalar $a_0(980)$ and the heavy scalar $D_{s_0}^*(2317)$. To investigate these states we use the variational method. By constructing two- and various four-quark creation operators we resolve the energy region of interest and provide different quark structures for the tetraquark candidate. We aim to find a state with a sizeable overlap to such a four-quark structure as an indication for a possibly exotic quark structure.

Such a study relies on an extensive computation of quark propagators, which are contracted differently in many correlation functions. Since we plan to solve a generalized eigenvalue problem it is vital for our analysis to ensure that every element is calculated as precisely as possible. Hence, we explore various methods to compute correlation functions of two- and four-quark operators of different structures. These investigations have been performed on both quark flavor structures, of the light and heavy candidate. Results agree for both candidates and we expect them to hold at least qualitatively also for other tetraquark candidates and four-quark systems. For changing quark masses, quark flavor compositions or when studying different lattice QCD quark actions, we expect deviations. Investigations reported in Chapter 4 provide a comprehensive overview of existing methods and helpful guidelines, which methods to choose for which kind of diagram type.

We find that methods, which average a diagram over space, are more efficient than methods, which do not. We emphasize especially the utilization of the one-end trick over standard stochastic timeslice-to-all propagators, as in this case fewer stochastic noise terms are introduced. Moreover, we see that the dynamics of two independent particles on a single timeslice is in favor for an improved signal. Omitting spatial sums over only two-quark field operators seems to result in much smaller statistical errors than omitting a sum over four-quark field operators. Sequential propagators are an indispensable procedure for the computation of propagators which connect two different spatial points \mathbf{x} and \mathbf{y} on the same timeslice. Diagrams involving such propagators are generated by operators of the form $(\bar{\psi}^{(f_1)}\Gamma_1\psi^{(f_3)})_{\mathbf{x}}(\bar{\psi}^{(f_3)}\Gamma_2\psi^{(f_2)})_{\mathbf{y}}$, which are an integral part of every tetraquark study. We also find that stochastic methods are more efficient for lighter quarks and less efficient for heavy quarks. This can be seen clearly throughout Section 4.2, whenever two realizations of method (b) are shown. Later on, increased statistical fluctuations are further identified on fully disconnected pieces of heavy pseudoscalar $q\bar{q}$ correlation functions, which origin from rather strong fluctuations of the gauge links. Overall we identify what we call the $2\times$ connected pieces of four-quark correlation functions as problematic, but still feasible. Since the error of these pieces will eventually dominate the correlator it is utterly relevant to determine a well-suited

method to compute these diagrams, in order to obtain a reliable signal. Especially correlation functions with a diquark-antidiquark content are largely composed of these contributions.

In the last chapter of this thesis we present our analyses of the two tetraquark candidates $a_0(980)$ and $D_{s_0}^*(2317)$. We split both discussions in two parts, where we first omit quark loop contributions to correlation functions and later include them for a complete analysis. Without quark loop contributions the analyses of both tetraquark candidates is reduced to a study of four-quark operators. Here the respective two-particle energy spectra are resolved, as well as their first momentum excitations. In the energy regions of interest no indications for additional bound states are found.

Including quark loop contributions to the analysis of the light tetraquark candidate $a_0(980)$ drastically worsens the circumstances of our analysis. These diagrams are not only affected by drastically increased stochastic noise but also display sizeable contributions from finite size effects. We identify these effects as artificially light signals from two particles propagating around the torus in opposing directions. Due to the large stochastic noise and a relatively small number of temporal separations it is impossible to identify these finite size contributions to every element precisely. We thus cannot include these effects to our analysis and instead, are forced to extract plateau values at relatively small temporal separations.

At relatively small temporal separations we find a third low-lying state only by including a conventional $q\bar{q}$ structure to the respective set of meson creation operators. Due to the high overlap of this state with the quark-antiquark operator we identify this state as the candidate for the $a_0(980)$ within our lattice setup. It is located close to the two Kaon threshold and displays an overlap to the neighboring two particle levels. We attribute this behavior to the shared artificially light state contributions with the $\eta_s\pi$ signal and the close proximity to the $K\bar{K}$ level. Given an improved statistics it can be assumed that the diagonalization of operators becomes much better, allowing a more distinct identification of the third low-lying state as conventional $q\bar{q}$ state.

To study the $D_{s_0}^*(2317)$ with our lattice ensemble we tune a value for the quark mass to coincide with the physical energies of light pseudoscalar open-charm states. Hence, it is important to note that on our $N_f = 2 + 1$ ensemble calculations involving this charm quark mass correspond to a partially quenched setup, i.e. no charm-anticharm creation and annihilation from the vacuum is included. Moreover, we find the two-particle energy levels of this analysis above the ultraviolet cutoff of our lattice. Strictly speaking, these energies are not accessible for our ensemble, but a consistent picture with regard to the light tetraquark candidate might indicate that effects from exceeding the cutoff are small.

In contrast to the study of the light tetraquark candidate $a_0(980)$ the inclusion of quark loop contributions to the correlation matrix is only a minor problem. The overall statistical error on all matrix elements is increased, but no sizeable contributions from finite size effects are observed. Furthermore, we have identified a much more moderate exponential increase in the relative statistical error of $2\times$ connected diagrams with respect to the $4\times$ connected diagrams, compared to the light tetraquark study. This was done by considering the asymptotic exponential decay of squared correlation functions. The exponential increase was found to be implicitly given by the mass difference of a two-particle state to a single-particle state.

Solving the generalized eigenvalue problem for various operator sets we find a third low-lying state between the two two-particle levels. However, contrary to the analysis of the light tetraquark candidate, we also find an indication for this third low-lying state by employing only four-quark structures. The fact that this state was not found omitting quark loop contributions further emphasizes their relevance for the study of tetraquark candidates and, in particular, for diquark-antidiquark matrix elements. The same low-lying state is also seen in the case that diquark-antidiquark operators are absent, with a strong overlap to a quark-antiquark structure. In the analysis of the full operator set the state shows a strong overlap to a quark-antiquark structure, but also of sizeable magnitude to a diquark-antidiquark structure. We interpret this behavior, in combination with the fact that the state emerges also by employing only four-quark operators, as an indication for a quark structure beyond a conventional quark-antiquark pair.

Investigating possibly bound states of four-quarks in full QCD is still a very challenging task on the lattice. As it is pointed out several times these states are very difficult to determine due to the proximity of two-particle thresholds. To further complicate the matter such states are not necessarily exotic mesons, but possibly resonances, which are not bound states of QCD. This is among other possibilities another realistic scenario for the case of the $a_0(980)$. The study of these short-lived particles on the lattice has only become possible in recent years. Resonance properties can be extracted by conducting extensive studies of multi-particle operator sets on various lattice volumes. The dependence of the two-particle energy levels as a function of the finite lattice volume can then be associated with various scattering amplitudes. However, calculations of coupled-channel meson-meson scattering are still at the very start of their lifetime. In [106] an extensive study of this kind is presented for a first time. The authors report on various results for the irreducible representations of moving frame analyses and employ a so-called K -matrix approach to interpolate between their lattice volumes. From this incredible amount of data they eventually obtain the S -wave scattering amplitude for their setup of $m_\pi \approx 400$ MeV.

Altogether the consistency between the results of both scalar tetraquark candidates that were studied in this thesis is very encouraging. To obtain more quantitative results one would require both a larger temporal extent of the lattice but also finer lattice spacing. The former is desirable in the case of the $a_0(980)$, as it will reduce the effects from particles traveling in opposite directions. The latter is required to increase the ultraviolet cutoff of the lattice to higher energies and thus to allow for a safer analysis of two-particle states with an open-charm meson. From what we have seen in this thesis especially the investigation of heavier tetraquark candidates might be a promising endeavour. Here, one needs to expand the operator set and include operators that excite states with explicit relative momenta. As the masses of tetraquark candidates become larger, the separations to momentum excitations become smaller. We have seen by the example of our $D_{s0}^*(2317)$ studies, that it will eventually become difficult to identify states precisely. Extending the Dirac structure of the set of operators would allow the simultaneous calculation of the axial vector partner of the $D_{s0}^*(2317)$, the $D_{s1}(2460)$, with reasonable effort. Given that the lattice extent is well-suited to study the candidates in question a solid foundation is provided by this thesis. For heavier excited candidates,

however, the operator set needs to be extended even further. As multiple two-particle thresholds will fit below the ground state energies of excited heavy tetraquarks, it has to be ensured that all of these states are resolved precisely.

APPENDIX A NOTATIONS AND CONVENTIONS

In this work we use natural units $\hbar = c = 1$, which leads to an energy-length conversion of

$$\hbar c = 197.327 \text{ MeV fm} = 1. \quad (\text{A.1})$$

All results of this work are obtained from calculations performed in Euclidean spacetime. The transition from a quantum field theory in Minkowski space to a Euclidean spacetime is a crucial step to allow a treatment of the path integral similar to quantum statistical mechanics. The otherwise oscillating action in the Minkowski path integral does so take over the role of an exponential weight, which eventually enables a stochastic evaluation of the path integral. Hence, Euclidean quantities are not further emphasized.

A.1 Gamma matrices

In the chiral representation the Dirac matrices are defined by

$$\begin{aligned} \gamma_0 &= \begin{pmatrix} 0 & 0 & +1 & 0 \\ 0 & 0 & 0 & +1 \\ +1 & 0 & 0 & 0 \\ 0 & +1 & 0 & 0 \end{pmatrix}, & \gamma_1 &= \begin{pmatrix} 0 & 0 & 0 & +i \\ 0 & 0 & +i & 0 \\ 0 & -i & 0 & 0 \\ -i & 0 & 0 & 0 \end{pmatrix}, \\ \gamma_2 &= \begin{pmatrix} 0 & 0 & 0 & +1 \\ 0 & 0 & -1 & 0 \\ 0 & -1 & 0 & 0 \\ +1 & 0 & 0 & 0 \end{pmatrix}, & \gamma_3 &= \begin{pmatrix} 0 & 0 & +i & 0 \\ 0 & 0 & 0 & -i \\ -i & 0 & 0 & 0 \\ 0 & +i & 0 & 0 \end{pmatrix}, \end{aligned} \quad (\text{A.2})$$

where we employ a notation for γ_μ analogue to Minkowski space $\mu = 0 \dots 3$, where $\mu = 0$ refers to time. They are hermitian and satisfy the anticommutation relation, i.e.

$$\gamma_\mu = \gamma_\mu^\dagger = \gamma_\mu^{-1} \quad , \quad \{\gamma_\mu, \gamma_\nu\} = 2 \delta_{\mu\nu} \mathbb{1} \quad (\text{A.3})$$

In addition, we define the product of the four gamma matrices

$$\gamma_5 = \gamma_0 \gamma_1 \gamma_2 \gamma_3 = \begin{pmatrix} +1 & 0 & 0 & 0 \\ 0 & +1 & 0 & 0 \\ 0 & 0 & -1 & 0 \\ 0 & 0 & 0 & -1 \end{pmatrix}, \quad (\text{A.4})$$

which is also hermitian and anticommutes with all Dirac matrices.

Together with the antisymmetric

$$\sigma_{\mu\nu} = \frac{1}{2i} [\gamma_\mu, \gamma_\nu], \quad (\text{A.5})$$

a complete basis of complex 4×4 matrices over \mathbb{C} is given by the set of 16 matrices

$$\Gamma \in \{\mathbf{1}, \gamma_\mu, \sigma_{\mu\nu}, \gamma_5 \gamma_\mu, \gamma_5\}, \quad (\text{A.6})$$

the elements of the *Clifford algebra*.

A.2 Parity transformation

A parity transformation P reflects spatial coordinates and acts on the lattice fields as:

$$\begin{aligned} \psi(\mathbf{x}, x_0) &\xrightarrow{P} \psi(\mathbf{x}, x_0)^P = \gamma_0 \psi(-\mathbf{x}, x_0), \\ \bar{\psi}(\mathbf{x}, x_0) &\xrightarrow{P} \bar{\psi}(\mathbf{x}, x_0)^P = \bar{\psi}(-\mathbf{x}, x_0) \gamma_0, \\ U_i(\mathbf{x}, x_0) &\xrightarrow{P} U_i(\mathbf{x}, x_0)^P = U_i(-\mathbf{x} - \hat{i}, x_0)^\dagger, \\ U_0(\mathbf{x}, x_0) &\xrightarrow{P} U_0(\mathbf{x}, x_0)^P = U_0(-\mathbf{x}, x_0). \end{aligned} \quad (\text{A.7})$$

A.3 Charge conjugation

A charge transformation C transforms a particle into an antiparticle and vice versa and acts on the lattice fields as

$$\begin{aligned} \psi(x) &\xrightarrow{C} \psi(x)^C = C^{-1} \bar{\psi}(x)^T, \\ \bar{\psi}(x) &\xrightarrow{C} \bar{\psi}(x)^C = -\psi(x)^T C, \\ U_\mu(x) &\xrightarrow{C} U_\mu(x)^C = U_\mu(x)^*. \end{aligned} \quad (\text{A.8})$$

The charge conjugation matrix C is defined by the relation

$$C \gamma_\mu C^{-1} = -\gamma_\mu^T, \quad (\text{A.9})$$

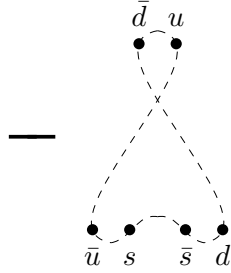
which is given in chiral representation by

$$C = i \gamma_2 \gamma_0. \quad (\text{A.10})$$

APPENDIX B COMPUTATION OF MATRIX ELEMENTS

B.1 Spin diagrams

The different spin diagrams are a simple graphical guide for reordering the Grassmann valued quark spinors within the fermionic expectation value, in order to contract equal flavors. As such not only the respective sign for the correlator, which emerges from shifting the Grassmann variables, but also the structure of the trace in spin space can be read off. If necessary, the spatial representation might aid to set the endpoints of the propagators. The spin diagram of C_{12} is given by



which reads as a single trace in spin space. The sign from shifting the Grassmann variables is negative for an odd number of line intersections and positive for an even number of line intersections. Constructs with zero intersections count also as a negative contribution. This is caused due to the possibility to interchange two quark pairs within an operator without the need for a sign change. Quark pairs in Figure 3.4 are ordered to provide a clear representation of the spin structure.

The ordering of the different quark propagators after contracting the spinors reads off to be

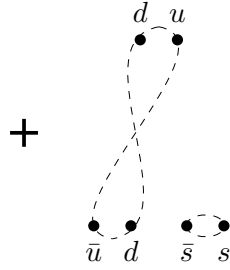
$$C_{12} \simeq - \left\langle \text{tr}_{\text{spin}} \left[G^{(d)} G^{(u)} \gamma_5 G^{(s)} \gamma_5 \right] \right\rangle_U. \quad (\text{B.1})$$

Invariance of the trace under cyclic permutations is encoded in the diagrams by continuous dashed lines, making a starting position irrelevant. Different Dirac structures between the spinors have to be inserted by hand, i.e. $\mathbb{1}$ between \bar{d} and u and a γ_5 between each of the two quark pairs at the bottom, cf. (3.19). Due to diagonal color indices of the operators the traces in color and spin conveniently merge. For the specific choice of O^2 the four quarks at the bottom share their spatial coordinates, so that we end up with

$$C_{12}(t) = -\frac{1}{V_s} \sum_{\mathbf{x}, \mathbf{y}} \left\langle \text{tr} \left[G^{(d)}(x, t_1; y, t_2) G^{(u)}(y, t_2; x, t_1) \gamma_5 G^{(s)}(x, t_1; x, t_1) \gamma_5 \right] \right\rangle_U. \quad (\text{B.2})$$

The spin structure remains the same for O^5 as indicated in Figure 3.4, but the bottom quark pairs are distributed to different spatial coordinates.

In an equal manner does the spin diagram of C_{13}



lead to

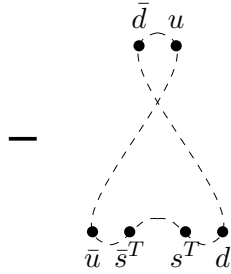
$$C_{13}(t) = + \frac{1}{V_s} \sum_{\mathbf{x}, \mathbf{y}} \left\langle \text{tr} \left[G^{(d)}(x, t_1; y, t_2) G^{(u)}(y, t_2; x, t_1) \gamma_5 \right] \text{tr} \left[G^{(s)}(x, t_1; x, t_1) \gamma_5 \right] \right\rangle_U, \quad (\text{B.3})$$

where the two separate spin structures with one and zero line intersections induce an overall positive sign.

Spin diagrams involving the diquark-antidiquark operator O^4 pose a distinct scenario. These interpolators are not only no longer diagonal in color, but also transposed quark spinors occur. To contract this operator with the others certain quark pairs might need to be transposed. For each transposed spinor pair *another* sign change takes place.

$$\bar{\psi}_A^T \psi_B^T = (\bar{\psi}_A)^T (\psi_B)^T = \bar{\psi}_A \psi_B = -\psi_B \bar{\psi}_A = -(\psi \bar{\psi})_{BA} = -((\psi \bar{\psi})_{AB})^T \quad (\text{B.4})$$

Such sign changes from initial operations are taken into account for the diagrammatic spin representation in Figure 3.4, cf. e.g. $C_{2,5;4}^{(4 \times \text{connected})}$. Hence, any further sign change from transposed spinor pairs occur only during the fermion contraction. The spin diagram for C_{14}



implies an ordering of quark propagators according to

$$C_{14} \simeq + \left\langle \text{tr}_{\text{spin}} \left[G^{(d)} G^{(u)} (C \gamma_5)^\dagger \left(G^{(s)} \right)^T (C \gamma_5)^\dagger \right] \right\rangle_U, \quad (\text{B.5})$$

including a change in the overall sign of the correlator with respect to the spin diagram due to the contraction of two transposed spinors. The spatial coordinates of the propagators remain the same as in the previous two examples and a permutation of color

indices needs to be added, cf. (3.19), resulting in

$$C_{14}(t) = +\frac{1}{V_s} \sum_{\mathbf{x}, \mathbf{y}} \epsilon_{abc} \epsilon_{ade} \left\langle \text{tr}_{\text{spin}} \left[G_{cf}^{(d)}(\mathbf{x}, t_1; \mathbf{y}, t_2) G_{fd}^{(u)}(\mathbf{y}, t_2; \mathbf{x}, t_1) (C\gamma_5)^* \right. \right. \\ \left. \left. \left(G_{be}^{(s)}(\mathbf{x}, t_1; \mathbf{x}, t_1) \right)^T (C\gamma_5)^* \right] \right\rangle_U. \quad (\text{B.6})$$

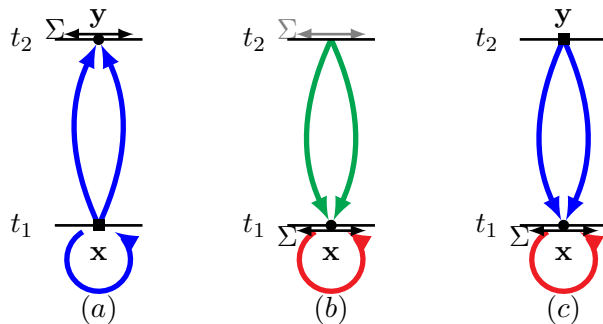
To summarize the above mentioned properties of spin diagrams:

- Continuous dashed lines represent spin traces.
- 0 and an odd number of line intersections implies a negative sign, an even number of line intersections implies a positive sign.
- The overall sign is a product of all constituent contributions.
- Sign changes from initial operations are taken into account.
- Contracting pairs of transposed quark spinors results in another sign change, cf. (B.4).

B.2 Application of techniques

Especially throughout Section 4.2 we utilize color schemes on spatial representations of correlators to indicate which techniques we employ to estimate the particular propagators. Those techniques are **point-to-all propagators**, **stochastic timeslice-to-all propagators** and the **one-end trick** and were introduced in Section 3.4. While both diagrammatic representations intend to simplify the derivation of the correlator structure, the color scheme applied to the spatial diagrams reveals the final computational implementation of techniques in a convenient way.

Although the color and spin structure of the various correlators differ, they can be computed by the same combination of techniques, as long as they share their spatial representation, cf. Figure 3.3. This is the case for the in Appendix B.1 discussed two-quark – four-quark correlators C_{12} , C_{13} and C_{14} . The candidate methods are illustrated by the following diagrams:



After the mathematical expression for a correlator is derived, suited propagator techniques can be applied to compute the correlation function at many temporal separations. We present the implementation of three methods for C_{12} , which were derived in (B.2):

- Method (a):

$$C_{12}(t) = - \left\langle \left(\sum_{\mathbf{y}} \phi_{\text{pnt}}^{(d)}(\mathbf{y}, t_2)[a, A, \mathbf{x}, t_1]^\dagger \gamma_5 \phi_{\text{pnt}}^{(u)}(\mathbf{y}, t_2)[b, B, \mathbf{x}, t_1] \right) \right. \\ \left. (\gamma_5)_{B;C} \phi_{\text{pnt}}^{(s)}(\mathbf{x}, t_1)[a, A, \mathbf{x}, t_1] \right\rangle_U. \quad (\text{B.7})$$

- Method (b):

$$C_{12}(t) = - \frac{1}{N_{\text{one}}} \sum_{n=1}^{N_{\text{one}}} \frac{1}{N_{\text{sto}}} \sum_{n'=1}^{N_{\text{sto}}} \frac{1}{V_s} \left\langle \sum_{\mathbf{x}} \left(\tilde{\phi}_{\text{one}}^{(u)}(\mathbf{x}, t_1)[t_2, \mathbb{1}, n]^\dagger \gamma_5 \phi_{\text{sto}}^{(s)}(\mathbf{x}, t_1)[t_1, n'] \right) \right. \\ \left. \left(\xi_{\text{sto}}(\mathbf{x}, t_1)[t_1, n']^\dagger \phi_{\text{one}}^{(d)}(\mathbf{x}, t_1)[t_2, n] \right) \right\rangle_U. \quad (\text{B.8})$$

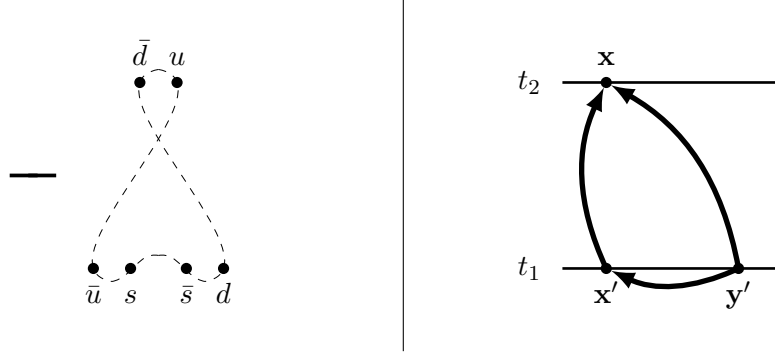
- Method (c):

$$C_{12}(t) = - \frac{1}{N_{\text{sto}}} \sum_{n=1}^{N_{\text{sto}}} \left\langle (\gamma_5)_{B;A} \sum_{\mathbf{x}} \left(\phi_{\text{pnt}}^{(u)}(\mathbf{x}, t_1)[a, A, \mathbf{y}, t_2]^\dagger \phi_{\text{sto}}^{(s)}(\mathbf{x}, t_1)[t_1, n] \right) \right. \\ \left. \left(\xi_{\text{sto}}(\mathbf{x}, t_1)[t_1, n]^\dagger \gamma_5 \phi_{\text{pnt}}^{(d)}(\mathbf{x}, t_1)[b, B, \mathbf{y}, t_2] \right) \right\rangle_U. \quad (\text{B.9})$$

ϕ_{pnt} , ϕ_{sto} , ξ_{sto} , ϕ_{one} and $\tilde{\phi}_{\text{one}}$ refer to the sources and solutions of the linear systems ($D^{(f)}\phi^{(f)} = \xi$) for the techniques of **point-to-all propagators**, **stochastic timeslice-to-all propagators** and the **one-end trick**, respectively. Essentially in the same way the techniques can also be applied to C_{13} (B.3) and C_{14} (B.6).

B.3 Application of sequential propagation

We utilize sequential propagation whenever quark spinors are embedded in a mutual spin structure, but are distributed over different spatial coordinates on the same timeslice. One example for this practice can be found in C_{15} . Its spin structure (left) is identical to C_{12} but in terms of its spatial representation (right) the K and \bar{K} meson are created at different points in space, i.e. \mathbf{x}' and \mathbf{y}' .



The mathematical expression for C_{15} can be derived from its diagrams

$$C_{15}(t) = -\frac{1}{V_s^{3/2}} \sum_{\mathbf{x}, \mathbf{x}', \mathbf{y}'} \left\langle \text{tr} \left[G^{(d)}(\mathbf{y}', t_1; \mathbf{x}, t_2) G^{(u)}(\mathbf{x}, t_2; \mathbf{x}', t_1) \gamma_5 G^{(s)}(\mathbf{x}', t_1; \mathbf{y}', t_1) \gamma_5 \right] \right\rangle_U, \quad (\text{B.10})$$

where we identify a sequential propagation of the form

$$G^{(u;s)}(\mathbf{x}, t_2; \mathbf{y}', t_1)[\gamma_5] \equiv \sum_{\mathbf{x}'} G^{(u)}(\mathbf{x}, t_2; \mathbf{x}', t_1) \gamma_5 G^{(s)}(\mathbf{x}', t_1; \mathbf{y}', t_1), \quad (\text{B.11})$$

and hence are able to calculate the diagram via the technique of e.g. the one-end trick

$$\begin{aligned} C_{15}(t) &= -\frac{1}{V_s^{3/2}} \sum_{\mathbf{x}, \mathbf{y}'} \left\langle \text{tr} \left[\left(G^{(d)}(\mathbf{x}, t_2; \mathbf{y}', t_1) \right)^\dagger \gamma_5 G^{(u;s)}(\mathbf{x}, t_2; \mathbf{y}', t_1)[\gamma_5] \right] \right\rangle_U \\ &\rightarrow \frac{1}{N} \sum_{n=1}^N -\frac{1}{V_s^{3/2}} \sum_{\mathbf{x}} \left\langle \left(\tilde{\phi}_{\text{one}}^{(d)}(\mathbf{x}, t_2)[t_1, n] \right)^\dagger \gamma_5 \psi_{\text{one}}^{(u;s)}(\mathbf{x}, t_2)[t_1, \gamma_5; t_1, n] \right\rangle_U. \end{aligned} \quad (\text{B.12})$$

With a shared origin of the propagators at \mathbf{y}' this realization corresponds to a sequential propagation within the source timeslice. The procedure to obtain solutions ψ follows the instructions from Section 3.4.4, i.e.

$$\begin{aligned} \sum_y D_{a,A;b,B}^{(s)}(x; y) \phi_{b,B}^{(s)}(y)[t_1, n] &= \xi_{a,A}(x)[t_1, n], \\ \sum_y D_{a,A;b,B}^{(u)}(x; y) \psi_{b,B}^{(u;s)}(y)[t_1, \gamma_5; t_1, n] &= (\gamma_5 \phi)_{a,A}(\mathbf{x}, x_0)[t_1, n] \delta(x_0; t_1). \end{aligned} \quad (\text{B.13})$$

Sequential propagators within the sink timeslice or with other propagator techniques are obtained in a similar manner.

B.4 Propagator content of methods

In the following we present the minimal number of inversions required to construct the methods presented in Section 4.2. Details given are dependent on the Dirac and flavor structure of the operators in use, for which we restrict ourself to the Dirac structure cf. (3.19), and flavor structure $\{\bar{\psi}^{(f_1)}, \psi^{(f_2)}, \bar{\psi}^{(f_3)}, \psi^{(f_3)}\}$ relevant throughout this thesis.

Solutions to linear system $D\phi = \xi$ are labeled by ϕ , if its source is a fixed point or a stochastic source and ψ , if its source is a solution to a linear system itself, referring to the notation of Section 3.4.

Each technique features a distinctive minimal number of inversions to be performed, i.e. $12\times$ the number of independently chosen spacetime points for point-to-all propagators or the number of independently chosen stochastic sources for stochastic propagators. Multiples of these are not explicitly given below. Consequently, each row has to be multiplied with its respective amount of repeated inversions, i.e. e.g. $\times 12$ per independent spacetime point for point-to-all propagators, or $\times N_{\text{sto}}$ for stochastic timeslice-to-all propagators. Different Dirac structures at the source of the one-end trick are distinguished by $\phi^{(f_1)}, \tilde{\phi}^{(f_2)} \equiv \phi^{(f_1)}, \tilde{\phi}^{(f_2)}[\mathbf{1}]$, cf. Section 3.4.3.

	(a)	(b)
one-end trick	$\phi^{(f_1)}, \tilde{\phi}^{(f_2)}$	
point-to-all propagators		$\phi^{(f_1)}, \phi^{(f_2)}$

TAB. B.3: Number of solutions required for the different methods of C_{11} .

For the simplest diagram of the correlation matrix we find a minimum of two solutions for the one-end trick and $12\times$ two solutions for point-to-all propagators. This refers to a single stochastic source and a single spacetime point, respectively. Note that for the first half of our investigation the flavor basis of interest is $\{\bar{d}, u, \bar{s}, s\}$, i.e. the flavor basis of an $a_0(980)$ tetraquark candidate. Considering the $N_f = 2 + 1$ ensemble in use, the first and second flavor thus become mass degenerate, i.e. $\phi^{(f_1)} = \phi^{(f_2)} = \phi^{(u/d)}$. This effectively reduces the number of required inversions for the application of point-to-all propagators by a factor of two. Multiple solutions of the same technique that only differ in their flavor are not further emphasized below, but become redundant in the case of mass degenerate flavors.

	(a)	(b)	(c)
one-end trick		$\phi^{(f_1)}, \tilde{\phi}^{(f_2)}$	
point-to-all propagators	$\phi^{(f_1)}, \phi^{(f_2)}, \phi^{(f_3)}$		$\phi^{(f_1)}, \phi^{(f_2)}$
stochastic timeslice-to-all		$N_{\Delta t} \phi^{(f_3)}$	$N_{\Delta t} \phi^{(f_3)}$

TAB. B.4: Number of solutions required for the different methods of C_{12} , C_{13} and C_{14} .

Stochastic timeslice-to-all propagators with a starting and endpoint on a single timeslices require independent solutions on $N_{\Delta t}$ subsequent timeslices. This will eventually lead to a maximum number of $N_{\Delta t}$ temporal separations and has to be considered in comparison to method (a), which covers the whole temporal lattice extent with little effort.

	(a)	(b)
one-end trick	$\psi^{(f_1:f_3)}, \phi^{(f_2)}, \phi^{(f_3)}$	
point-to-all propagators		$\psi^{(f_1:f_3)}, \phi^{(f_2)}, \phi^{(f_3)}$

TAB. B.5: Number of solutions required for the different methods of C_{15} .

The Dirac structure at the source of C_{15} is $\Gamma = \gamma_5$, so that the ϕ 's of the one-end trick are based on the same source vector and do not need to be distinguished in Table B.5. Although $\phi^{(f_3)}$ is not explicitly required for the contraction of the correlation function, it is shown in the table as it is required as a source vector for the sequential propagator procedure, i.e. $\psi^{(f_1:f_3)}$ is the solution of a linear system of the form $D^{(f_1)} \psi^{(f_1:f_3)} = \gamma_5 \phi^{(f_3)}$. For a scenario with no mass degeneracy between the first and second flavor the sequential propagator procedure can be applied to either of them.

	(a)	(b)	(c)
one-end trick	$\phi^{(f_1)}, \phi^{(f_2)}$	$\phi^{(f_1)}, \phi^{(f_2)}$	
point-to-all propagators		$\phi^{(f_3)}$	$\phi^{(f_1)}, \phi^{(f_2)}$
stochastic time- slice-to-all	$\phi^{(f_3)}$		$\phi^{(f_3)}$

TAB. B.6: Number of solutions required for the different methods of C_{16} .

	(a)	(b)	(c)
one-end trick	$\phi^{(f_1)}, \phi^{(f_3)}, \chi^{(f_2)}, \chi^{(f_3)}$	$\phi^{(f_2)}, \phi^{(f_3)}$	
point-to-all propagators		$\phi^{(f_1)}, \phi^{(f_3)}$	$\phi^{(f_1)}, \phi^{(f_2)}, \phi^{(f_3)}$

	(a)	(b ₁)	(b ₂)	(c)
one-end trick	$\phi^{(f_1)}, \phi^{(f_2)}, \chi^{(f_3)}$	$\phi^{(f_1)}, \phi^{(f_2)}$	$\phi^{(f_3)}$	
point-to-all propagators		$\phi^{(f_3)}$	$\phi^{(f_1)}, \phi^{(f_2)}$	$\phi^{(f_1)}, \phi^{(f_2)}, \phi^{(f_3)}$

TAB. B.7: Number of solutions required for the different methods of C_{25}, C_{35}, C_{45} 4×connected (top) and C_{26}, C_{36}, C_{46} 4×connected (bottom).

The χ 's, occurring for a first time in Table B.7, are ordinary solutions to the linear system with a source term different to the one of the ϕ 's, i.e. e.g. $\phi^{(f_3)} \equiv \phi^{(f_3)}[n]$ and $\chi^{(f_3)} \equiv \phi^{(f_3)}[n']$ with $n \neq n'$.

	(a)	(b)
one-end trick	$\psi^{(f_1;f_3)}, \phi^{(f_2)}, \phi^{(f_3)}$	
point-to-all propagators		$\psi^{(f_1;f_3)}, \phi^{(f_2)}, \phi^{(f_3)}$
stochastic time- slice-to-all	$N_{\Delta t} \phi^{(f_3)}$	$N_{\Delta t} \phi^{(f_3)}$

TAB. B.8: Number of solutions required for the different methods of C_{25}, C_{35}, C_{45} $2 \times$ connected.

	(a)	(b)
one-end trick	$\phi^{(f_1)}, \phi^{(f_2)}$	
point-to-all propagators		$\phi^{(f_1)}, \phi^{(f_2)}, \phi^{(f_3)}$
stochastic time- slice-to-all	$N_{\Delta t} \phi^{(f_3)}$	$N_{\Delta t} \phi^{(f_3)}$

TAB. B.9: Number of solutions required for the different methods of C_{26}, C_{36}, C_{46} $2 \times$ connected.

	(a)	(b)
one-end trick	$\phi^{(f_1)}, \phi^{(f_3)}, \chi^{(f_2)}, \chi^{(f_3)}$	$\phi^{(f_2)}, \phi^{(f_3)}$
point-to-all propagators		$\phi^{(f_1)}, \phi^{(f_3)}$

	(a)	(b ₁)	(b ₂)
one-end trick	$\phi^{(f_1)}, \phi^{(f_2)}, \chi^{(f_3)}$	$\phi^{(f_1)}, \phi^{(f_2)}$	$\phi^{(f_3)}$
point-to-all propagators		$\phi^{(f_3)}$	$\phi^{(f_1)}, \phi^{(f_2)}$

TAB. B.10: Number of solutions required for the different methods of C_{55} $4 \times$ connected (top) and C_{66} $4 \times$ connected (bottom).

	(a)	(b ₁)	(b ₂)
one-end trick	$\phi^{(f_1)}, \phi^{(f_3)}, \chi^{(f_2)}, \chi^{(f_3)}$	$\phi^{(f_1)}, \phi^{(f_2)}$	$\phi^{(f_3)}$
point-to-all propagators		$\phi^{(f_3)}$	$\phi^{(f_1)}, \phi^{(f_2)}$

TAB. B.11: Number of solutions required for the different methods of C_{56} $4 \times$ connected.

	(a)	(b)	(c)
one-end trick	$N_{\Delta t} \psi^{(f_3:f_1)}, \phi^{(f_1)}, \phi^{(f_2)}$	$\psi^{(f_1:f_3)}, \phi^{(f_3)}, \phi^{(f_2)}$	
point-to-all propagators	$\phi^{(f_3)}$		$\psi^{(f_1:f_3)}, \phi^{(f_3)}, \phi^{(f_2)}$
stochastic time- slice-to-all		$N_{\Delta t} \phi^{(f_3)}$	$N_{\Delta t} \phi^{(f_3)}$

TAB. B.12: Number of solutions required for the different methods of C_{56} $2 \times$ connected.

BIBLIOGRAPHY

- [1] K. G. Wilson, Phys. Rev. D **10**, 2445 (1974). doi:10.1103/PhysRevD.10.2445
- [2] S. Durr *et al.*, Science **322**, 1224 (2008) doi:10.1126/science.1163233 [arXiv:0906.3599 [hep-lat]].
- [3] J. Bulava, R. G. Edwards, E. Engelson, B. Joo, H. W. Lin, C. Morningstar, D. G. Richards and S. J. Wallace, Phys. Rev. D **82**, 014507 (2010) doi:10.1103/PhysRevD.82.014507 [arXiv:1004.5072 [hep-lat]].
- [4] J. J. Dudek, R. G. Edwards, M. J. Peardon, D. G. Richards and C. E. Thomas, Phys. Rev. D **82**, 034508 (2010) doi:10.1103/PhysRevD.82.034508 [arXiv:1004.4930 [hep-ph]].
- [5] L. Liu *et al.* [Hadron Spectrum Collaboration], JHEP **1207**, 126 (2012) doi:10.1007/JHEP07(2012)126 [arXiv:1204.5425 [hep-ph]].
- [6] J. J. Dudek *et al.* [Hadron Spectrum Collaboration], Phys. Rev. D **88**, no. 9, 094505 (2013) doi:10.1103/PhysRevD.88.094505 [arXiv:1309.2608 [hep-lat]].
- [7] K. Cichy, M. Kalinowski and M. Wagner, Phys. Rev. D **94**, no. 9, 094503 (2016) doi:10.1103/PhysRevD.94.094503 [arXiv:1603.06467 [hep-lat]].
- [8] R. L. Jaffe and F. Wilczek, Phys. Rev. Lett. **91**, 232003 (2003) doi:10.1103/PhysRevLett.91.232003 [hep-ph/0307341].
- [9] R. L. Jaffe, Phys. Rept. **409**, 1 (2005) doi:10.1016/j.physrep.2004.11.005 [hep-ph/0409065].
- [10] Z. Q. Liu *et al.* [Belle Collaboration], Phys. Rev. Lett. **110**, 252002 (2013) doi:10.1103/PhysRevLett.110.252002 [arXiv:1304.0121 [hep-ex]].
- [11] M. Ablikim *et al.* [BESIII Collaboration], Phys. Rev. Lett. **110**, 252001 (2013) doi:10.1103/PhysRevLett.110.252001 [arXiv:1303.5949 [hep-ex]].
- [12] R. Aaij *et al.* [LHCb Collaboration], Phys. Rev. Lett. **115**, 072001 (2015) doi:10.1103/PhysRevLett.115.072001 [arXiv:1507.03414 [hep-ex]].
- [13] C. J. Morningstar and M. J. Peardon, Phys. Rev. D **60**, 034509 (1999) doi:10.1103/PhysRevD.60.034509 [hep-lat/9901004].

-
- [14] P. Bicudo, K. Cichy, A. Peters, B. Wagenbach and M. Wagner, Phys. Rev. D **92**, no. 1, 014507 (2015) doi:10.1103/PhysRevD.92.014507 [arXiv:1505.00613 [hep-lat]].
- [15] P. Bicudo, J. Scheunert and M. Wagner, Phys. Rev. D **95**, no. 3, 034502 (2017) doi:10.1103/PhysRevD.95.034502 [arXiv:1612.02758 [hep-lat]].
- [16] M. Luscher, Commun. Math. Phys. **104**, 177 (1986). doi:10.1007/BF01211589
- [17] M. Luscher, Commun. Math. Phys. **105**, 153 (1986). doi:10.1007/BF01211097
- [18] S. h. Lee *et al.* [Fermilab Lattice and MILC Collaborations], arXiv:1411.1389 [hep-lat].
- [19] S. Prelovsek, C. B. Lang, L. Leskovec and D. Mohler, Phys. Rev. D **91**, no. 1, 014504 (2015) doi:10.1103/PhysRevD.91.014504 [arXiv:1405.7623 [hep-lat]].
- [20] Y. Chen *et al.*, Phys. Rev. D **89**, no. 9, 094506 (2014) doi:10.1103/PhysRevD.89.094506 [arXiv:1403.1318 [hep-lat]].
- [21] C. Alexandrou, J. O. Daldrop, M. Dalla Brida, M. Gravina, L. Scorzato, C. Urbach and M. Wagner, JHEP **1304** (2013) 137 doi:10.1007/JHEP04(2013)137 [arXiv:1212.1418 [hep-lat]].
- [22] M. Wagner, C. Alexandrou, M. Gravina, J. O. Daldrop, C. Urbach, M. Dalla Brida, L. Scorzato and C. Wiese, PoS ConfinementX , 108 (2012) [arXiv:1212.1648 [hep-lat]].
- [23] M. Wagner *et al.* [European Twisted Mass Collaboration], PoS LATTICE **2013**, 258 (2014) [arXiv:1309.0850 [hep-lat]].
- [24] J. Berlin, A. Abdel-Rehim, C. Alexandrou, M. Dalla Brida, M. Gravina and M. Wagner, PoS LATTICE **2014**, 104 (2014) [arXiv:1410.8757 [hep-lat]].
- [25] J. Berlin, A. Abdel-Rehim, C. Alexandrou, M. Dalla Brida, M. Gravina and M. Wagner, PoS LATTICE **2015**, 096 (2016) [arXiv:1508.04685 [hep-lat]].
- [26] J. Berlin, A. Abdel-Rehim, C. Alexandrou, M. Dalla Brida, J. Finkenrath, M. Gravina, T. Leontiou and M. Wagner, PoS LATTICE **2016**, 128 (2016) [arXiv:1611.07762 [hep-lat]].
- [27] A. Abdel-Rehim, C. Alexandrou, J. Berlin, M. Dalla Brida, J. Finkenrath and M. Wagner, arXiv:1701.07228 [hep-lat].
- [28] J. Finkenrath, C. Alexandrou, J. Berlin, M. Dalla Brida, T. Leontiou and M. Wagner, PoS LATTICE **2016**, 129 (2017) [arXiv:1701.07673 [hep-lat]].
- [29] C. Patrignani *et al.* [Particle Data Group], Chin. Phys. C **40**, no. 10, 100001 (2016). doi:10.1088/1674-1137/40/10/100001
- [30] F. E. Close and N. A. Tornqvist, J. Phys. G **28**, R249 (2002) doi:10.1088/0954-3899/28/10/201 [hep-ph/0204205].
-

-
- [31] C. Amsler and N. A. Tornqvist, Phys. Rept. **389**, 61 (2004). doi:10.1016/j.physrep.2003.09.003
- [32] E. Klempt and A. Zaitsev, Phys. Rept. **454**, 1 (2007) doi:10.1016/j.physrep.2007.07.006 [arXiv:0708.4016 [hep-ph]].
- [33] H. J. Rothe, “Lattice gauge theories: An Introduction,” World Sci. Lect. Notes Phys. **82**, 1 (2012).
- [34] I. Montvay and G. Munster, “Quantum fields on a lattice,” Cambridge, UK: Univ. Pr. (1994) 491 p. (Cambridge monographs on mathematical physics)
- [35] C. Gattringer and C. B. Lang, “Quantum chromodynamics on the lattice,” Lect. Notes Phys. **788**, 1 (2010). doi:10.1007/978-3-642-01850-3
- [36] T. DeGrand and C. DeTar, “Lattice Methods for Quantum Chromodynamics,” World Scientific, Singapore, 2006.
- [37] R. Gupta, “Introduction to lattice QCD: Course,” hep-lat/9807028.
- [38] U. J. Wiese, “An introduction to lattice field theory”
- [39] L. Lellouch, R. Sommer, B. Svetitsky, A. Vladikas and L. F. Cugliandolo, “Modern perspectives in lattice QCD: Quantum field theory and high performance computing. Proceedings, International School, 93rd Session, Les Houches, France, August 3-28, 2009,”
- [40] M. Luscher and P. Weisz, Phys. Lett. **158B**, 250 (1985). doi:10.1016/0370-2693(85)90966-9
- [41] M. Luscher and P. Weisz, Commun. Math. Phys. **97**, 59 (1985) Erratum: [Commun. Math. Phys. **98**, 433 (1985)]. doi:10.1007/BF01206178
- [42] Y. Iwasaki, preprint, UTHEP-118 (1983), unpublished
- [43] Y. Iwasaki, “Renormalization group analysis of lattice theories and improved lattice action: two-dimensional nonlinear $O(N)$ Sigma Model,” Nucl. Phys. B **258**, 141 (1985).
- [44] H. B. Nielsen and M. Ninomiya, Nucl. Phys. B **185**, 20 (1981) Erratum: [Nucl. Phys. B **195**, 541 (1982)]. doi:10.1016/0550-3213(81)90361-8, 10.1016/0550-3213(82)90011-6
- [45] H. B. Nielsen and M. Ninomiya, Nucl. Phys. B **193**, 173 (1981). doi:10.1016/0550-3213(81)90524-1
- [46] L. Susskind, Phys. Rev. D **16**, 3031 (1977). doi:10.1103/PhysRevD.16.3031
- [47] H. S. Sharatchandra, H. J. Thun and P. Weisz, Nucl. Phys. B **192**, 205 (1981). doi:10.1016/0550-3213(81)90200-5
-

-
- [48] P. H. Ginsparg and K. G. Wilson, Phys. Rev. D **25**, 2649 (1982). doi:10.1103/PhysRevD.25.2649
- [49] H. Neuberger, Phys. Lett. B **417**, 141 (1998) doi:10.1016/S0370-2693(97)01368-3 [hep-lat/9707022].
- [50] H. Neuberger, Phys. Lett. B **427**, 353 (1998) doi:10.1016/S0370-2693(98)00355-4 [hep-lat/9801031].
- [51] D. B. Kaplan, Phys. Lett. B **288**, 342 (1992) doi:10.1016/0370-2693(92)91112-M [hep-lat/9206013].
- [52] V. Furman and Y. Shamir, Nucl. Phys. B **439**, 54 (1995) doi:10.1016/0550-3213(95)00031-M [hep-lat/9405004].
- [53] C. Gattringer, I. Hip and C. B. Lang, Nucl. Phys. B **597**, 451 (2001) doi:10.1016/S0550-3213(00)00717-3 [hep-lat/0007042].
- [54] C. Gattringer, Phys. Rev. D **63**, 114501 (2001) doi:10.1103/PhysRevD.63.114501 [hep-lat/0003005].
- [55] B. Sheikholeslami and R. Wohlert, Nucl. Phys. B **259**, 572 (1985). doi:10.1016/0550-3213(85)90002-1
- [56] M. Luscher, S. Sint, R. Sommer and P. Weisz, Nucl. Phys. B **478**, 365 (1996) doi:10.1016/0550-3213(96)00378-1 [hep-lat/9605038].
- [57] M. Luscher, S. Sint, R. Sommer, P. Weisz and U. Wolff, Nucl. Phys. B **491**, 323 (1997) doi:10.1016/S0550-3213(97)00080-1 [hep-lat/9609035].
- [58] R. G. Edwards, U. M. Heller and T. R. Klassen, Nucl. Phys. Proc. Suppl. **63**, 847 (1998) doi:10.1016/S0920-5632(97)00918-3 [hep-lat/9710054].
- [59] M. Luscher and P. Weisz, Nucl. Phys. B **479**, 429 (1996) doi:10.1016/0550-3213(96)00448-8 [hep-lat/9606016].
- [60] R. Frezzotti *et al.* [Alpha Collaboration], JHEP **0108**, 058 (2001) [hep-lat/0101001]
- [61] R. Frezzotti and G. C. Rossi, JHEP **0410**, 070 (2004) doi:10.1088/1126-6708/2004/10/070 [hep-lat/0407002]
- [62] A. Shindler, Phys. Rept. **461**, 37 (2008) doi:10.1016/j.physrep.2008.03.001 [arXiv:0707.4093 [hep-lat]].
- [63] P. de Forcrand, PoS LAT **2009**, 010 (2009) [arXiv:1005.0539 [hep-lat]].
- [64] S. Duane, A. D. Kennedy, B. J. Pendleton and D. Roweth, Phys. Lett. B **195**, 216 (1987). doi:10.1016/0370-2693(87)91197-X
- [65] S. Aoki *et al.* [PACS-CS Collaboration], Phys. Rev. D **79**, 034503 (2009) doi:10.1103/PhysRevD.79.034503 [arXiv:0807.1661 [hep-lat]].
-

-
- [66] R. Sommer, Nucl. Phys. B **411**, 839 (1994) doi:10.1016/0550-3213(94)90473-1 [hep-lat/9310022].
- [67] S. Aoki *et al.* [JLQCD Collaboration], Phys. Rev. D **78**, 014508 (2008) doi:10.1103/PhysRevD.78.014508 [arXiv:0803.3197 [hep-lat]].
- [68] C. B. Lang, D. Mohler, S. Prelovsek and M. Vidmar, Phys. Rev. D **84**, no. 5, 054503 (2011) Erratum: [Phys. Rev. D **89**, no. 5, 059903 (2014)] doi:10.1103/PhysRevD.89.059903, 10.1103/PhysRevD.84.054503 [arXiv:1105.5636 [hep-lat]].
- [69] S. Capitani, M. Della Morte, G. von Hippel, B. Knippschild and H. Wittig, PoS LATTICE **2011**, 145 (2011) [arXiv:1110.6365 [hep-lat]].
- [70] D. J. Wilson, R. A. Briceño, J. J. Dudek, R. G. Edwards and C. E. Thomas, Phys. Rev. D **92**, no. 9, 094502 (2015) doi:10.1103/PhysRevD.92.094502 [arXiv:1507.02599 [hep-ph]].
- [71] C. Alexandrou *et al.* [ETM Collaboration], Phys. Rev. D **80**, 114503 (2009) doi:10.1103/PhysRevD.80.114503 [arXiv:0910.2419 [hep-lat]].
- [72] G. S. Bali *et al.*, Nucl. Phys. B **866**, 1 (2013) doi:10.1016/j.nuclphysb.2012.08.009
- [73] R. Baron *et al.*, JHEP **1006**, 111 (2010) doi:10.1007/JHEP06(2010)111 [arXiv:1004.5284 [hep-lat]].
- [74] P. Fritzsche, F. Knechtli, B. Leder, M. Marinkovic, S. Schaefer, R. Sommer and F. Virotta, Nucl. Phys. B **865**, 397 (2012) doi:10.1016/j.nuclphysb.2012.07.026 [arXiv:1205.5380 [hep-lat]].
- [75] S. Lottini [ALPHA Collaboration], PoS LATTICE **2013**, 315 (2014) [arXiv:1311.3081 [hep-lat]].
- [76] C. Michael, Nucl. Phys. B **259**, 58 (1985). doi:10.1016/0550-3213(85)90297-4
- [77] M. Luscher and U. Wolff, Nucl. Phys. B **339**, 222 (1990). doi:10.1016/0550-3213(90)90540-T
- [78] B. Blossier, M. Della Morte, G. von Hippel, T. Mendes and R. Sommer, JHEP **0904**, 094 (2009) doi:10.1088/1126-6708/2009/04/094 [arXiv:0902.1265 [hep-lat]].
- [79] J. J. Dudek, R. G. Edwards and C. E. Thomas, Phys. Rev. D **86**, 034031 (2012) doi:10.1103/PhysRevD.86.034031 [arXiv:1203.6041 [hep-ph]].
- [80] J. Bulava, B. Fahy, B. Hörz, K. J. Juge, C. Morningstar and C. H. Wong, Nucl. Phys. B **910**, 842 (2016) doi:10.1016/j.nuclphysb.2016.07.024 [arXiv:1604.05593 [hep-lat]].
- [81] M. Kalinowski and M. Wagner, Phys. Rev. D **92**, no. 9, 094508 (2015) doi:10.1103/PhysRevD.92.094508 [arXiv:1509.02396 [hep-lat]].
-

-
- [82] C. Alexandrou, C. N. Papanicolas and E. Stiliaris, PoS LATTICE **2008**, 099 (2008) [arXiv:0810.3982 [hep-lat]].
- [83] C. N. Papanicolas and E. Stiliaris, arXiv:1205.6505 [hep-ph].
- [84] C. Alexandrou, T. Leontiou, C. N. Papanicolas and E. Stiliaris, Phys. Rev. D **91**, no. 1, 014506 (2015) doi:10.1103/PhysRevD.91.014506 [arXiv:1411.6765 [hep-lat]].
- [85] S. Prelovsek, T. Draper, C. B. Lang, M. Limmer, K. F. Liu, N. Mathur and D. Mohler, Phys. Rev. D **82**, 094507 (2010) doi:10.1103/PhysRevD.82.094507 [arXiv:1005.0948 [hep-lat]].
- [86] S. Ozaki and S. Sasaki, Phys. Rev. D **87**, no. 1, 014506 (2013) doi:10.1103/PhysRevD.87.014506 [arXiv:1211.5512 [hep-lat]].
- [87] S. Prelovsek and L. Leskovec, Phys. Rev. Lett. **111**, 192001 (2013) doi:10.1103/PhysRevLett.111.192001 [arXiv:1307.5172 [hep-lat]].
- [88] J. O. Daldrop *et al.* [ETM Collaboration], PoS LATTICE **2012**, 161 (2012) [arXiv:1211.5002 [hep-lat]].
- [89] C. Alexandrou, P. de Forcrand and B. Lucini, Phys. Rev. Lett. **97**, 222002 (2006) doi:10.1103/PhysRevLett.97.222002 [hep-lat/0609004].
- [90] M. Hestenes and E. Stiefel, "Methods of Conjugate Gradients for Solving Linear Systems," Journal of Research of the National Bureau of Standards **49** (6) (1952) doi:10.6028/jres.049.044.
- [91] H. A. van der Vorst, "Bi-CGSTAB: A Fast and Smoothly Converging Variant of Bi-CG for the Solution of Nonsymmetric Linear Systems," SIAM J. Sci. and Stat. Comput. **13** (2): 631-644 (1992) doi:10.1137/0913035.
- [92] R. Babich, J. Brannick, R. C. Brower, M. A. Clark, T. A. Manteuffel, S. F. McCormick, J. C. Osborn and C. Rebbi, Phys. Rev. Lett. **105**, 201602 (2010) doi:10.1103/PhysRevLett.105.201602 [arXiv:1005.3043 [hep-lat]].
- [93] J. C. Osborn, R. Babich, J. Brannick, R. C. Brower, M. A. Clark, S. D. Cohen and C. Rebbi, PoS LATTICE **2010**, 037 (2010) [arXiv:1011.2775 [hep-lat]].
- [94] M. Albanese *et al.* [APE Collaboration], Phys. Lett. B **192**, 163 (1987). doi:10.1016/0370-2693(87)91160-9
- [95] M. Falcioni, M. L. Paciello, G. Parisi and B. Taglienti, Nucl. Phys. B **251**, 624 (1985). doi:10.1016/0550-3213(85)90280-9
- [96] S. Gusken, Nucl. Phys. Proc. Suppl. **17**, 361 (1990). doi:10.1016/0920-5632(90)90273-W
- [97] T. A. DeGrand and R. D. Loft, Comput. Phys. Commun. **65**, 84 (1991). doi:10.1016/0010-4655(91)90158-H
-

-
- [98] K. Jansen *et al.* [ETM Collaboration], JHEP **0812**, 058 (2008) doi:10.1088/1126-6708/2008/12/058 [arXiv:0810.1843 [hep-lat]].
- [99] C. Wiese, “Efficient computation of meson and four-quark correlation functions”, Master of Science thesis at Humboldt University of Berlin (2012).
- [100] S. Prelovsek and D. Mohler, Phys. Rev. D **79**, 014503 (2009) doi:10.1103/PhysRevD.79.014503 [arXiv:0810.1759 [hep-lat]].
- [101] C. McNeile *et al.* [UKQCD Collaboration], Phys. Rev. D **74**, 014508 (2006) doi:10.1103/PhysRevD.74.014508 [hep-lat/0604009].
- [102] C. Gattringer, L. Y. Glozman, C. B. Lang, D. Mohler and S. Prelovsek, Phys. Rev. D **78**, 034501 (2008) doi:10.1103/PhysRevD.78.034501 [arXiv:0802.2020 [hep-lat]].
- [103] G. P. Engel *et al.* [BGR [Bern-Graz-Regensburg] Collaboration], Phys. Rev. D **82**, 034505 (2010) doi:10.1103/PhysRevD.82.034505 [arXiv:1005.1748 [hep-lat]].
- [104] S. Prelovsek, AIP Conf. Proc. **1030**, 311 (2008) doi:10.1063/1.2973519 [arXiv:0804.2549 [hep-lat]].
- [105] M. Wakayama, T. Kunihiro, S. Muroya, A. Nakamura, C. Nonaka, M. Sekiguchi and H. Wada, Phys. Rev. D **91**, no. 9, 094508 (2015) doi:10.1103/PhysRevD.91.094508 [arXiv:1412.3909 [hep-lat]].
- [106] J. J. Dudek *et al.* [Hadron Spectrum Collaboration], Phys. Rev. D **93**, no. 9, 094506 (2016) doi:10.1103/PhysRevD.93.094506 [arXiv:1602.05122 [hep-ph]].
- [107] W. Wei, P. Z. Huang and S. L. Zhu, Phys. Rev. D **73**, 034004 (2006) doi:10.1103/PhysRevD.73.034004 [hep-ph/0510039].
- [108] Y. B. Dai, C. S. Huang, C. Liu and S. L. Zhu, Phys. Rev. D **68**, 114011 (2003) doi:10.1103/PhysRevD.68.114011 [hep-ph/0306274].
- [109] A. P. Szczepaniak, Phys. Lett. B **567**, 23 (2003) doi:10.1016/S0370-2693(03)00865-7 [hep-ph/0305060].
- [110] T. Barnes, F. E. Close and H. J. Lipkin, Phys. Rev. D **68**, 054006 (2003) doi:10.1103/PhysRevD.68.054006 [hep-ph/0305025].
- [111] V. Dmitrasinovic, Phys. Rev. Lett. **94**, 162002 (2005). doi:10.1103/PhysRevLett.94.162002
- [112] H. Kim and Y. Oh, Phys. Rev. D **72**, 074012 (2005) doi:10.1103/PhysRevD.72.074012 [hep-ph/0508251].
- [113] E. van Beveren and G. Rupp, Phys. Rev. Lett. **91**, 012003 (2003) doi:10.1103/PhysRevLett.91.012003 [hep-ph/0305035].
- [114] G. Bali, S. Collins and P. Perez-Rubio, J. Phys. Conf. Ser. **426**, 012017 (2013) doi:10.1088/1742-6596/426/1/012017 [arXiv:1212.0565 [hep-lat]].
-

-
- [115] G. Moir, M. Peardon, S. M. Ryan, C. E. Thomas and L. Liu, JHEP **1305**, 021 (2013) doi:10.1007/JHEP05(2013)021 [arXiv:1301.7670 [hep-ph]].
- [116] D. Mohler, C. B. Lang, L. Leskovec, S. Prelovsek and R. M. Woloshyn, Phys. Rev. Lett. **111** (2013) no.22, 222001 doi:10.1103/PhysRevLett.111.222001 [arXiv:1308.3175 [hep-lat]].
- [117] C. B. Lang, L. Leskovec, D. Mohler, S. Prelovsek and R. M. Woloshyn, Phys. Rev. D **90** (2014) no.3, 034510 doi:10.1103/PhysRevD.90.034510 [arXiv:1403.8103 [hep-lat]].
- [118] R. G. Edwards *et al.* [SciDAC and LHPC and UKQCD Collaborations], Nucl. Phys. Proc. Suppl. **140**, 832 (2005) doi:10.1016/j.nuclphysbps.2004.11.254 [hep-lat/0409003].
-

ACKNOWLEDGMENTS

First and foremost, I want to thank my supervisor Marc Wagner for his outstanding support. I learned a lot about physics and the many discussions throughout the last years assured a constant and sound progress of this work. I am grateful for all the opportunities to report on the progress of my research in front of international audiences. It took me to many interesting places and pushed me to perform at my best. Furthermore I want to express my gratitude for all the responsibilities I was entrusted with.

I also want to thank my collaborators, without whom this work would not have reached this point. The excellent introduction to the project, the many Skype talks we had and your reliable support were of great value to me.

I want to thank every member of the Lattice QCD group of Frankfurt throughout the past years for making it such a pleasant stay. The friendly and humorous, yet dedicated and professional atmosphere is something I really appreciate. I proudly cannot point out individuals, as everyone of you made it an experience of a lifetime.

I thank Gerhard Bura and the whole team of HGS-HIRE for their support and continuous interest regarding my studies. Because of them I had the pleasure to attend many courses that helped me to improve myself.

Special thanks are due to Jonas Scheunert, Björn Wagenbach, Antje Peters, Jacob Finkenrath and Mattia Dalla Brida for reading through parts of this thesis and pointing out errors and flaws to me.

I thank my family for their constant support. Your pride in my development is an encouragement beyond words.

Last but not least, I am very grateful to Alina. You are everything I could ever ask for. Thank you for always being there for me.

Computations have been performed using the Chroma software library [118].

I acknowledge the support by the Emmy Noether Programme of the DFG (German Research Foundation), grant WA 3000/1-1.

This work was supported in part by the Helmholtz International Center for FAIR within the framework of the LOEWE program launched by the State of Hesse. Calculations on the LOEWE-CSC and on the on the FUCHS-CSC high-performance computer of the Frankfurt University were conducted for this research. I would like to thank HPC-Hessen, funded by the State Ministry of Higher Education, Research and the Arts, for programming advice.

This work was cofunded by the European Regional Development Fund and the Republic of Cyprus through the Research Promotion Foundation (Project Cy-Tera NEA ΤΠΟΔΟΜΗ/ΣΤΡΑΤΗ/0308/31) by the grand cypro914.

curriculum
v i t a e

JOSHUA BERLIN

PROZESSIONSWEG 3, D-60438 FRANKFURT AM MAIN

+49 (0)69 / 907 509 91 | berlin@th.physik.uni-frankfurt.de**Personal Data**

Date of Birth: 05.07.1989
Place of Birth: Frankfurt am Main
Nationality: german
Marital Status: unmarried

Education

November 2013 - April 2017 **PhD Candidate**

During my time as a PhD Candidate I developed a code to investigate potential exotic scalar mesons with lattice QCD. Studies of this kind rely on extensive correlation matrices with various propagator structures that were implemented. Large amounts of effort were invested in testing and optimizing methods to obtain the best possible signal at comparable numerical costs.

Supervisor: Prof. Dr. Wagner.
Goethe University, Frankfurt am Main, Germany.

October 2011 - October 2013 **Master of Science**

In my thesis I investigated a mixed action setup of twisted mass fermions and clover improved twisted mass fermions. Indications towards improved parity breaking effects on hadronic observables were studied on a single ensemble.

Supervisor: Prof. Dr. Wagner.
Minor: Astronomy.
Goethe University, Frankfurt am Main, Germany.

April 2009 - July 2011 **Bachelor of Science**

In my thesis I examined two models for heavy ion collisions in relativistic hydrodynamics. Following two major publications I worked into an at the time unfamiliar topic and reproduced fundamental results.

Supervisor: Prof. Dr. Rischke.
Minor: Philosophy.
Goethe University, Frankfurt am Main, Germany.

August 2008 - April 2009 **Civilian Service**

July 2008 **Abitur**

Experience

PRESENTATION

Multiple presentations given to audiences reaching from colleagues to international conferences, addressing new developments and recent progress of my dissertation topic.

- 34th International Symposium on Lattice Field Theory, 24-30 July 2016 (Southampton, UK)
- Bound states in QCD and beyond, 24-27 March 2015 (St. Goar, Germany)
- International Conference on Scientific Computing, 3-6 December 2013 (Paphos, Cyprus)

(*selected conferences)

TEACHING

- Held different tutorials for students on fundamental and specialized courses (2011-2017).
- Organized and developed a practical simulation course for Master students: “Lattice Monte-Carlo simulation of the quantum mechanical path integral” (2014-2017).
- Supported several Bachelor and Master projects during my time as PhD candidate.

TRAINING

Soft skill courses as part of the graduate school program.

- Basic Course III: Leadership and Career Development (March 2016)
- Basic Course II: Leading Teams in a Research Environment (November 2015)
- Basic Course I: Making an Impact as an Effective Researcher (October 2014)

Lecture and Power Weeks as part of the graduate school program

- Measuring properties of hadrons with PANDA and on the lattice (April 2016)
- Hadron physics at the Belle and BES experiments (May 2015)
- Software Design (September 2014)
- In-medium Properties of Hadrons (May 2014)

IT SKILLS

C++	Advanced object-oriented programming, GSL
Typography	L ^A T _E X
Tools	Vim, Gnuplot, Root
Other	MATLAB, Mathematica, SQL

Languages

German - native
 English - proficient

Publications

J. Finkenrath, C. Alexandrou, J. Berlin, M. Dalla Brida, T. Leontiou and M. Wagner,
“Using a new analysis method to extract excited states in the scalar meson sector,”
PoS LATTICE **2016**, 129 (2017) [arXiv:1701.07673 [hep-lat]].

A. Abdel-Rehim, C. Alexandrou, J. Berlin, M. Dalla Brida, J. Finkenrath and
M. Wagner,
“Investigating efficient methods for computing four-quark correlation functions,”
arXiv:1701.07228 [hep-lat].

* Publication accepted by the *Computer Physics Communications* Journal in May '17

J. Berlin, A. Abdel-Rehim, C. Alexandrou, M. Dalla Brida, J. Finkenrath,
M. Gravina, T. Leontiou and M. Wagner,
“Importance of closed quark loops for lattice QCD studies of tetraquarks,”
PoS LATTICE **2016**, 128 (2016) [arXiv:1611.07762 [hep-lat]].

J. Berlin, A. Abdel-Rehim, C. Alexandrou, M. Dalla Brida, M. Gravina and
M. Wagner,
“Computation of correlation matrices for tetraquark candidates with $J^P = 0^+$ and
flavor structure $q_1\bar{q}_2q_3\bar{q}_3$,”
PoS LATTICE **2015**, 096 (2016) [arXiv:1508.04685 [hep-lat]].

J. Berlin, A. Abdel-Rehim, C. Alexandrou, M. Dalla Brida, M. Gravina and
M. Wagner,
“Investigation of the tetraquark candidate $a_0(980)$: technical aspects and preliminary
results,”
PoS LATTICE **2014**, 104 (2014) [arXiv:1410.8757 [hep-lat]].

J. Berlin, D. Palao and M. Wagner,
“Testing mixed action approaches to meson spectroscopy with twisted mass sea quarks,”
PoS LATTICE **2013**, 441 (2014) [arXiv:1308.4916 [hep-lat]].

Awards

Prize for Best Posters at the GSI-FAIR Colloquium (May 2017)
“Young Scientists Poster Session”

Recipient of a Giersch Excellence Award (October 2015).
“In recognition of outstanding achievements in the doctoral thesis project.”
